# A review on mechanical alloying and spark plasma sintering of refractory high-entropy alloys

## Challenges, microstructures, and mechanical behavior

Martin, P.; Aguilar, C.; Cabrera, J. M.

**DOI**
10.1016/j.jmrt.2024.03.205

**Publication date**
2024

**Document Version**
Final published version

**Published in**
Journal of Materials Research and Technology

**Citation (APA)**
Martin, P., Aguilar, C., & Cabrera, J. M. (2024). A review on mechanical alloying and spark plasma sintering of refractory high-entropy alloys: Challenges, microstructures, and mechanical behavior. *Journal of Materials Research and Technology*, *30*, 1900-1928. https://doi.org/10.1016/j.jmrt.2024.03.205

Journal of Materials Research and Technology 30 (2024) 1900–1928

Contents lists available at ScienceDirect

Journal of Materials Research and Technology

journal homepage: www.elsevier.com/locate/jmrt

# A review on mechanical alloying and spark plasma sintering of refractory high-entropy alloys: Challenges, microstructures, and mechanical behavior

P. Martin [a,b,*], C. Aguilar [b,c], J.M. Cabrera [b,d]

[a] Department of Materials Science and Engineering, Delft University of Technology, Delft, Netherlands
[b] Department of Materials Science and Engineering, Technical University of Catalonia, Barcelona, Spain
[c] Departamento de Ingeniería Metalúrgica y Materiales, Universidad Técnica Federico Santa María, Valparaíso, Chile
[d] Fundació Centre CIM-UPC, Barcelona, Spain

ARTICLE INFO

*Keywords:*
High-entropy alloys
Mechanical properties
Powder metallurgy
Spark plasma sintering
Mechanical alloying

ABSTRACT

Refractory high-entropy alloys (RHEAs) are promising candidates for those applications requiring of strong materials at high temperatures with elevated thermal stability and excellent oxidation, irradiation, and corrosion resistance. Particularly, RHEAs synthesized using mechanical alloying (MA) followed by spark plasma sintering (SPS) has proven to be a successful path to produce stronger alloys than those produced by casting techniques. This superior behavior, at both room and high temperature, can be attributed to the microstructural features resultant from this powder metallurgy route, that include the presence of homogeneously distributed non-metallic particles, fine- and ultrafine-grained microstructures, and higher content of interstitial solutes. Nevertheless, the powder metallurgy fabrication relies over a complex balance of several operational variables, and the process is no exempt of certain challenges, such as contamination or the presence of pores in the bulk parts. This review aims to cover all the peculiarities of the MA + SPS route, the resultant microstructures, their mechanical properties, and the strengthening and deformation mechanisms behind their superior performance, as well as a brief description of their oxidation resistance.

## 1. Introduction

The current demands of the society for a more sustainable industry have guided materials science researchers to develop newer advanced materials to fulfill the needs of aerospace, nuclear, chemical, defense, or automotive sectors. In the first case, for example, a more efficient operation – with less fuel consumption and less $CO_2$ emissions – is nowadays limited by the temperature that turbine blades and disk materials (currently made of Ni-based superalloys) can sustain in terms of mechanical performance. The challenge is far from simple: these materials not only have to possess elevated mechanical strength at extreme temperatures but also outstanding oxidation and fatigue resistance as well as excellent thermal stability. A significant breakthrough came with the publication of the two first works [1,2] introducing the high-entropy alloys (HEAs) concept, opening a vast field of candidate alloys with a promising but – until that moment – unexplored potential.

Initially, HEAs were defined as those alloys constituted by at least five elements, all of them between 5 and 35 at. % [3]. This unusual composition – out of the traditional alloy design paradigm of diluted solutions with a clear and well-defined base element – would promote elevated values of the entropy of mixing ($\Delta S_m$) term at the liquid state; hence, after cooling, a single-phase solid solution (SPSS) microstructure containing all these components would be stable yet down to room temperature. The previous was termed the *high-entropy effect*, one of the four core effects – the other three included *high-lattice strain*, *sluggish diffusion*, and the *cocktail effect* – that defined the physical metallurgy and performance during the early development of high-entropy alloys. However, with the years, it was noted that SPSS microstructures were less frequent than multi-phase microstructures, as well some contradictory results were found regarding the rest of core effects. Hence, nowadays, the high-entropy alloy concept has evolved into a more flexible term – the *complex concentrated alloy* (CCA) concept – that groups all those alloys with a complex composition that lays out of the traditional alloy design paradigm, indistinctly of their microstructure [4,5]. Despite of that, the *high-entropy alloy* term continues as the reference term for the field, and therefore, it will be used in this review indistinctly of the microstructure of the alloy.

During the first decade of HEA development, the studies were

* Corresponding author. Department of Materials Science and Engineering, Delft University of Technology, Delft, Netherlands.
*E-mail address:* p.m.martinsaint-laurence@tudelft.nl (P. Martin).

https://doi.org/10.1016/j.jmrt.2024.03.205
Received 8 February 2024; Received in revised form 23 March 2024; Accepted 26 March 2024
Available online 30 March 2024

focused on alloys mainly containing 3d transition metals (TM) (and hence, termed as 3d TM HEAs): Fe, Ni, Co, and Mn, with the addition of other elements such as Cr, Cu, Al, and Ti. These alloys were mainly constituted by disordered face-centered cubic (fcc) solid solutions, presenting similar behavior that some austenitic stainless steels. A particularly interesting case is the equiatomic CoCrFeMnNi, also known as the Cantor' alloy, in recognition of the pioneer work by Cantor et al. [2]. This alloy possesses a SPSS fcc microstructure and interesting mechanical behavior, singularly at low temperatures [2,6,7]. It was just in 2010, that Senkov et al. [8] opened the frontiers of the field reporting the first HEAs entirely constituted by refractory elements, whose high-temperature mechanical performance was even superior to that of commercial Ni-based superalloys, as illustrated in Fig. 1. These alloys presented a disordered body-centered cubic (bcc) solid solution, that provided them a superior strength with a reduced ductility, in comparison to 3d TM HEAs. However, refractory high-entropy alloys (RHEAs) were immediately considered strong candidates with enormous potential to solve the previously mentioned high-temperature challenges.

The excellent results of Senkov's group started a fever to explore this new subfield by addressing two critical aspects of the first RHEAs: their room temperature brittleness, and their elevated density (the two first RHEAs possessed a density over 12 g $cm^{-3}$). The first is a challenging aspect of the RHEA development, and despite several efforts have been done in the area exploring several approaches (the effect of different substitutional elements [10–17], doping with interstitial elements [18–22], tuning the electronic properties of the alloy [10,23], among others) there is no a clear strategy to solve it yet. On the other hand, the density issue could have been straightforwardly addressed by prioritizing lighter elements, such as Ti or V, using less content of the heaviest refractory elements (like W and Ta), and incorporating non-refractory but lighter elements, such as Al or Si. Nevertheless, in the case of SPSS alloys, an elevated high-temperature strength is directly related to an elevated alloy melting point that will result from the melting point of the constituent elements [24]; unfortunately, elements that possess low density also present lower melting points. Thus, SPSS RHEAs with high mechanical strength at elevated temperature will have poor specific yield strength (SYS) and vice versa. Additionally, the high-temperature oxidation resistance is also a performance property that has to be considered in the design of RHEAs, since refractory metals (such as W, Mo, and V) intrinsically possess poor oxidation resistance and may be subjected to the pesting phenomenon, as well as some of their oxides are susceptible of volatilization and sublimation and present poor adherence [25]. In that way, alloying elements such as Cr, Al, and Si may contribute to enhance the oxidation resistance of RHEAs. Hence, having all that into consideration, the alloy design must be accompanied by additional strategies in order to find a superior balance between mechanical performance, lightness, and oxidation resistance, not only through compositional tunning, but also through the fabrication route, in order to obtain superior microstructures.

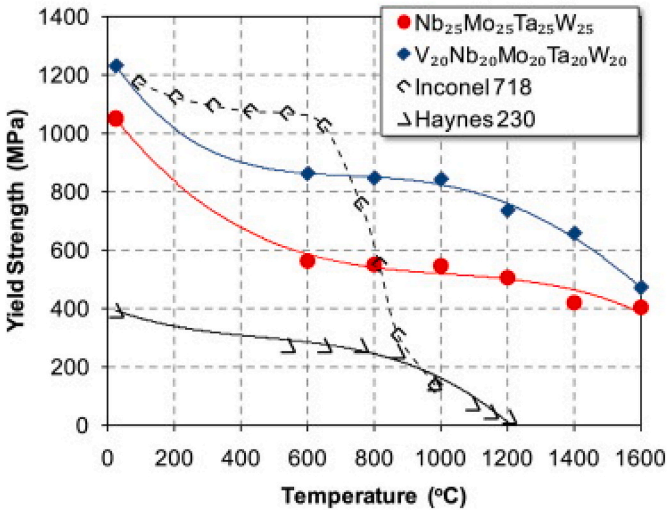


**Fig. 1.** Yield strength ($\sigma_{YS}$) as a function of the temperature of the first RHEAs, MoNbTaW and MoNbTaVW, and of two commercial superalloys [9]. Reproduced with permission of Elsevier.

Most RHEAs (including the pioneer RHEAs) have been fabricated by arc melting, in spite of the undesired casting defects that this route causes, such as dendritic microstructures (observed in alloys with elevated melting point differences between constituents [26] or non-zero enthalpies of mixing ($\Delta H_m$) [27]), coarse grain size (attributed to the elevated temperatures required to melt elements with high melting points such as W or Hf), or the evaporation or sublimation of constituent elements. Aiming to produce more homogeneous microstructures, annealing and hot isostatic pressing (HIP) post-treatments are usually conducted [8,28–33], although with no considerable effect over the mechanical properties. A particular exception of casting-produced RHEAs is the refractory high-entropy superalloys (RHSAs) subfamily [34,35]; these are Al-containing dual-phase RHEAs constituted by disordered and ordered (B2) bcc solid solutions forming a nanoscale cuboid-like microstructure, that resembles that of Ni-based superalloys [35–37]. These alloys are constituted by important amounts of light elements (Al, Ti, and Zr) and due to their advanced microstructure, a superior SYS is achieved (as represented in Fig. 2), showing that advanced microstructures in multi-phase RHEAs conduct to a superior performance and balance of strength and density.

On the other hand, the powder metallurgy (PM) route, particularly mechanical alloying (MA) followed by spark plasma sintering (SPS), can lead to the obtention of advanced microstructures with excellent mechanical behavior at both room and at high temperatures, as has been reported in several cases [21,38–47]. MA corresponds to a solid-state fabrication technique, in which the alloying is achieved by means of the repetitive impact of balls over particles of mixtures of elemental or prealloyed powders [48]. After that, the alloyed powder is subjected to SPS, in which the simultaneous flow of electric current through the particles and the application of stress for tens of minutes produce almost fully-dense bulk samples. This route presents strong advantages in comparison to casting: i) because the alloy is formed in the solid state, the bulk samples will not present a dendritic microstructure nor an inhomogeneous microstructure; ii) MA processing avoids strong chemical segregation between elements with very different melting points (which is especially relevant in Al-containing RHEAs, where the differences on melting point may be as high as 1500 °C), iii) it may lead to the fabrication of fully-dense bulk pieces with fine and ultrafine grain size, that enhances the room temperature yield strength ($\sigma_{YS}$) of the alloy, iv) fine and homogeneously dispersed precipitates (oxides, carbides, and nitrides) are formed during the sintering stage, pinning grain boundaries and inhibiting grain growth during high-temperature exposure, strengthening the alloy, among others [49,50]. The microstructural features that govern the mechanical properties and deformation mechanisms of MA + SPS RHEAs parts are summarized in Fig. 2.

Nevertheless, PM fabrication is far from being simple and straightforward and has its limitations too, so several aspects must be considered. On the one hand, the MA + SPS route has serious limitations in terms of producing large parts as well as industrial-scale production (where casting techniques may be more appropriate) and dies are usually expensive and limited in terms of highly complex shapes (where additive manufacturing techniques would be preferred). On the other hand, the powder and bulk samples are exposed to several sources of contamination, that will affect the composition and microstructure of the samples. Additionally, a large number of operational parameters and variables are involved during MA that will affect the physical and chemical characteristics of the milled powder. All of these, alongside the operational parameters of the sintering stage and the alloy composition,

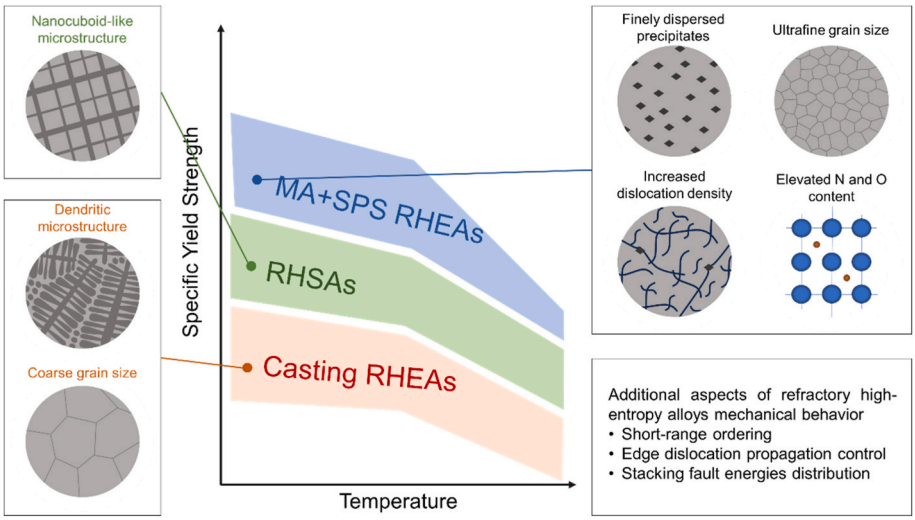


**Fig. 2.** Summary of the microstructural features and high-temperature mechanical strength of MA + SPS RHEAs, RHSAs, and Casting RHEAs.

will determine the resulting microstructure and performance of the bulk alloys.

A couple of works have been published reviewing the PM synthesis of HEAs [51–53]; nevertheless, since RHEAs are somehow less reported than 3d TM HEAs, their peculiarities are not appropriately nor extensively addressed. In the same way, various review manuscripts addressing RHEAs have been published too during the last couple of years [4,28,54]. Still, none of them particularly focused on those produced by the PM route (which are less common than those fabricated by casting despite their poorer performance).

Hence, the present review aims to focus exclusively on those RHEAs fabricated using the MA + SPS route, the main challenges related to powder alloy fabrication by means of MA, as well as the obtention of bulk samples through SPS (with a few mentions of samples sintered using other techniques for comparison purposes) with a special consideration of the particularities of the elemental powders that constitute RHEAs. Thus, the first section will be focused on the discussion of how the operational parameters of MA affect the main outcomes of the process, such as phase evolution, physical characteristics of the powder, powder yield, and contamination. Then, a second section will address the effect of sintering conditions and techniques over microstructure, keeping an eye on how the powder features (physical characteristics, chemical composition, and chemical homogeneity) affect it too. Then, the mechanical behavior of PM RHEAs is discussed, especially focusing on the high-temperature performance, addressing how the fabrication route, the chemical composition, and the microstructure can affect it. Additionally, a discussion addressing the involved softening and deformation mechanisms is revised, by means of constitutive and microstructural analysis of deformed samples. Lastly, a short description of high-temperature oxidation resistance reports of MA + SPS and SPS RHEAs will be presented.

## 2. Mechanical alloying of RHEAs

During MA, particles are exposed to various physical phenomenon, such as plastic deformation, agglomeration, cold welding, and fracture. In the early stage of milling, ductile powders are plastically deformed by means of the impacts of balls, acquiring elongated particle shapes; in opposition, brittle powders likely suffer fracture, evidenced through particle size reduction. With further milling time, the cold welding phenomenon may be activated, providing the necessary particle-particle contact to allow diffusion – in the case of particles of different composition – and therefore, the alloying. Fig. 3 illustrates the evolution of the particles as well as of the distribution of the elements on them during the milling of an $Al_{0.3}NbTa_{0.8}Ti_{1.5}V_{0.2}Zr$ RHEA [55]. As can be appreciated from Fig. 3 c (that illustrates the powder in the unmilled state) and Fig. 3 f (after 1 h of milling), the particle size increased considerably evidencing how much cold welding predominated. Fig. 3.2 shows how cold-welded particles are constituted by different layers of different composition. With further milling time, these layers become finer due to the continuous plastic deformation exerted by the balls impacts, up to a point in which they become indistinguishable, as displayed in Fig. 3.5. Fig. 3 o shows that, after 10 h of milling, the fracture phenomenon acquires a main role, since fine particles can be appreciated. These processes will compete during the rest of the milling, up to reaching a steady state, from which no considerable changes in the particle size are observed.

The phase and particle evolution during MA results from a complex relationship between several aspects, that includes intrinsic characteristics of the involved elemental powders (hardness, solubility, melting point), additional characteristics of the involved elemental powders (granulometry, purity, morphology) associated to their fabrication processes, and operational parameters (rotational speed, the ball-to-powder mass ratio or BPR, milling time, ball sizes, and atmosphere) that define the amount of transferred energy [56,57]. Besides, additional organic reagents, commonly referred as a process control agents (PCA), can be employed to decrease the surface energy of the powder and thus to control cold welding [48].

In most of the cases, the goals of MA are the same: the desired phenomena (e.g. alloying, particle size reduction, amorphization) must be achieved in the shortest milling time, producing as much grams of powder per batch as possible, with the minimum contamination, at the lowest cost. Notwithstanding, the mentioned operational variables may contribute positively to some of these goals, but simultaneously, in a negative manner to the rest. For example, increasing the rotational speed would reduce the milling time required to produce an alloy, but it would also promote grinding media wear and contamination of the sample. Thus, the election of the operational setting of the MA process lays over a delicate balance.

The laboratory conditions used for the synthesis of RHEA powder employing MA are summarized in Appendix A of the Supplementary Material. As can be appreciated, most of these works employ planetary ball mills, because of their adequate balance of powder production and transferred energy for laboratory purposes. The Burgio' model [58] stands out for its simplicity and semi-empirical nature to calculate the total energy transferred ($E_t$) to the powders in a planetary ball mill by means of the following expression:

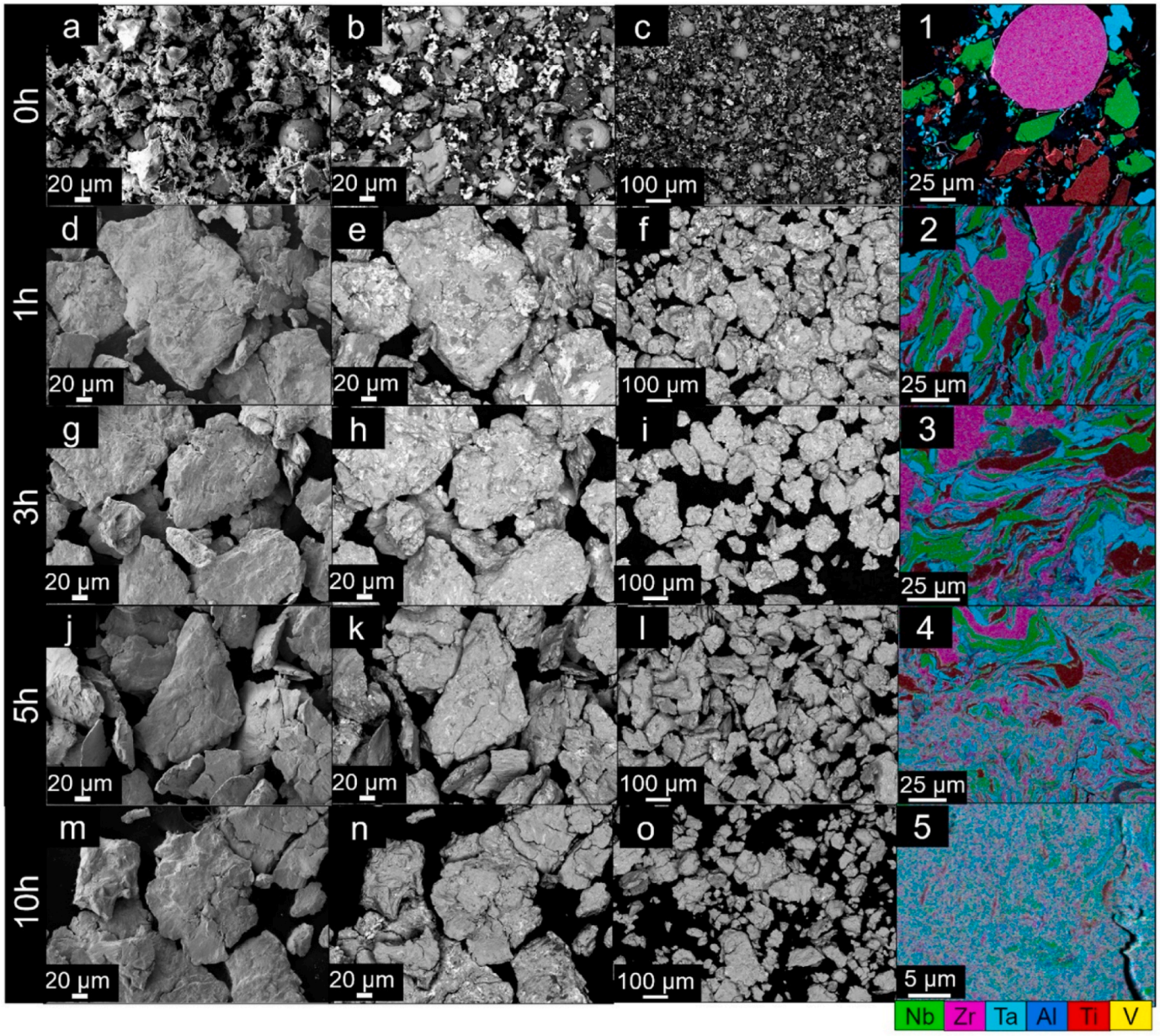


**Fig. 3.** Scanning Electron Microscopy (SEM) images of the $Al_{0.3}NbTa_{0.8}Ti_{1.5}V_{0.2}Zr$ powders obtained with different milling times, indicated in the left border of the image. a), d), g), j), and m) were taken with secondary electrons (SE) detector; the rest were taken with backscattered electrons (BSE) detector. (1–5) Energy-dispersive X-ray spectroscopy (EDS) maps of the cross-section of the respective powders. Reproduced from Ref. [55].

$$E_t = \frac{f \Delta E_b^* n_b}{w_p} t \quad (1)$$

where $f$ is the frequency of impact of balls [58,59], $\Delta E_b^*$ is the energy released by all balls, $n_b$ is the number of balls, $t$ is the milling time, and $wp$ the weight of powder in the vial. The expressions to calculate both $f$ and $\Delta E_b^*$ can be found elsewhere in Ref. [60]. Summarizing, these are function of the ball size and density, the plate rotational speed, the dimensions of the containers, the effective diameter of the mill plate, and the speed ratio between the plate and the containers (these last two depending on each planetary ball mill).

Commonly, RHEAs are constituted by bcc solid solutions, attributed to the nature of their constituent elements. Nonetheless, the amount of energy transferred to the blended powder during MA also plays a role regarding phase transformations. For example, an insufficient amount of transferred energy can conduct to an insufficient alloying process, and the presence of various poorly-alloyed phases will be likely observed, as reported by Kang et al. [40]. Alternatively, metastable crystalline solid solutions may be formed during MA, which will suffer phase transformations during sintering (in order to shift the system towards lower Gibbs free energies). This was described by Zhu et al. [46] studying the TiNbMoTaZr RHEA, where a fully fcc microstructure obtained after 30 h of MA transformed into a bcc + fcc microstructure after sintering. Lastly, metastable non-crystalline solid solutions have been observed after 90 min of MA of the HfTaTiNbZr, which evolved into different crystalline phases after sintering [61], aiming for a lower energetic state.

The MoNbTaVW RHEA exhibited a SPSS after 6 h of MA, presenting a mean particle size lower than 2 μm, using 7 mm-of-diameter WC balls, with a BPR of 10:1 and 300 rpm with no PCA reagent in a planetary ball mill [41]. The fabrication of a similar alloy, MoNbTaW, was described by Roh et al. [62], using an attritor mill (less energetic equipment than the planetary ball mill) with 5-mm-of-diameter stainless steel balls in a

BPR of 10:1, using stearic acid as PCA in a 3 wt %, and a rotational speed of 500 rpm. In this case, the X-ray diffraction (XRD) patterns evidenced that multiphase microstructure is observed, even after 96 h of milling, as depicted in Fig. 4. On the other hand, Pan et al. [49] also reported the synthesis of a MoNbTaW alloy but using a planetary ball mill with WC balls in a BPR of 15:1, a rotational speed of 400 rpm, and acetone as PCA; notwithstanding, only after 60 h of processing a bcc SPSS was observed. The different outcomes reported in these three latter works give a superficial description of how the different parameters can affect phase formation, despite the similar nominal composition. Because of the systemic character of the process, and since the enormous number of degrees of freedom of the process, most of the operational settings of MA are usually fixed based in previous experience of the group or based on conditions commonly used in literature. The single exception of the previous is the milling time, whose effect is commonly studied in order to determine (indirectly) the required transferred energy for desired phase transformations. Fig. 5 illustrates the XRD patterns of a HfMoNbTaTi RHEA powder prepared with different rotational speeds and different BPR, with and without PCA, evaluating the effect of milling time. As can be appreciated, the formation of a bcc SPSS microstructure (that can be quickly identified when the peak of Mo is no longer observed) is obtained at different milling times depending of the rest of the milling conditions: in Fig. 5 a is observed at 40 h, in Fig. 5 b is observed at 30 h, and in Fig. 5 c is observed at 20 h. In these three cases, the BPR was constant but the rotational speed increased from 300 to 350–400 rpm.

Milling time affects not only phase formation but also the particle size evolution, as described by Wang et al. [64] in their study on a MoNbTaTiV RHEA, illustrated in Fig. 6. Elemental powders of the constituent elements were used, all with particle sizes smaller than 74 μm. After 10 h of milling, elemental peaks of Mo, V, Nb, and Ta remain observable yet. However, after 20 h of milling, peaks corresponding uniquely to a bcc solid solution were observed. No remarkable changes in the XRD patterns were observed between 20 h and 40 h of milling. On the other hand, after 5 h of milling, the powder exhibited an average particle size of 343.8 μm. After 10 h and 15 h, the distribution evolved into a bimodal one, with one peak around 300 μm and the other around 30 μm. With further milling time, the particle size distribution turned into a unimodal distribution centered in smaller particle sizes: 22.8 μm after 20 h and 6.8 μm after 40 h. This particle size evolution suggests that the fracture phenomenon predominates during the whole process, typical of brittle systems [56].

The choice of the appropriate milling time for the subsequent stage is also a complex subject. Prolonged milling processes are commonly associated with homogeneous distribution of the constituent elements or SPSS microstructures; nonetheless, it may also conduct to further contamination of the powder, that can end (if uncontrolled) in a poor mechanical behavior in the sintered part. In order to attempt this issue, certain authors have addressed the optimization of the milling time. Kang et al. [40] for example, determined that only 12 h of milling were necessary to prepare the $Al_{0.1}$CrMoNbV RHEA, since after those hours the average particle size and the lamellar spacing were saturated and further milling time had negligible effect on them. Effectively, and despite that the elemental peaks could still be noticed in the XRD pattern of the powder, the SPS-ed part only presented a bcc matrix with fine $Al_2O_3$ precipitates. Moravcikova-Gouvea et al. [55] also determined that the optimal milling time for the $Al_{0.3}NbTa_{0.8}Ti_{1.5}V_{0.2}Zr$ RHEA was 10 h, aiming for a balance between contamination, grain size of the sintered part, and its hardness.

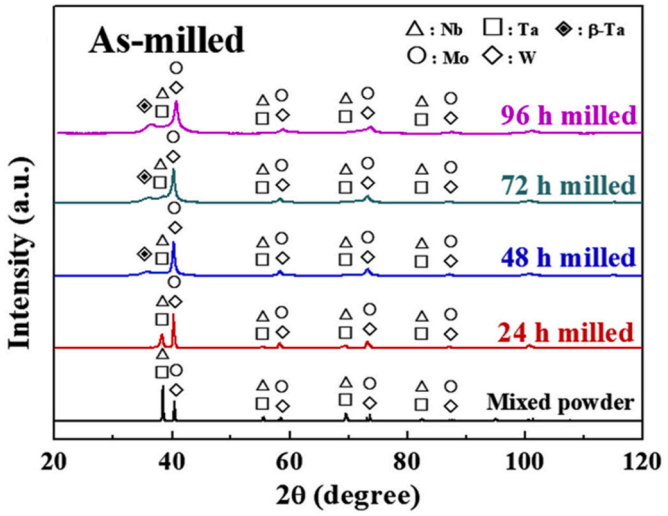


**Fig. 4.** XRD patterns of as-milled powder of a MoNbTaW RHEA as a function of milling time [62]. Reproduced with permission from Elsevier.

One of the main challenges that need to be addressed during the MA of metals is the (generally undesired) powder contamination. This may come from three different main sources: the gaseous atmosphere (reactive gases, like $O_2$ or $N_2$, this last in N-sensitive metals), liquid or solid reagents used as process control agents (PCAs), and the grinding media (such as milling balls and vials). Fig. 7 schematizes an internal view of the vial containing powder and milling balls, in a dry milling scheme (when a solid PCA is employed) and in a wet milling scheme (when a liquid PCA is employed).

Powder materials have larger area-to-volume ratios than bulk materials; hence, they are even more prone to oxidation and nitriding. Therefore, the MA of metals (including the powder handling and loading stages) is typically conducted under inert atmospheres, like Ar, He, (or $N_2$, if there is no risk of nitrides formation) using sealed containers. In the particular case of RHEAs powder fabrication, refractory metals are among the most susceptible elements to form these non-metallic compounds [65]. Therefore, Ar atmosphere has been unavoidable employed during most of the works reporting MA of RHEAs [40,41,49,50,62,66–72]. In some cases, the authors have preferred employing air or $N_2$ as milling atmospheres, either to study their effect or to promote O or N uptake for the formation of non-metallic particles in the subsequent stage [73–75]. Unfortunately, the formation of oxides and carbides is hard to detect in the XRD patterns of milled powders because these compounds are usually contained in small amounts (less than 1 wt %) and possess nanometric sizes.

One of the outcomes of MA is the powder yield, defined as the mass of powder that is extracted after the milling process in comparison to the initial powder loading. The powder yield can be drastically reduced – even to 0 % – because of a superior prevalence of cold welding: particles are not only cold-weld to other particles during MA, but also to the inner walls of the container and to the surface of the milling media. To address this issue, a PCA is commonly considered. Hence, Zhan et al. [63] observed an increase of the powder yield of 24 % by means of the addition of 1 wt % of stearic acid during the synthesis of HfMoNbTaTi powder. Stearic acid is precisely the most commonly used solid PCA, being employed in most of the dry milling processes of RHEAs in dosages between 1 and 4 wt % [45,62,63,67,75–77]. Regarding fully wet milling processes of RHEAs, toluene [78,79], n-heptane [46,80], acethone [49], and isopropyl alcohol [81] have been employed as liquid PCAs.

The effect of PCAs over surface energy and cold welding, additionally results in a reduction of the alloying rate slugging the phase evolution kinetics. Following the previous, Qiao et al. [82] studied the effect of stearic acid and liquid PCAs – ethanol and n-heptane – on the alloying rate and powder yield of a NbTaTiZr RHEA. According to the authors, a powder yield of only 5 % was obtained with stearic acid (with dosages of 0.3 and 30 wt %) after 30 h of milling. Contrarily, the employment of the liquid PCAs increased the powder yield over a 60 %, after 40 and 55 h of milling, respectively. On the other hand, no significant difference in the alloying rate was observed between using stearic acid as PCA and no PCA at all, reaching a maximum value of homogenization degree of 79 %

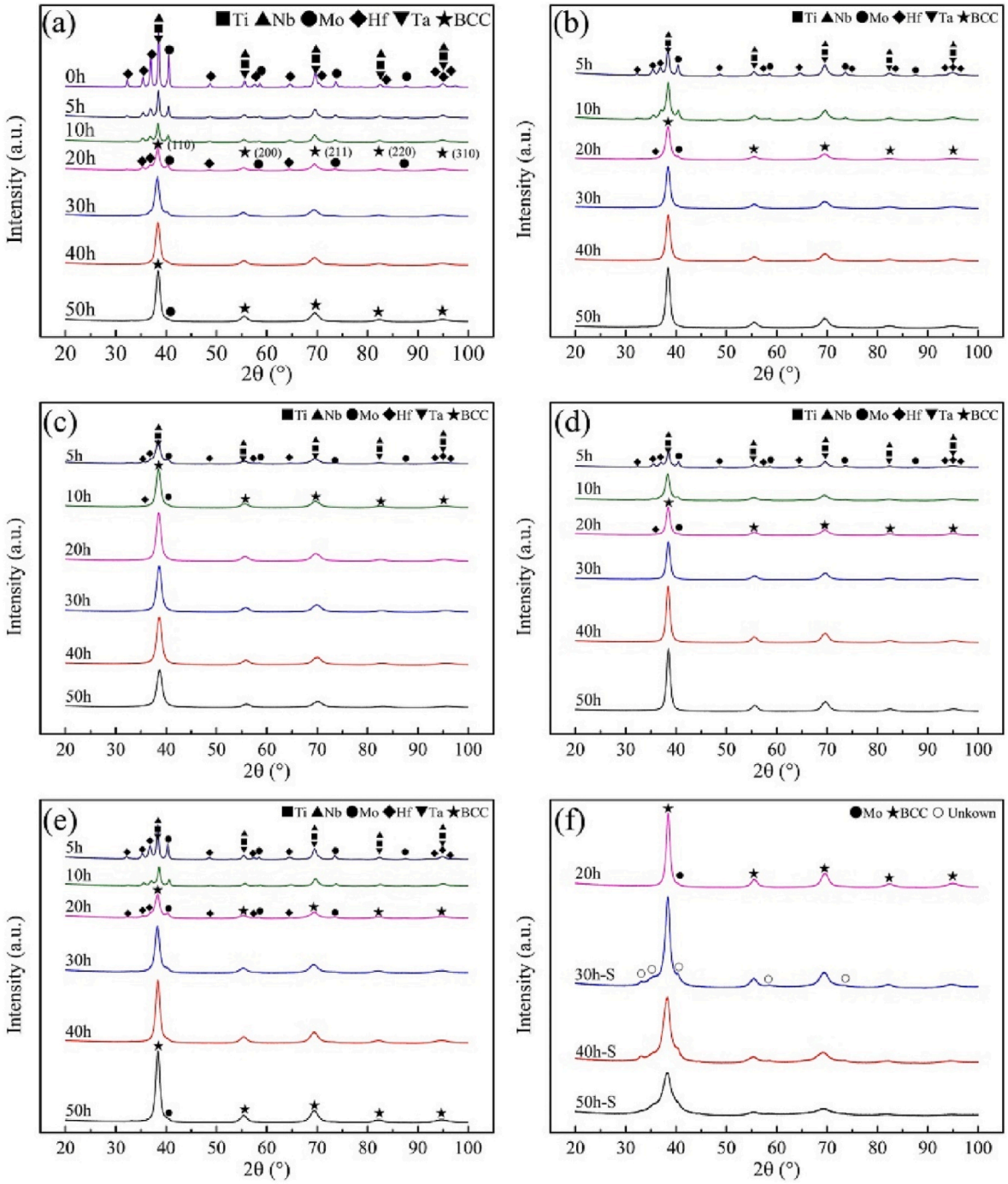


**Fig. 5.** XRD patterns as a function of milling time of HfMoNbTaTi RHEA powders produced using a) 300 rpm and 10:1, b) 350 rpm and 10:1, c) 400 rpm and 10:1, d) 400 rpm and 5:1, e) 400 rpm and 20:1, and f) 400 rpm and 10:1 and stearic acid [63]. Reproduced with permission of Elsevier.

On the other hand, liquid PCAs effectively conducted to slower alloying rates; however, after longer milling times (which were possible since cold welding was controlled), a homogenization degree of over 97 % was observed with n-heptane after 70 h.

The reader may have in mind that all of these compounds are important sources of C, H, and O, and despite of the positive effects of PCA over powder yield, these are an important source of contamination. For these reasons, a considerable number of authors [39–41,44,47,50,64,83–88] have deliberately avoided using a PCA during the RHEAs powder fabrication, unfortunately, without reporting the powder yield. In other cases, an hybrid process has been employed: an initial prolonged stage of dry milling with low dosages of stearic acid [89] or with no PCA at all [19,55,90–92] was conducted (aiming to contains most of the alloying process) followed by a short wet milling process (aiming to recover most of the already alloyed powder). For example, Zhao et al. [19] conducted 60 h of milling without PCA, followed by 2 h of wet milling using high-purity ethanol, while Lv et al. [89] reported 42 h of milling using 0.25 wt % of stearic acid followed by 6 h of wet milling using absolute ethanol. It is important to remind that a subsequent stage of drying (commonly, between 12 and 24 h at temperatures over 70 °C) is required in order to eliminate the liquid PCAs. Summarizing, this strategy could lead to an optimal balance between contamination (by minimizing the dosage of solid PCA during the dry milling stage), powder yield, and milling time.

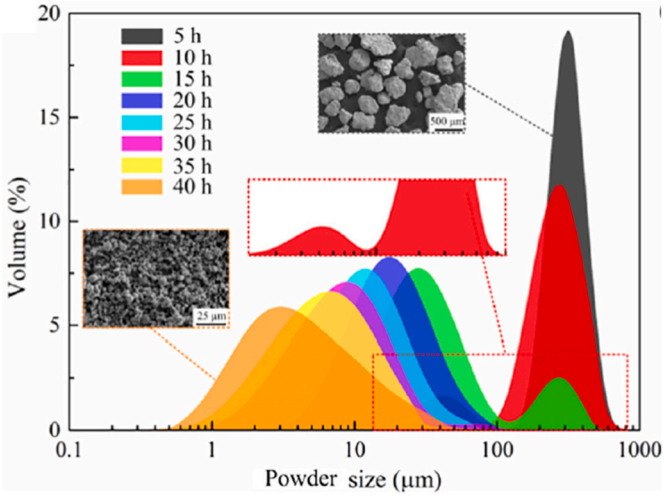


**Fig. 6.** Particle size distribution of milled powders of a MoNbTaTiV RHEA [64]. Reproduced with permission from Elsevier.

It is important to consider at this point, that MA may be conducted starting from blended elemental powders (as has been described in all the articles reporting RHEAs powder synthesis), or by utilizing blends of pre-alloyed powders (that could have been prepared from a previous MA step, this usually described as sequential alloying, or by using other techniques such as atomization) [93]. This last approach has not been employed in the synthesis of RHEAs yet, but there are some reports using sequential alloying in the synthesis of 3d TM HEAs [94–98]. In the case of MA + SPS route, utilizing pre-alloyed powder may reduce the required milling time to obtain a fully-alloyed powder and allows more control for the phase and microstructural evolution; hence, the productivity may be enhanced at the same time that the exposure time to contamination during milling is reduced, potentially conducting to a lower presence of secondary phases in the SPS-ed parts.

In order to avoid contamination from the grinding media, it is recommended that ideally, both container and milling media are made of the same material that will be processed. However, this is not an option in HEA fabrication. In the fabrication of RHEAs powder by MA, Fe-based alloys containers and balls are commonly used because of their low cost and superior availability, despite their low hardness and poor wear resistance [62,68–70,92]. For example, Yan et al. [70] and Shkodich et al. [99] observed, using stainless steel balls and containers, an increment of the Fe content in the solid solution of WMoNbCrTi and NbTaTi RHEA powders, respectively. Various authors have used tungsten carbide balls and containers to fabricate RHEAs powder, avoiding Fe contamination [41,45,49,67,71,78,80,100]. This ceramic material presents higher hardness and wear resistance than Fe-based materials and is not dissolved in the solid solution lattice, as can Fe be. Besides, because of the higher density of WC compared to that of stainless steel, each ball impact transfers more energy, so the alloying kinetics is enhanced too. Even though all these advantages, WC milling media are more expensive than Fe-based milling media, and its unavoidable wear during prolonged milling may result in contamination of the powder. Even more, its presence may promote the formation of multicomponent metal carbides during the subsequent stage [45,71,101]. Another strategy considers a pre-milling stage, in which the inner walls of the containers and the milling balls are coated by a fine layer of powder of a desired composition (or even, a mixture of powders with the nominal composition of the alloy to produce) in order to reduce contamination [41,102].

The BPR parameter correlates the mass ratio of balls and powder. Since the number of balls is usually recommended by the mill supplier – as a function of the container' volume and diameter of the balls – the BPR will determine the nominal grams of powder produced per container per batch. Nonetheless, the parameter is also associated with transferred energy: a low BPR may enhance powder mass production, but the mill is less energetic, since impacts between powder particles and balls will be less frequent. In opposition, a high BPR would promote a larger number of collision events, promoting the alloying. Nonetheless, the frequency of ball-ball collisions is also enhanced, promoting grinding media wear and contamination. For example, Zhan et al. [63] reported an Fe content of 0.49, 1.58, and 7.04 at. % in a HfMoNbTaTi powder milled using BPR of 5:1, 10:1, and 20:1, respectively. BPR values of 10:1 are the most commonly employed in millings using planetary ball mills, since this result in an excellent balance between powder production and transferred energy, with controlled levels of grinding media wear and contamination.

Rotational speed in a planetary ball mill plays a main role in delimiting the nominal kinetic energy of the process. However, an intermediate value should be considered just as with the rest of the operational parameters. A low rotational speed will require a longer milling time since low kinetic energy can be transferred from milling media to powder. On the other hand, a high rotational speed may result in severe contamination due to milling media wear and an increase in the vials' internal temperature (and then increasing the risk of severe cold welding). Shkodich et al. [61] studied the effect of the rotational speed during MA on the phase formation of HfNbTaTiZr RHEA powders after SPS. After 10 h of MA and using 200 rpm of rotational speed, the XRD pattern exhibited a main peak corresponding to a bcc solid solution and the remaining peaks of pure elements. Then, after SPS at 1300 °C and 10 min, a bcc and an hexagonal close-packed (hcp) solid solution were observed. On the other hand, after only 90 min of MA but using 694 rpm as rotational speed, a highly broadened peak was observed in the XRD pattern (corresponding to an amorphized bcc solid solution) and minor peaks indexed as pure Fe. After SPS, the sample also exhibited bcc and hcp solid solutions but accompanied by a Fe-containing Laves phase. Then, even though high rotational speed can reduce the required milling time, the increased wear and the resulting contamination can also influence the phase formation, if not during milling, during sintering.

Collisions and attrition of balls, as well as some exothermic processes occurring at the interior of the milling containers, can increase their inner temperatures accelerating the alloying but also promoting cold

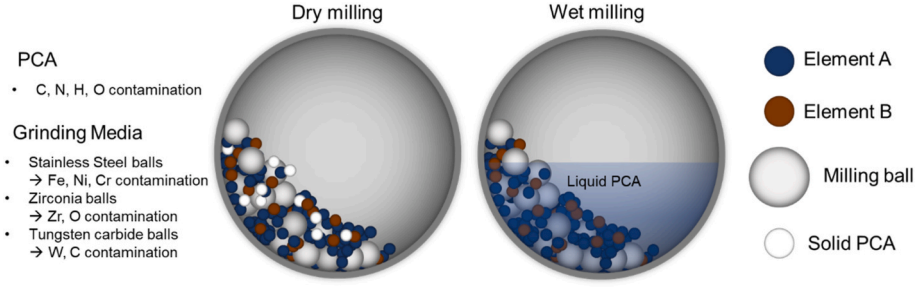


**Fig. 7.** Scheme of dry and wet milling processes.

welding (affecting the powder yield) and contamination. In order to control it, short milling cycles are followed by pauses (aiming to decrease the temperature) in a repetitive manner up to reach the desired effective milling time (referred as on/off cycles). In RHEAs synthesis, on/off cycles of 2:1 [50,74,84,88,103], 4:1 [104], or 1:4 [55] have been employed. Straightforwardly, this strategy conducts to prolonged overall milling times. Alternatively, some containers or mills can be conducted using water-cooling systems, in order to maintain the vial' inner temperature close to room temperature but without a considerable extension of the milling duration.

A promising strategy, especially recommended for powders highly susceptible to suffer cold welding, is cryogenic milling. In these processes, the sealed vials are cooled by cryogenic liquids, such as liquid $N_2$ (that has a boiling point of −196 °C). This will enhance fracture rather than cold welding, reducing the resultant particle size and increasing the powder yield, dispensing with PCA and hence, preserving the chemical purity of the intended alloy. Of course, this technology is associated with its own practical challenges beyond the extra precautions associated with the handle of cryogenic liquids. Smeltzer et al. [83] reported the fabrication of the equiatomic MoNbTaW RHEA by means of cryogenic milling in a modified SPEX 8000 M shaker mill for 8 h in liquid $N_2$, using tool steel grinding media, with no PCA at all. In the sintered state, the sample exhibited complex nitrides in its microstructure, attributed to N contamination.

In a second attempt [105], the authors reported cryogenic milling of the same alloy but using liquid Ar, either with tool steel or WC as grinding media. In that case, negligible N contamination was observed, suggesting that in the first case, liquid $N_2$ leaked during the cryogenic milling due to the shrinkage of the O-rings used between the container and the lid. One of the drawbacks of the cryogenic milling though, is that not only promotes fracture of the alloyed powder, but also of the grinding media. In the latter case, the authors observed severe contamination of either Fe or WC depending on the grinding media; in the case of tool steel grinding media, the contamination of Fe was so severe that an equiatomic MoNbTaWFe resulted from the milling (despite that, initially, the nominal alloy was an equiatomic MoNbTaW alloy).

## 3. Sintering of RHEAs

SPS is employed in most of the cases regarding the consolidation processes of RHEA parts as previously advanced: Fig. 8 a illustrates how over 80 % of the works addressing PM RHEAs employ SPS as the consolidation technique. Then, conventional sintering (CS) and hot pressing (HP) have been used in 4 and 6 works, respectively, to consolidate RHEAs powder. Lastly, HIP and high-pressure sintering (HPS) have been reported in only 1 work each ([66,71], respectively). As mentioned before, the extended use of SPS for the consolidation of HEAs and RHEAs is associated with low sintering time, high densification, and grain growth inhibition, among others [106]. Fig. 8 b, Fig. 8 c, and Fig. 8 d shows the frequency of observation of different values for sintering temperature, uniaxial stress, and holding time employed for the fabrication by SPS of bulk RHEAs parts. First of all, among the operational parameters, the temperature effect is the most studied one, meanwhile

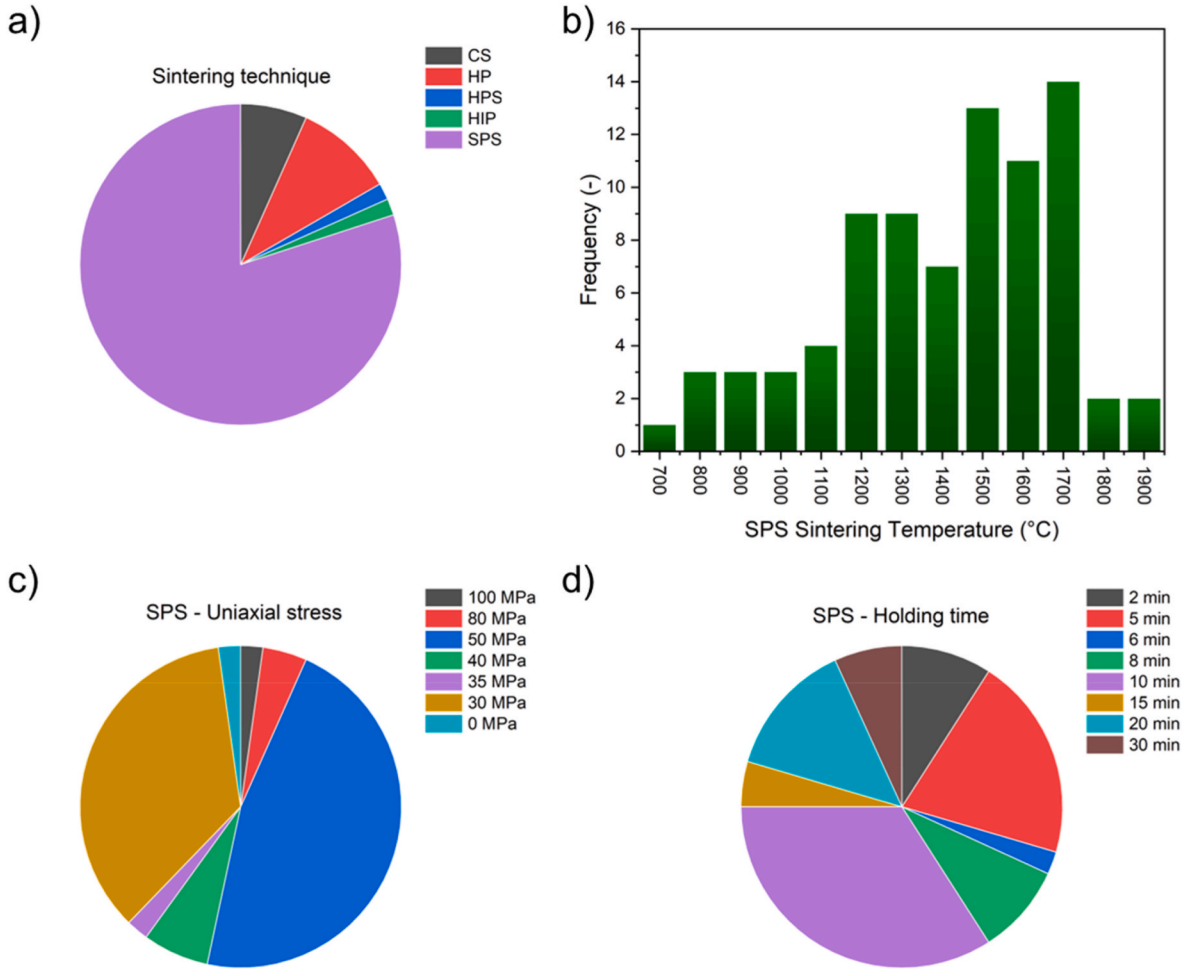


**Fig. 8.** a) Frequency of the different sintering techniques employed in the PM fabrication of RHEAs; b), c) and d) indicates the frequency of the sintering temperature, uniaxial stress, and holding time, respectively, used in the consolidation by SPS of RHEAs.

both holding time and stress are maintained in constant values. As shown in Fig. 8 b, most of the studies are focused in exploring the 1200–1700 °C range; this corresponds to 0.5–0.7 times the melting point (*Tm*) of Nb as a reference (2477 °C). Nonetheless, temperatures as high as 1900 °C have been utilized too. Regarding the uniaxial stress used during the process, two values are mostly employed: 30 and 50 MPa. A particular case is that reported by Han et al. [43] using SPS for the consolidation of MoNbTaW but without the application of any stress. In terms of holding time, an intermediate value of 10 min has been mostly employed, followed by 5 and 20 min. A summary of the conditions used during the preparation of bulk samples of RHEAs through sintering, as well as the main microstructural features of the resulting samples is presented in Appendix B of the Supplementary Material.

One of the challenges of PM parts designed for structural applications is the presence of porosity; this is even more relevant and challenging when CS is chosen as the consolidation technique [66,106–110]. Cao et al. [108] reported densification values of 90 % after CS for 16 h in vacuum at a temperature of 1300 °C during the preparation of TiNb-$Ta_{0.5}Zr$ and $TiNbTa_{0.5}ZrAl_{0.2}$ RHEAs. To reduce it, a longer sintering time or higher sintering temperature is recommended, even though both alternatives increase the cost of the process, promote coarser grain size and expose the sample to more contamination. Malek et al. [109] reported the study of the effect of CS time on the porosity of bulk specimens of a HfNbTaTiZr alloy employing blended elemental powders: a residual porosity of ~8.4 % was observed in the sample obtained after 2 h of sintering, which gradually decreased only up to 5.5 % even after 64 h of sintering. Nevertheless, the sample obtained after 64 h presented oxides that were not observed in samples obtained at 32 h of sintering or less. In a subsequent study, Malek and co-workers [66] studied the effect of the processing route over the densification of a HfNbTaTiZr RHEA. The authors found that powders blended, compacted, and subjected to CS at 1400 °C for 16 h presented a porosity of 6.5 %. However, when they used HIP at 1400 °C for 14 h under a pressure of 190 MPa instead, porosity of 5 % was found. The application of HIP as a posterior treatment in the CS-ed sample conducted to a porosity of 4.5 %, just slightly inferior to that obtained with the single treatments. On the other hand, the samples produced either from powders milled for 42 h or from atomized powders, subjected to SPS at 1300 °C for only 2 min under 80 MPa, presented a porosity of less than 1 %.

The latter observations confirm the superiority of the SPS technology to produce fully-dense parts, either preceded by a MA stage or not, which has been accomplished in various works addressing the SPS consolidation of RHEAs [21,78,101]. Naturally, the sintering temperature plays an important role here too: according to Liu et al. [50], the density of SPS-ed MoNbTaTiV RHEA parts increased from 9.22 to 9.45 g $cm^{-3}$ by increasing the sintering temperature from 1500 to 1600 °C; further raise to 1700 °C did not produce changes in densification though. Similarly, Gao et al. [47] reported that the density of a SPS-ed $TiAlV_{0.5}CrMo$ incremented from 5.62 g $cm^{-3}$ to 5.95 and 5.97 g $cm^{-3}$ when the sintering temperature raised from 1100 to 1200 and 1300 °C. It is important to highlight though, that in most cases the porosity is calculated as the percentual difference between the experimental density and the theoretical one, this last calculated with a rule of mixture of the substitutional constituent elements of the alloy, not considering the differences of density of the formed phases.

Another important feature of the PM route concerns the obtention of ultrafine-grained microstructures: several authors have reported average matrix grain sizes of 1 μm or less in RHEAs fabricated by MA + SPS [38–40,50,84,85]. However, there are some works that describe MA + SPS RHEAs with coarse grain sizes too [111]. The grain size of the matrix phase of MA + SPS samples results from the complex interaction between various aspects of the processing, such as the amount of energy transferred during the milling stage, the sintering temperature and the dwell time, but also, of course, of the alloy composition. Regarding this, Xiang et al. [111] reported that increasing the content of Al (an element that decrease the melting point of RHEAs) in a SPSS $TaNbVTiAl_x$ (with x from 0 to 1) caused an increment of the grain size from 69 to 187 μm, under the same fabrication conditions. Nonetheless, the opposite effect was observed by Zhang et al. [112], who noted that increasing the Al content from x = 0.25 to 1 in an $Al_xCrTiMo$ resulted in a reduction of the grain size, from 48 to 20 μm.

Particularly, all of the ultrafine-grained RHEAs exhibit ultrafine carbides or oxides in their microstructure too: for example, a 3.5 vol % of fcc precipitates of 110 nm of size are observed accompanying a bcc matrix of 0.35 μm of average grain size in the microstructure of a MA + SPS $Ti_{0.5}VNbMoTa$ [85]. In the same way, Fu et al. [67] reported that the matrix grain size decreased from 47 to 31 μm just due to the presence of both coarse and fine $TiC_xO_{1-x}$ particles. Similarly, the addition of just 1 wt % of $ZrO_2$ previous to the milling, caused a reduction of the matrix grain size in SPS-ed samples from 5 to 3.4 μm [113]. Hence, non-metallic particles may have a fundamental role in inhibiting the grain growth of the matrix phases by pinning their grain boundaries.

Moravcikova-Gouvea et al. [55] studied the microstructure of SPS-ed samples of an $Al_{0.3}NbTa_{0.8}Ti_{1.5}V_{0.2}Zr$ RHEA produced from powders milled for different milling times (that means, different amounts of transferred energy). Hence, the authors found that the grain size of the bcc matrix phase decreased with the milling time, from 33 μm (in the sample produced from powder milled for 3 h) to 25.2 μm (in the sample produced from powder milled for 40 h). Apart from that though, it was observed that the fraction of fine precipitates increased with the milling time too. As reported in the previous section, prolonged milling time promotes the uptake of interstitial elements; hence, MA may promote the obtention of fine grain sizes in the microstructure of SPS-ed samples not only by means of powder's microstructure refinement, but also through the increase of the content of interstitial elements that form non-metallic fine particles.

The sintering temperature and dwell time, fortunately, have monotonical effects over grain and secondary particle size: higher temperature and longer times unavoidably promote grain growth [41,45–47,50,69,72]. The reduction of surface energy drives grain growth and precipitate coarsening, and as diffusion-controlled processes, higher temperatures promote faster kinetics. Guo and co-workers [72] reported that the grain size of the bcc matrix phase increases from 24 μm to 38 μm by increasing the sintering temperature from 1500 to 1700 °C. On the other hand, Liu et al. [50] reported the coarsening of Ti-rich precipitates with the increase of sintering temperature during the SPS of a MA-ed MoNbTaTiV RHEAs, as observed from Fig. 9. These increased from 0.15 to 0.28 μm, although their volumetric fraction slightly decreased from 4.9 to 3.9 %. At the same time, the bcc matrix grain size increased from 0.42 to 1.33 μm too. When the size of non-metallic particles increased, the distance between them increased too; that means, the grain boundaries of the bcc matrix can migrates towards larger distances until a particle hinder its movement.

It has been shown that the distribution of the constituent elements in the powder used in the consolidation stage will affect the microstructure, the phase formation, and therefore, the alloy performance. This, in spite of the fact that during the sintering stage any metastable phase already formed in the MA-ed powder will likely transform into a more stable one, because of the effect of the elevated temperatures used during the consolidation step. Shkodich et al. [99] reported that the SPS-ed samples of blended TaTiNb, TaTiNbZr, TaTiNbZrMo, and TaTiNbZrW powder alloys exhibited two bcc solid solutions and an hcp solid solution in all cases, but with a non-homogeneous and coarse microstructure, exhibiting the precipitation of a hcp phase on the grain boundaries of the main bcc phase of the TaTiNbZrMo alloy. The microstructures of these alloys are presented in Fig. 10. On the other hand, all the SPS-ed samples of MA-ed powders of the same alloys (that presented only bcc phases in the milled powder state) exhibited a main bcc solid solution, accompanied by fine oxides precipitates. On top of that, notorious differences can be observed in the microstructure of both alloys, as shown in Figs. 10 and 11.

In the previous section, it was reported that intermediate milling

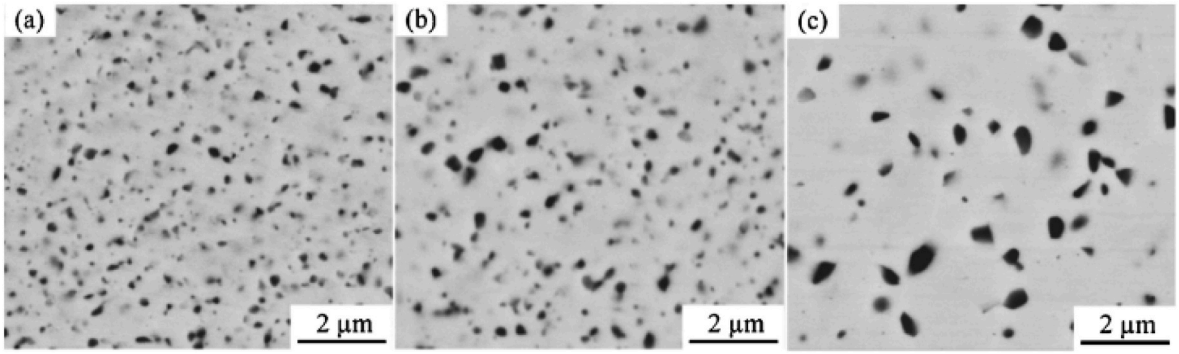


**Fig. 9.** SEM images of sintered MoNbTaTiV RHEAs obtained at a) 1500 °C, b) 1600 °C, and c) 1700 °C, where dark gray precipitates correspond to Ti-rich precipitates [50]. Reproduced with permission from Elsevier.

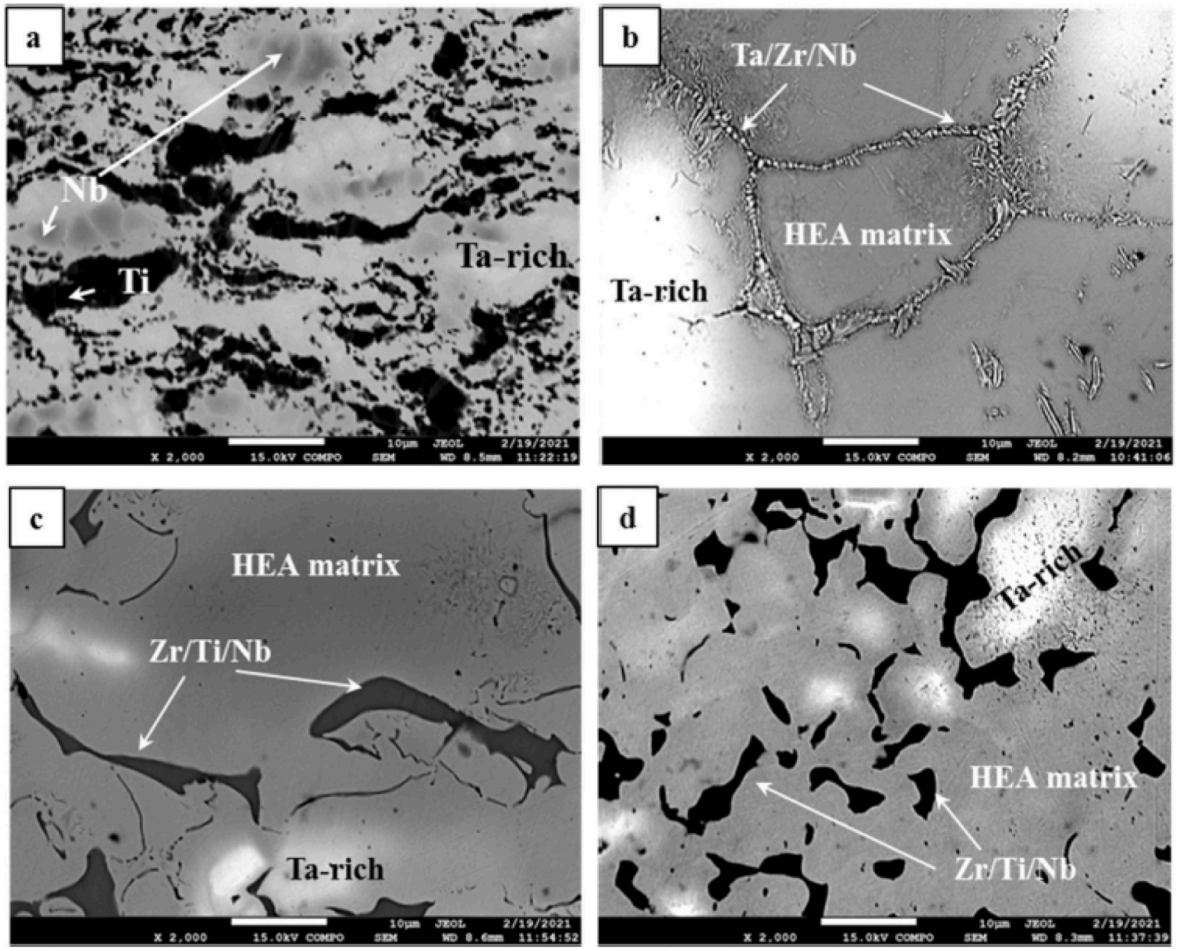


**Fig. 10.** BSE-SEM images of a) TaTiNb, b) TaTiNbZr, c) TaTiNbZrMo, and d) TaTiNbZrW SPS-ed samples obtained from blended elemental powders [99]. Reproduced with permission from Elsevier.

times were optimal in terms of microstructural refinement, homogenization, and controlled contamination. Nonetheless, this can be different for those RHEAs containing elements with high melting points such as W or Ta. Fig. 12a and Fig. 12 b depict the microstructure of a CrMoNbTiW RHEA produced by MA (for 4 h in Ar) and subjected to SPS (at 1500 °C and 50 MPa for 2 min) [75]. Despite a densification of 97 % was reached, W-rich particles were observed in the microstructure, as a signal of a deficient alloying process (whether during milling as in the sintering stage). Similarly, W-rich particles have been reported in Refs. [70,92, 100]. Chen et al. [100] found that W-rich particles were observed in samples produced from powder milled for 4 h and subjected to pressureless sintering at 1250 °C for 2 h, as illustrated in Fig. 13 a. Increasing the sintering temperature conducted to a more homogeneous microstructure with no evidence of W-rich particles (as shown in Fig. 13b and Fig. 13 c). On the other hand, samples sintered at 1250 °C but using powder milled for 16 h presented a totally homogeneous microstructure, as can be appreciated in Fig. 13 d. Accordingly, short milling stages will have to be balanced with sintering at higher temperatures to obtain homogeneous microstructures. Alternatively, incorporating the desired W content by means of pre-alloyed powders in the MA stage may also contribute to a more homogeneous microstructure in these cases.

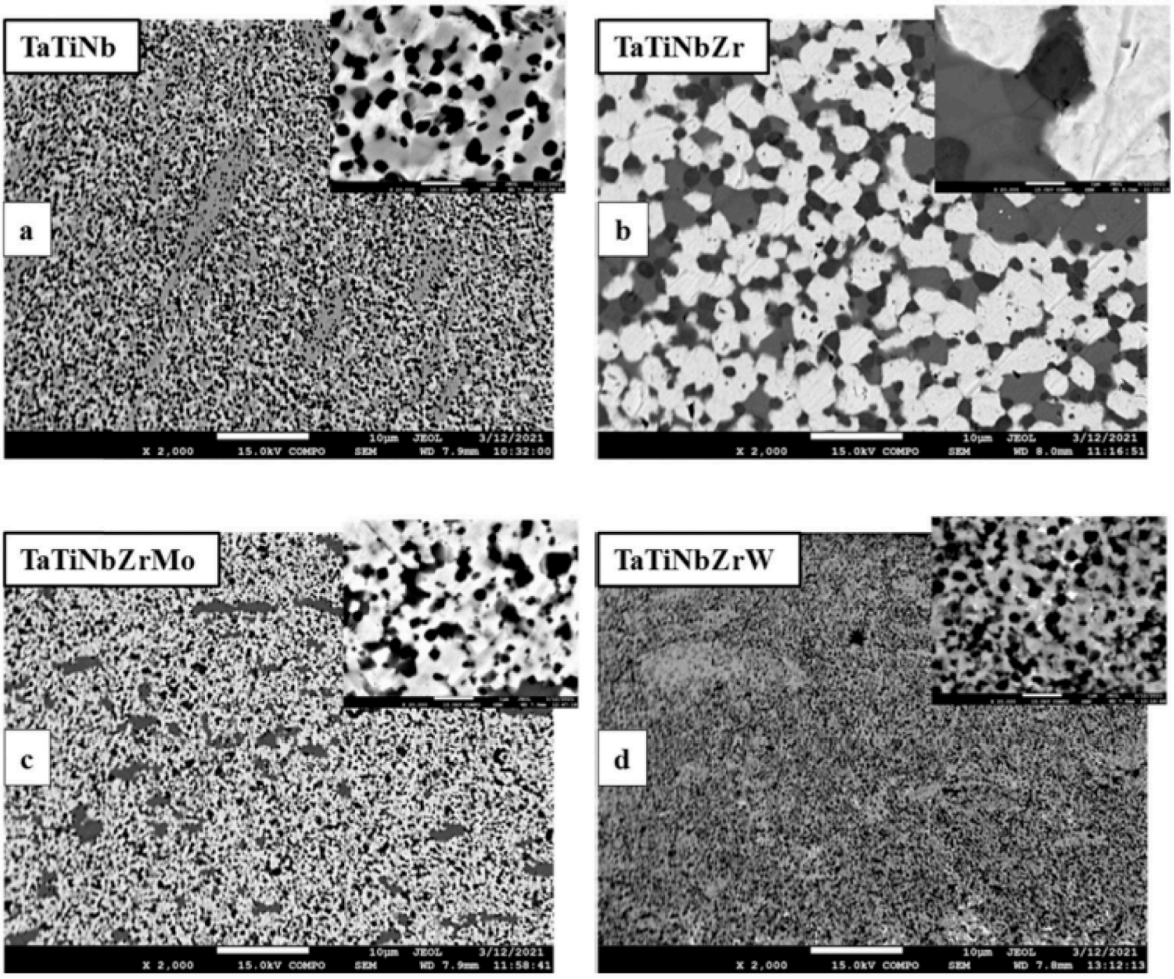


**Fig. 11.** BSE-SEM images of a) TaTiNb, b) TaTiNbZr, c) TaTiNbZrMo, and d) TaTiNbZrW SPS-ed samples obtained from MA-ed powders [99]. Reproduced with permission from Elsevier.

On the other hand, Lukac et al. [114] and Akmal et al. [115] reported the fabrication through SPS of gas-atomized HfNbTaTiZr and plasma-spheroidized MoNbTaTiZr powders, respectively. In both cases, the powders presented a dendritic microstructure with two bcc phases, one of them corresponding to a Zr-rich phase concentrated in the interdendritic regions. After SPS, the two bcc phases and their elemental distribution were maintained. In the first case, the dendritic-like microstructure was also conserved in samples sintered at 800 and 1000 °C. As well, some pores were observed in these samples, while samples sintered at 1200 °C presented only equiaxed grains with no signal of porosity. In the second case, the sintered samples (at 1400 °C) maintained the dendritic microstructure but exhibited full densification. Malek et al. [66] compared the microstructures of SPS-ed samples of a HfNbTaTiZr RHEA prepared from powder milled for 42 h and from atomized powders. The authors found negligible porosity in both samples. Besides, the grain size and O content of the MA + SPS sample were ~10 μm and 1.07 wt %, respectively, meanwhile those of the atomized and SPS-ed sample were ~50 μm and 0.12 wt %. These differences ended in hardness values of 548 and 360 $HV_{10}$, respectively.

The chemical composition possesses the main role in terms of the phase equilibrium of RHEAs. A summary of the microstructural features of sintered RHEAs available in literature, as well as their sintering conditions, is presented in Appendix B of the Supplementary Material. As noted, most RHEAs are constituted by a main bcc solid solution since Mo, Nb, Ta, V, W, and Cr (the most common constituent elements) exhibit that lattice structure as pure elements. Ti, Zr, and Hf additionally seem to promote the formation of hcp solid solutions, associated with the fact that those pure elements present bcc and hcp lattice structures at high and low temperatures, respectively. The formation of Laves phase in RHEAs (the most frequent intermetallic phase in HEAs [116]) is commonly triggered by the presence of Cr. Additionally, Fe promotes its formation too; this is particularly important to consider when ferrous grinding media are used during milling, even if the initial powder mixture does not contain this metal, as previously described. All of these observations, nonetheless, are not exclusive of PM RHEAs, as reported by Miracle and Senkov [4], mostly considering casting RHEAs.

The sintering temperatures also may have a considerable influence over the phase equilibrium. For example, Xin et al. [71] reported that MoNbTaVW samples sintered at 800 and 1000 °C maintained the SPSS bcc microstructure observed in the MA-ed powders, in opposition to those sintered at higher temperatures, where a secondary bcc solid solution was observed. Besides, the XRD patterns evidenced the presence of carbides in the samples sintered above 1150 °C. On the other hand, Guo et al. [72] observed that two phases were formed after sintering at 1500 and 1600 °C in a NbTaTiV RHEA, but only one phase was obtained after sintering at 1700 °C. According to He et al. [102], MoNbTaVW samples subjected to HP presented a bcc phase and oxides microstructure. Increasing the sintering temperature from 1700 °C to 1900 °C reduced the volumetric content of oxides from 20 % to 15 %, as well as their size (from 15 nm to 8 nm), while the $\sigma_{YS}$ increased from 2200 MPa to 2800 MPa.

As described previously, one of the features of the bulk samples

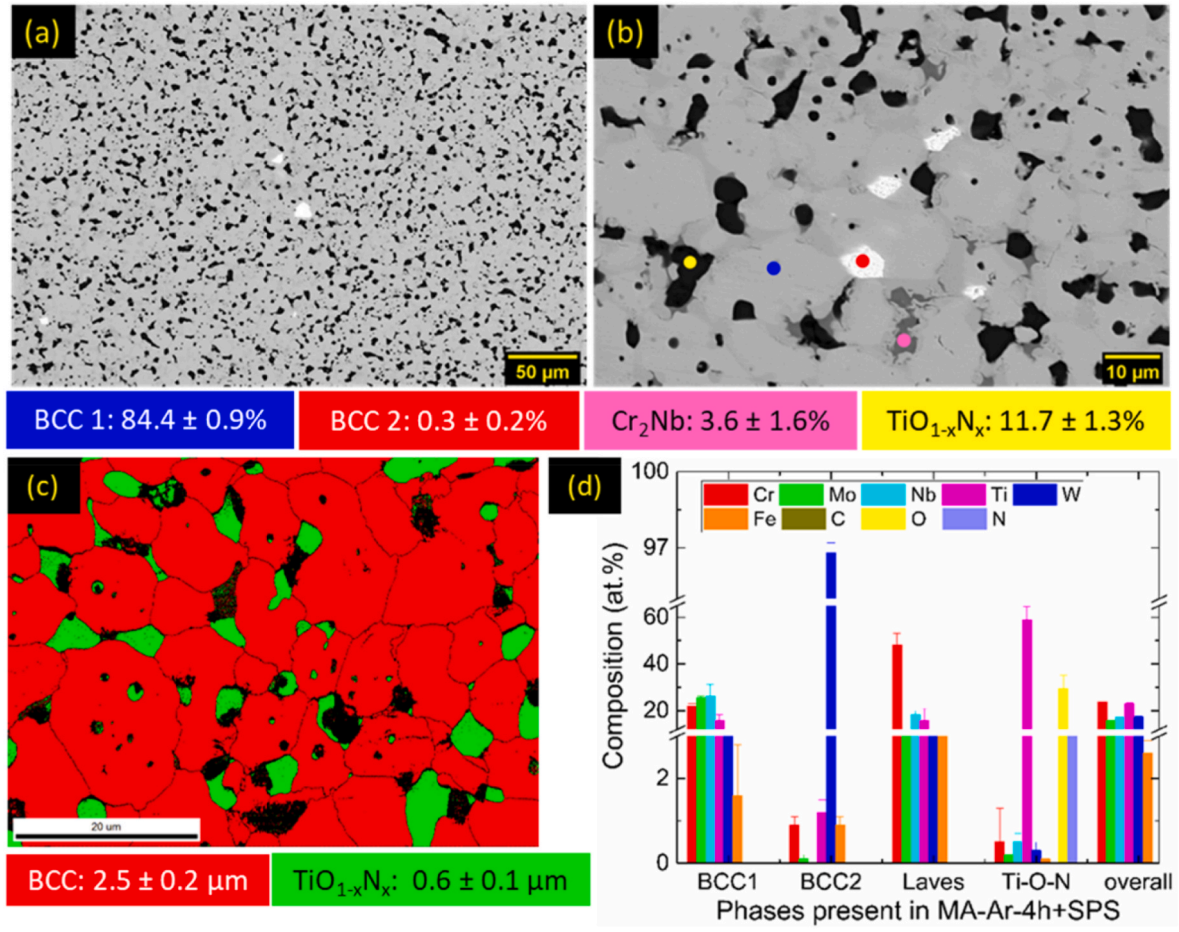


**Fig. 12.** a) BSE-SEM image of the microstructure of a CrMoNbTiW RHEA fabricated by MA and SPS; b) BSE-SEM image of the same sample at higher magnification presenting blue, red, yellow, and pink dots that correspond to the BCC1, BCC2, $Cr_2Nb$, and $TiO_{1-x}N_x$ phases, respectively; c) phase map of the sintered part; and d) SEM-EDS analysis of the phases according to b, showing the elevated content of W in BCC2 [75]. Reproduced with permission of Springer. (For interpretation of the references to colour in this figure legend, the reader is referred to the Web version of this article.)

fabricated by MA and sintering is the formation of finely dispersed non-metallic particles. In RHEAs, the nominal composition of the alloy seems to influence the *in situ* formation of the different species. In Ti-free RHEAs, compounds like $Ta_2VO_6$ [41,69], Ta oxides [62], complex carbides of Nb and Ta [62], and $Al_2O_3$ [40] have been observed. On the other hand, Ti-rich species are mostly observed in Ti-containing alloys. For example, TiO [50,68] was formed because of the presence of O in the atmospheres during MA and SPS. According to Fu et al. [67], adding stearic acid during MA resulted in the formation of $TiC_xO_{1-x}$. Other authors reported the formation of TiC, formed either with [78,117] or without PCA addition [42,118] during the MA stage. Nevertheless, when the alloy contains Zr or Hf (or both), these elements preferably react with O instead (forming compounds like ZrO and $ZrO_2$ [92] or $(Hf,Zr)O_2$ [109]); meanwhile, Ti is kept as a constituent of the metallic phases.

On the other hand, the formation of oxides and carbides in PM RHEAs has a collateral effect over phase equilibrium: their formation implies a depletion of the affected element in the rest of the phases. Hence, Al promotes the B2 formation in casting-produced RHEAs [35,119–121]. However, this situation is less common observed in those fabricated by MA + SPS since most of the Al will preferentially form $Al_2O_3$ rather than constitute any solid solution [40]. In the same way, the lack of available Al dissolved in the main phase will affect the performance of the alloy. For example, increasing the Al content on RHEAs has been proved to enhance the oxidation resistance [122]; this effect would be weakened if Al was already oxidized before exposure to oxidation conditions.

Graphite tools widely used in SPS consolidation of metallic powder materials have been pointed as C contamination sources by several authors [55,118,123–125]. The role of graphite punches and foils use in SPS has been recently analyzed by Smetanina et al. [126] too. Fig. 14 shows a carburized layer formed at the surface of SPS-ed samples of a CrMoNbVW RHEA; this layer seems to be a function of temperature too. The extension of the C contamination from graphite tools and foils used during SPS is still controversial; some authors have suggested that the C uptake is not limited to external carburized layers (as shown in Fig. 14), but to the whole volume of the samples [126]. As a measure to prevent (or limit) C contamination [127], Mo, Ta, or W foils can be used to cover the tooling surfaces that make contact with the powder [66].

Other studies have explored the production of reinforced RHEAs employing *ex situ* addition of oxides and carbides followed by chemical reactions. Li et al. [129] reported the MA of elemental powders of Hf, Nb, Ta, and Zr with TiC particles, the latter as a source of C. After SPS, however, Ti was found constituting the bcc matrix, while Hf and Zr carbides were formed, similar to the findings of Málek et al. [109]. Fu et al. [113] explored the reactive sintering of Nb, Ti, and V elemental powders with $Al_2O_3$ particles, which led to the formation of TiO particles and the dissolution of Al atoms into a bcc matrix. A more complex reaction was reported by Liu et al. [110]; WC, $Mo_2C$, TaC, NbC, and VC powders were milled with Ti elemental powders and then subjected to SPS at 1500 °C. After sintering, the alloy was constituted by a Mo,W, V-rich bcc matrix and coreless carbide grains containing Ti, Nb, Ta, and minor V amounts.

Zhang et al. [127] proposed two alternative routes to prepare RHEA composites, using combustion and reduction processes to produce

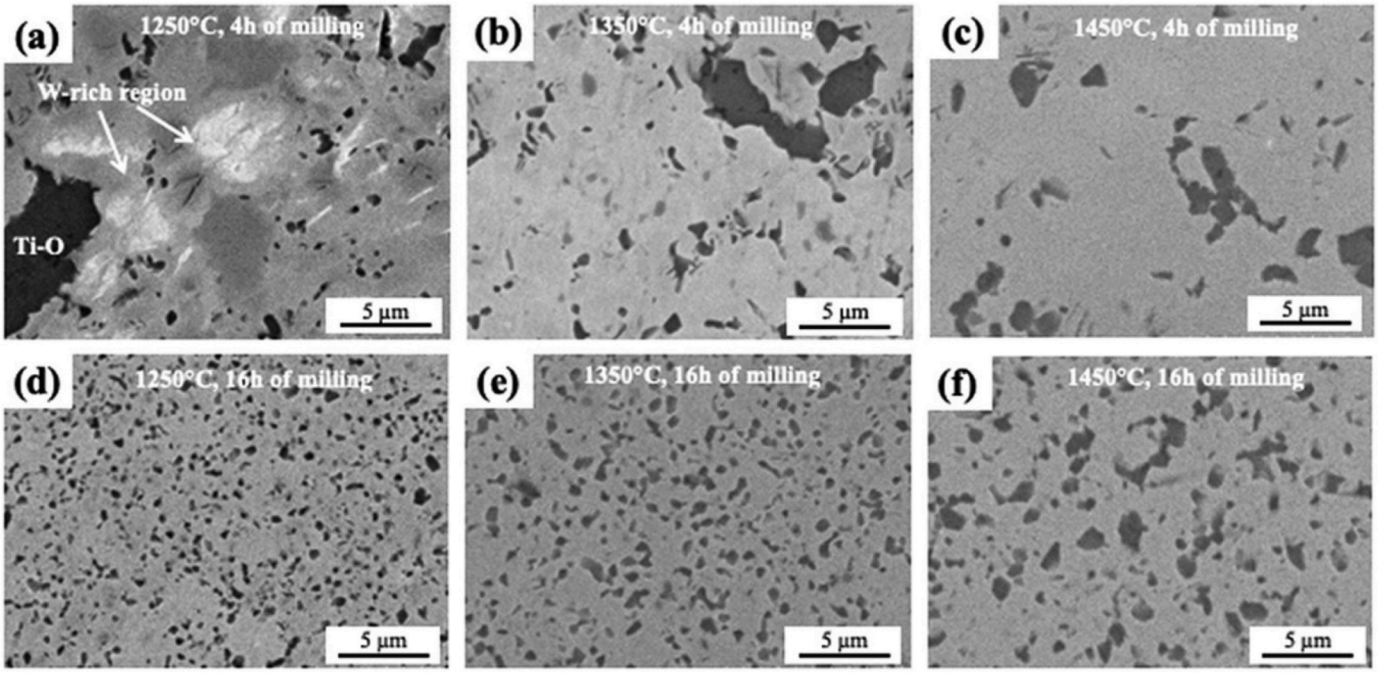


**Fig. 13.** BSE-SEM images of WMoVTiCr samples produced from powders milled for 4 h and sintered at a) 1250 °C, b) 1350 °C, and c) 1450 °C; BSE-SEM images of samples produced from powders milled for 16 h and sintered at d) 1250 °C, e) 1350 °C, and f) 1450 °C [100]. Reproduced with permission of Elsevier.

alloyed powders rather than MA, followed by SPS to consolidate the bulk samples. The authors proposed these routes aiming to produce non-metallic reinforcement particles in a more controlled way than that resulting from using MA. A $(MoNbVTaW)_2O_5$ precursor was firstly prepared by solution combustion and Mg-thermal reduction resulting in a SPSS bcc phase. After SPS, nevertheless, $Ta_2C$ and $TaO_2$ were formed anyways, accompanying the ultrafine-grained bcc matrix. In a second attempt, the oxide precursor was fabricated by combustion followed by nitrogenating it in an ammonia atmosphere, resulting in two fcc nitrides. After SPS, a W,Mo,Ta-rich ultrafine-grained bcc phase and a Nb,V, Ta-rich nitride were formed.

## 4. Room temperature mechanical properties

Fig. 15 represents the room temperature $\sigma_{YS}$ and total deformation ($\varepsilon_T$) values of RHEAs subjected to compression tests, classified by their fabrication route, including RHEAs produced by casting techniques (Casting RHEAs), the different powder metallurgy techniques, and those prepared using additive manufacturing techniques (labeled as AMed in the image). Casting RHEAs are located in the lower half of the graph, comprehending a vast range of $\varepsilon_T$ (from 0 to over 50 %) and of $\sigma_{YS}$ (the only RHEAs with $\sigma_{YS}$ lower than 500 MPa were fabricated using casting techniques [130]). PM RHEAs are characterized by higher $\sigma_{YS}$ but limited $\varepsilon_T$: except one, all of these presented $\varepsilon_T$ lower than 30 %. SPSed RHEAs are the most common among PM RHEAs; they are clustered in the left-top quadrant of the image exhibiting the highest $\sigma_{YS}$ values up to $\varepsilon_T = 25$ % (because no SPSed RHEA sample have achieved a superior ductility than that up to the date of this study). Even more, this route leads to the only three RHEAs with a $\sigma_{YS}$ over 3500 MPa ([46,89]). While CSed and HIPed samples seem to exhibit similar behavior than Casting RHEAs, HPed ones are located in the top border of the Casting RHEAs cluster, exhibiting the highest $\sigma_{YS}$ in the range $25\ \% < \varepsilon_T < 40\ \%$. Lastly, AMed RHEAs are distributed in a narrow $\sigma_{YS}$ band (between 1000 and 1700 MPa) but exhibiting a wide variety of $\varepsilon_T$ values. More importantly, in the case of alloys with $\varepsilon_T \geq 50$ %, those produced by AM seem to outstand those prepared by casting. It is important to mention that despite compression tests are not so adequate as tensile tests to quantitatively compare the ductility of these materials, the different tendencies resulting from the fabrication routes in terms of strength and ductility are quite clear.

Focusing on $\sigma_{YS}$, certain Casting RHEAs overcome the 2000 MPa barrier, such as $Al_{0.5}NbTa_{0.8}Ti_{1.5}V_{0.2}Zr$ [15], $Al_{0.5}Mo_{0.5}NbTa_{0.5}TiZr$ [131], HfNbTaZr [132], and $Mo_{0.5}NbVTi_2$ [133]. The highest $\sigma_{YS}$ of a casting RHEA (2700 MPa) was obtained in a HbNbTaTiZrV RHEA reinforced with $Al_2O_3$ particles [134]. The addition of these particles caused that the grain size of the as-cast part was refined from 80 μm (in the sample without $Al_2O_3$ addition) to 13 μm (in the sample containing 4 vol % of reinforcements). Straightforwardly, the $\varepsilon_T$ did not overcome the 5 %. Hence, it is possible to obtain the typical microstructural features of PM RHEAs through the casting route and with that, get closer to their mechanical properties. In the case of the strongest SPSed RHEAs, a CrMoNbWTi co-doped with N and O outstand but its impressive $\sigma_{YS}$ of 4345 MPa [89]. This however, was obtained with null ductility, revealing a ceramic-like mechanical behavior. The alloy exhibited a multi-phase microstructure containing a bcc matrix (with an average grain size close to 1 μm) and a considerable fraction of nitrides and oxides particles (comprehending in total 45 vol %).

The SPSed RHEAs cluster also presents some outliers that escape from the strength-ductility trade-off trend exhibited by the majority. An $Al_{0.1}CrMoNbV$ RHEA fabricated employing MA and SPS presented a $\sigma_{YS}$ of 2544 MPa and $\varepsilon_T$ of 20 %; using the same fabrication route and the same alloy but doped with 0.015 at. % of B, exhibited an increment of both $\sigma_{YS}$ and $\varepsilon_T$ to 2933 MPa and 26 %, respectively [21]. This is the alloy with the best combination of properties at room temperature among RHEAs, and despite the B doping did not alter the microstructure, it clearly enhances the mechanical performance of the alloy. Other two MA + SPS RHEAs also exhibited remarkable combination of properties, such as a TiVNbMoTa (2208 MPa and 24.9 %) [85] and a $Ti_8Nb_{23}Mo_{23}Ta_{23}W_{23}$ (2377 MPa and 26.3%) [49]. In the case of HPed RHEAs, the most remarkable result was obtained with an $Al_2NbTi_3V_2Zr_{0.4}$ [91]. The alloy was fabricated through 12 h of milling followed by HP at 1250 °C for 2 h under a pressure of 40 MPa, resulting in a multi-phase microstructure containing a bcc matrix and a 14 vol % of a Zr–Al intermetallic compound. Hence, the alloy exhibited the highest $\varepsilon_T$

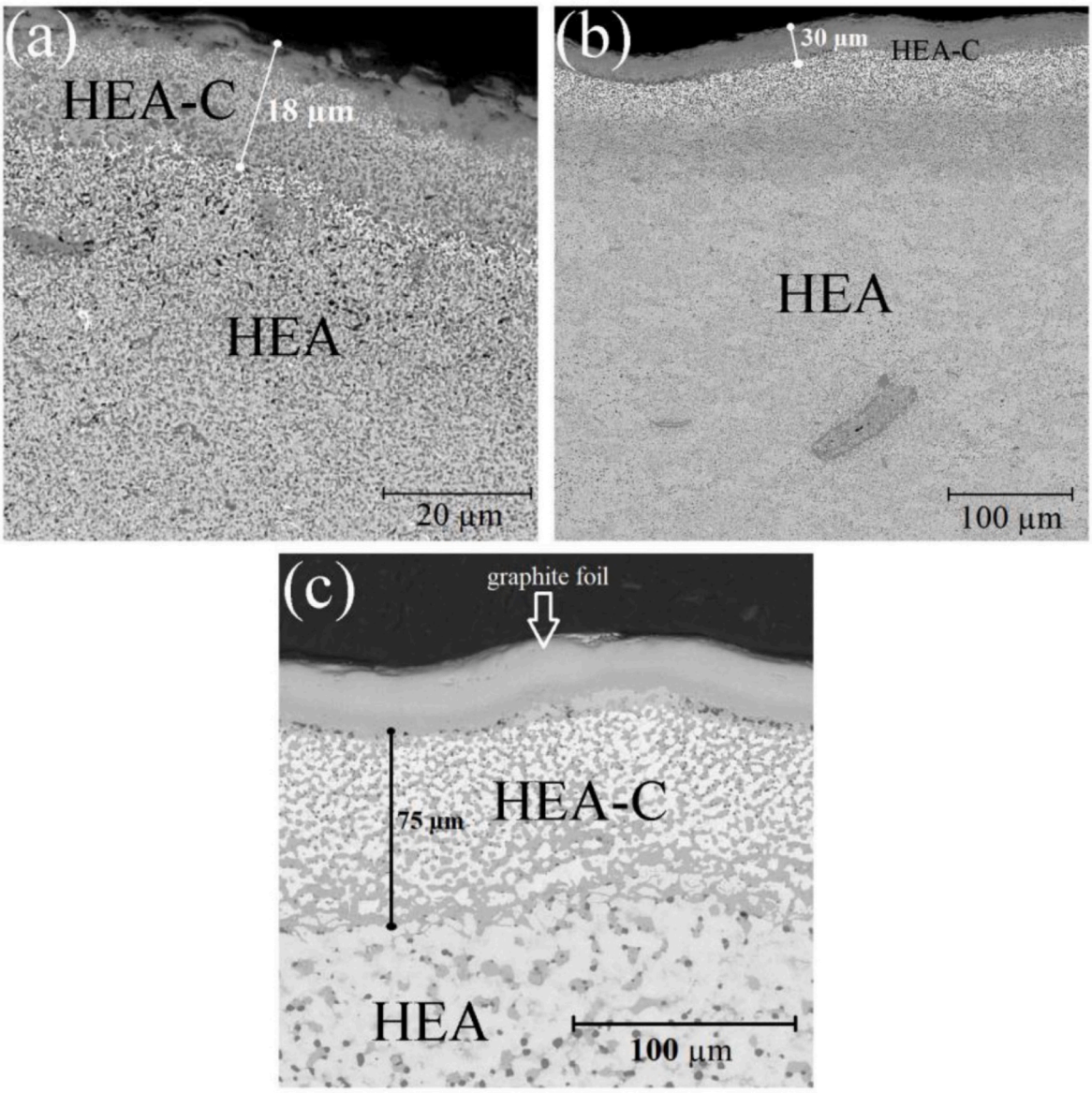


**Fig. 14.** C-rich layers formed at the surface of CrMoNbVW samples subjected to SPS at a) 1200, b) 1300, and c) 1400 °C [128].

among PM RHEAs (38.2 %) with a more than acceptable $\sigma_{YS}$ value (1742 MPa, the highest value in that range of $\varepsilon_T$).

Table 1 summarizes the mechanical properties of some RHEAs fabricated by both PM and casting routes. In all the cases, the $\sigma_{YS}$ of PM RHEAs is superior to those of the casting RHEAs. However, this is counterbalanced by a considerable reduction of ductility in most cases. Notwithstanding, in the case of extremely brittle as-cast RHEAs, the $\varepsilon_T$ of the same alloy produced by PM can be superior. Pan et al. [49]reported the fabrication by MA + SPS of a MoNbTaW RHEA. MA-ed powders were constituted by a single-phase bcc solid solution. After sintering at 1600 °C for 8 min at 35 MPa, the sample exhibited a bcc solid solution with an average grain size of 0.88 µm. Besides, TEM and XRD analysis revealed the presence of a secondary bcc Ta,Nb-rich phase, accompanied by a minor presence of carbides. Compression tests at room temperature resulted in a $\sigma_{YS}$ value of 2460 MPa, overcoming the 1058 MPa of $\sigma_{YS}$ observed in the as-cast MoNbTaW RHEA sample; surprisingly, $\varepsilon_T$ also increased (from 2.6 %, in the as-cast sample, to 16.8 % in the PM one) [9].

From the previous analyses, it is clear that the microstructural features of MA + SPS RHEAs play an important role in their superior room temperature mechanical properties. It is well known that different sources can contribute to the strength of a given alloys and metallic-based composite materials, identified as the strengthening mechanisms. Since all of them affect the strength independently, the following expression can be used for an alloy constituted by a main polycrystalline phase with precipitates in it:

$$\sigma_{YS} = \sigma_0 + \Delta\sigma_{ss} + \Delta\sigma_{iss} + \Delta\sigma_{gb} + \Delta\sigma_{orowan} + \Delta\sigma_{dis} \quad (2)$$

where $\sigma_0$ is the intrinsic strength of the matrix phase, $\Delta\sigma_{ss}$ is the strengthening contribution from substitutional solid solution, $\Delta\sigma_{iss}$ is the strengthening contribution from interstitial solutes, $\Delta\sigma_{gb}$ is the contribution from grain size refinement, $\Delta\sigma_{orowan}$ corresponds to the contribution of fine precipitates, and $\Delta\sigma_{dis}$ to the contribution of pre-existing dislocations.

In the case of SPSS HEAs, the substitutional solid solution strengthening is one of the main sources of strength: since all the different elements constitute a single phase, their different atomic radii and different bonding energies conduct to a superior lattice strain that is translated into an elevated $\sigma_{YS}$ [137]. Nonetheless, this is merely function of the composition, and the contribution of this term will be the same in those

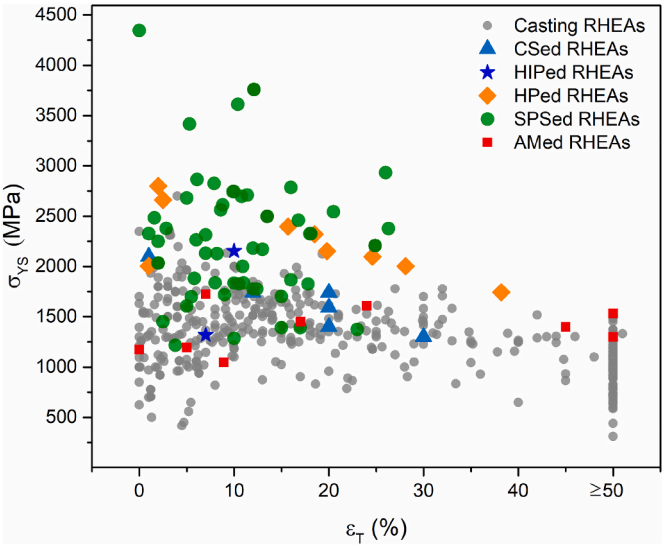


**Fig. 15.** Room temperature $\sigma_{YS}$ and $\varepsilon_T$ of RHEAs subjected to compression testing classified by their fabrication technique: Casting RHEAs groups alloys fabricated by casting techniques; CSed RHEAs groups alloys fabricated by CS; HPed RHEAs groups alloys fabricated by HP; HIPed RHEAs groups alloys fabricated by HIP; SPSed RHEAs groups alloys fabricated by SPS, AMed RHEAs groups alloys fabricated by additive manufacturing. All the alloys whose $\varepsilon_T$ resulted superior than 50 %, or well, whose test was stopped at that deformation value, are included in the ≥50 %. In the rest of the cases, the $\varepsilon_T$ value indicates the deformation at which the sample was fractured.

**Table 1**
Mechanical properties at room temperature of RHEAs fabricated by MA + SPS and casting techniques.

| Alloy | MA + SPS | | | Casting | | |
|---|---|---|---|---|---|---|
| | $\sigma_{YS}$ (MPa) | $\varepsilon_T$ (%) | Ref. | $\sigma_{YS}$ (MPa) | $\varepsilon_T$ (%) | Ref. |
| HfNbTaTiZr | 2620 | 4 | [129] | 929 | +50 | [29] |
| MoNbTaTiV | 2208 | 24.9 | [50] | 1400 | 30 | [135] |
| MoNbTaVW | 2612 | 8.8 | [41] | 1246 | 1.7 | [9] |
| MoNbTaW | 2460 | 16.8 | [49] | 1058 | 2.6 | [9] |
| NbTaTiV | 1373 | 23 | [72] | 965 | +50 | [136] |
| MoNbTaTiVW | 2709 | 11.4 | [68] | 1521 | 14.2 | [68] |

produced either by PM or casting techniques. On the other hand, the dissolution of small atoms in the interstitial sites of the HEAs lattice can cause strain fields that hinders the dislocation glide, increasing the strength of the alloy [80]. Their content may differ in function of the synthesis route: RHEAs powders produced by MA generally present non-negligible amounts of O and C dissolved, as explained in the previous section, usually higher than those of their as-cast counterparts [50,138]. The contribution to strength from interstitial solutes can be expressed as follows:

$$\Delta\sigma_{iss} = Q_{iss} c_m^c \tag{3}$$

where $Q_{iss}$ is a material constant, $c_m$ is the atomic concentration of interstitial solutes in the matrix, and $c$ is an exponent of the model that may take the value of 1/2 or 2/3 [41]. Liu et al. [50] studied the strengthening mechanisms acting in the elevated strength of a MoNbTaTiV prepared by MA + SPS; the sample sintered at 1600 °C presented an interstitial solid solution strengthening contribution of almost 20 % due to its elevated content of N + O, that reached to 4.42 at. %.

The $\Delta\sigma_{gb}$ term also is a fundamental source of strength in MA + SPS RHEAs due to their fine- and ultrafine-grained microstructures. In these cases, the high amount of grain boundaries hinders the dislocation glide, increasing the strength of the material according to the Hall-Petch relationship [139]:

$$\Delta\sigma_{gb} = K_{HP} d^{-1/2} \tag{4}$$

where $K_{HP}$ corresponds to the Hall-Petch constant and $d$ to the average grain size). Kang et al. [40] reported that the $\Delta\sigma_{gb}$ term was almost 37 % of the total strength of an ultrafine-grained $Al_{0.1}$CrMoNbV RHEA reinforced with 5.5 vol % $Al_2O_3$, with a $K_{HP}$ of 811 MPa $\mu m^{0.5}$. Fig. 16 a illustrates how the grain boundaries limit the movement of dislocations, generating pile-ups structures as those indicated with a yellow arrow in the image. A wide range of $K_{HP}$ have been reported in PM RHEAs, from low values such as 240 MPa $\mu m^{0.5}$ [50,67], intermediate values (418 MPa $\mu m^{0.5}$ [47] and 440 MPa $\mu m^{0.5}$ [69]), and high values (1462–1774 MPa $\mu m^{0.5}$ [41], 928–1394 MPa $\mu m^{0.5}$ [103], 984–1568 MPa $\mu m^{0.5}$ [44], and 1245 MPa $\mu m^{0.5}$ [19]).

In turns, the $\Delta\sigma_{dis}$ term can be calculated as follows:

$$\Delta\sigma_{dis} = M\alpha G b \rho_{dis}^{1/2} \tag{5}$$

where $\alpha$ is an empirical constant (equals to 0.38 for bcc phases [21,140]) and $\rho_{dis}$ can be determined experimentally from the broadening of the XRD patterns using the procedure described elsewhere in Refs. [141,142]. Powders produced during prolonged MA processes usually present elevated $\rho_{dis}$ because of the plastic deformation exerted through balls' impacts. During sintering, $\rho_{dis}$ may decrease considerably because of recovery and recrystallization events. Nevertheless, the elevated heating rates, the short dwell times, and the rapid cooling used in SPS may result in an inefficient dislocation anhilitation, preserving an elevated $\rho_{dis}$ even after sintering. Hence, according to Kang et al. [39], the $\Delta\sigma_{dis}$ term presented a considerable contribution of 25 % to the strength of a MA + SPS CrNbMoV RHEA; in opposition, Gao et al. [47] reported a contribution of less than 10 % from this term in the room temperature strength of a MA + SPS $TiAlV_{0.5}$CrMo.

Orowan strengthening contributes to the strength of multi-phase materials, as in the case of intermetallic-containing and non-metallic reinforced RHEAs, by means of hard secondary phases that impede the dislocation glide, demanding higher stresses to overcome them. This is evidenced in Fig. 16, depicting how $Al_2O_3$ nanoparticles hinder the slide of dislocations in an $Al_{0.1}$CrMoNbV RHEA. Additionally, this effect is even greater when a high fraction of hard fine particles are homogeneously dispersed in the matrix (like those observed in PM RHEAs). The strengthening contribution from secondary particles ($\Delta\sigma_{Orowan}$) can be described by Eq. (6 [143] as follows:

$$\Delta\sigma_{Orowan} = M \frac{0.4Gb}{\pi\lambda} \frac{\ln\left(2\sqrt{\frac{2}{3}}\frac{r}{b}\right)}{\sqrt{1-\upsilon}} \tag{6}$$

where $M$ is the mean orientation factor of the matrix phase (that takes a value between 2.75 [39] and 2.9 [144] for bcc lattice structures), $G$ is the shear modulus of the matrix, $b$ is the Burger's vector, $r$ is the mean radii of the particles, $\lambda$ is the distance between particles, and $\upsilon$ is the Poisson's ratio. Accordingly, $\lambda$ is calculated by Eq. (7):

$$\lambda = 2\sqrt{\frac{2}{3}} r \left(\sqrt{\frac{\pi}{4f}} - 1\right) \tag{7}$$

where $f$ is the volume fraction of secondary particles and r the mean radii of the particles.

Nevertheless, several authors have reported limited contribution of these ultrafine secondary particles in the room temperature strength of MA + SPS RHEAs [19,21,44,67,85,103]. For example, Kang et al. [41] reported that the $\Delta\sigma_{Orowan}$ term corresponded only to 1 % of the strength of a MA + SPS MoNbTaVW RHEA, that can be attributed to the low volumetric fraction of the nanoprecipitates (~0.5 vol %). Nonetheless, in the case of a MA + SPS CrMoNbTaVW [69], with a non-negligible 24 vol % of nanoprecipitates of 370 nm of diameter, the $\Delta\sigma_{Orowan}$ term

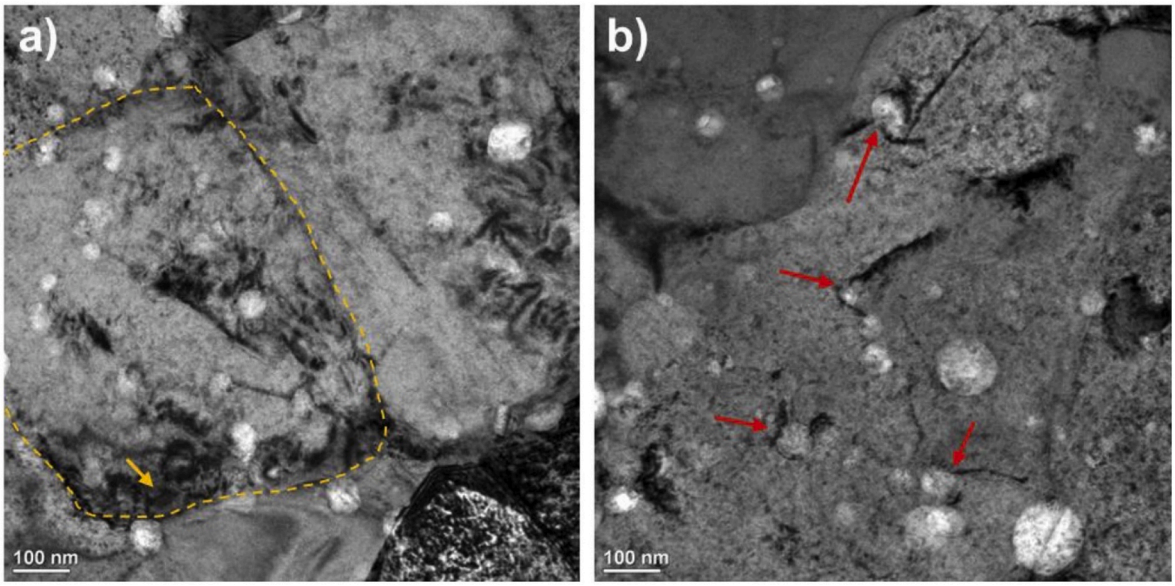


**Fig. 16.** Bright field transmission electron microscopy (BF-TEM) images of the microstructure of an $Al_{0.1}$CrMoNbV RHEA in the as-sintered state [40]. Reproduced with permission of Elsevier.

contributed with only 149 MPa of the 3416 MPa of $\sigma_{YS}$. Despite the poor direct contribution of nanoprecipitates in the strength of MA + SPS RHEAs, their presence may have a preponderant role in inhibiting grain growth [39,145], contributing hence to the alloy strength indirectly through the $\Delta\sigma_{gb}$ term.

According to other authors [101,146–148], the contribution of secondary particles $\sigma_{particles}$ includes more terms that just the $\Delta\sigma_{Orowan}$ effect, being actually calculated as follows:

$$\sigma_{particles} = \sigma_m\left[(1+f_L)(1+f_D)-1\right] \tag{8}$$

where $\sigma_m$ is the yield strength of the matrix, $f_L$ is the factor associated with the load-bearing effect, and $f_D$ is the factor associated with dislocation-related effects; these last two are calculated as Eqs. (9) and (10) indicate, respectively:

$$f_L = f\frac{(L+t)AR}{4L} \tag{9}$$

where L is the length of the particle (measured in the perpendicular direction of the C. A.), $t$ the particle thickness, $AR$ the aspect ratio, and $f$ the volume fraction of $p$ particles. In turns $f_D$ is described as follows:

$$f_D = \frac{\sqrt{(\Delta\sigma_{Orowan})^2+(\Delta\sigma_{thermal})^2+(\Delta\sigma_{GND})^2}}{\sigma_m} \tag{10}$$

where the $\Delta\sigma_{thermal}$ and $\Delta\sigma_{GND}$ terms correspond, respectively, to the stress contribution associated to the mismatch of thermal expansion coefficients between matrix and reinforcements, and to the strength contribution associated to geometrically necessary dislocations (GND) required to accommodate the plastic deformation mismatch between matrix and reinforcements. The first term is calculated as follows:

$$\Delta\sigma_{thermal} = 1.25Gb\sqrt{\frac{12\Delta\alpha\cdot\Delta T\cdot f}{2rb(1-f)}} \tag{11}$$

where $\Delta\alpha$ is the difference between thermal expansion coefficients between matrix and reinforcements, $\Delta T$ is the difference between the last heat treatment temperature and the testing temperature. And the second term is obtained as follows:

$$\Delta\sigma_{GND} = \xi G\sqrt{f\varepsilon b/2r} \tag{12}$$

where ξ is a geometric factor and ε is the strain applied in the matrix phase.

## 5. High-temperature mechanical properties

Fig. 17 depicts the SYS of RHEAs as a function of the temperature classified by the fabrication route; PM RHEAs are individually described according to their composition. The SYS is chosen to illustrate the high-temperature mechanical performance of RHEAs since it summarizes in a single parameter both alloy's strength and density, fundamental aspects for aerospace applications. Just as with Fig. 15, PM RHEAs are located in

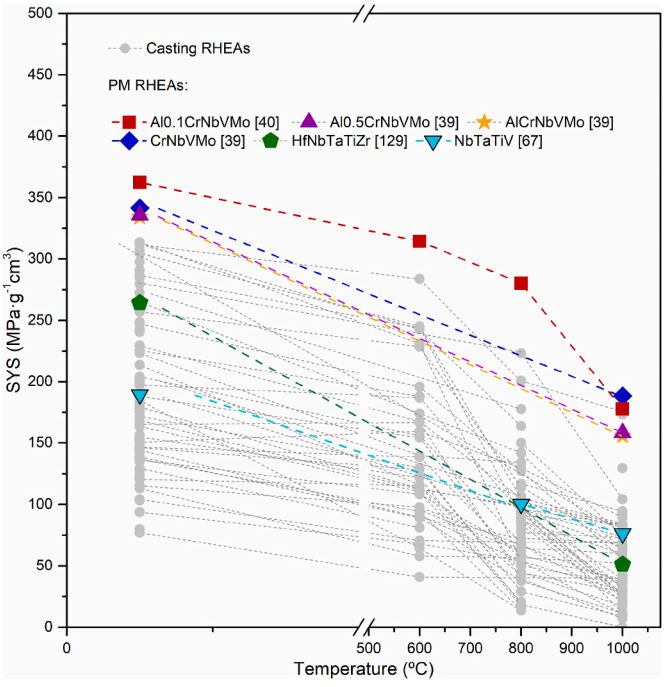


**Fig. 17.** SYS as a function of the temperature of RHEAs reported in the literature. All the values presented in the graph were obtained in uniaxial compression testing with an initial strain rate of $10^{-3}$ $s^{-1}$.

the upper part of the graph, confirming their superior behavior at high temperatures too. As can be clearly appreciated, a very limited number of studies have addressed the high-temperature mechanical performance of PM RHEAs in comparison to those of Casting RHEAs. It is important to highlight that all these PM RHEAs are indeed fabricated through the MA + SPS route. The highest $\sigma_{YS}$ and SYS at 600 and 800 °C corresponds to an $Al_{0.1}$CrMoNbV RHEA fabricated by MA + SPS, reinforced with $Al_2O_3$ particles [40]. The alloy exhibited an outstanding hot softening resistance up to 800 °C since *SYS* decreased from 360 MPa·g$^{-1}$cm$^3$ (at room temperature) to 253 MPa·g$^{-1}$cm$^3$ as is observed in Fig. 17, or in terms of $\sigma_{YS}$, from 2863 MPa to 2213 MPa. Notwithstanding, increasing just 200 °C more, the $\sigma_{YS}$ importantly dropped to below 1500 MPa. Similarly, a PM RHEA CrMoNbV (reinforced with Nb oxide particles) presented a $\sigma_{YS}$ of 1513 MPa at 1000 °C (the highest value among all the RHEAs at that temperature). Nevertheless, a NbTaTiV RHEA reported by Fu et al. [67] and a HfNbTaTiZr RHEA prepared by Li et al. [129] presented just average values of $\sigma_{YS}$ and SYS, either at room or high temperature, even though they were fabricated by MA + SPS too.

The high-temperature flow behavior is the result of the competition between work hardening (increase of the dislocation density) and temperature-activated softening mechanisms, such as dynamic recovery (DRV) and dynamic recrystallization (DRX), that aim to reduce the energy stored in the form of dislocations. During DRV, and because of the high temperature, dislocations can move easily, so pairs of dislocations of opposite signs meet and annihilate each other, decreasing the dislocation density. At the same time, dislocations form a network of high dislocation density walls surrounding cells of low dislocation density, increasing the fraction of low-angle grain boundaries (LAGB). During DRX, on the contrary, fine equiaxial undeformed grains (with very low dislocation density) will nucleate in regions of high energy (as grain boundaries, for example), reducing the area of the previously deformed grains and increasing the high-angle grain boundaries (HAGB) fraction [149]. Hence, in both cases, the dislocation density is reduced [150].

In metals with low and moderate stacking fault energy (SFE), cross-slip is hindered so the annihilation process cannot counterbalance the dislocation generation during the deformation process. Thus, a large amount of energy is accumulated in the material; if a critical amount of deformation is stored ($\varepsilon_c$), DRX will occur, as is commonly observed in fcc alloys like Cu alloys, austenitic stainless steel, and even 3d TM HEAs [151–153]. In opposition, metals with elevated SFE, such as bcc metals and their alloys, commonly present DRV as the main softening mechanism [154–156]. Notwithstanding, various studies regarding high-temperature deformation of bcc RHEAs have reported the occurrence of DRX rather than DRV, including those addressing hot deformation of PM RHEAs [84,157–163]. For example, Fig. 18 illustrates the microstructure of as-deformed HfNbTaTiZr RHEAs after compression test at different strains, evidencing a necklace-like structure of fine DRX-ed grains surrounding unrecrystallized grains, typical of discontinuous DRX (dDRX) [162]. Following the previous, Fig. 19 illustrates TEM images of the microstructure of deformed samples of a MA + HP $AlMo_{0.8}NbTiW_{0.2}Zr$ RHEA. These evidence bulges in the grain boundaries, a phenomenon that precedes dDRX; additionally, dDRXed grains are observed, as well as some resultant from continuous DRX (cDRX) too [164]. All these microstructural features associated with dDRX and cDRX were also observed by Liu et al. [84] during the hot deformation of a MA + SPS MoNbTaTiV.

Fig. 20 illustrates the inverse pole figure (IPF) maps of a MA + SPS MoNbTaTiV RHEA deformed at various conditions of temperature and strain rate [84]. Poor indexation was obtained in samples deformed at the higher strain rate and lower temperatures, likely for an elevated degree of deformation with high fraction of LAGBs and HAGBs. The rest of the images mainly depict equiaxial grains with a low degree of misorientation at their interior, suggesting the occurrence of DRX events. Besides, a subtle majority of blue grains, associated with the <111> fiber, can be appreciated. Fig. 21 depicts the IPF maps of a $AlMo_{0.8}NbTiW_{0.2}Zr$ RHEA deformed at different conditions [164]. Samples deformed at 1150 and 1250 °C and strain rates of 0.01 and 0.001 s$^{-1}$ exhibit considerable misorientation at the interior of the grains, as well as an apparent preferred orientation towards <111> and <100> directions. In opposition, samples deformed at 1350 °C and 0.0001 s$^{-1}$ displayed grains parallel to the <110> directions, indicating a potential change in the deformation texture. Of course, the amount of grains analyzed in these IPF maps are not enough to establish conclusions regarding the texture of the samples. Unfortunately, no extensive analyses of pole figures or orientation distribution functions have been done in PM RHEAs.

Unusual behaviors exhibited by HEAs in comparison to pure metals are not uncommon: recent studies have revealed particularly different roles of edge and screw dislocations in the deformation of RHEAs [165–168]. Commonly, the high-temperature strength of bcc metals and their alloys is governed by the hindered glide of screw dislocations. Nonetheless, some studies have experimentally shown that the fraction of edge dislocations of the bcc phase of RHEAs increased with plastic deformation instead of that of screw dislocations [166,169], in opposition to the conventional ideas extracted pure bcc metals. Hence, it has been proposed that edge dislocations face larger barriers for their movement, controlling the deformation, and providing the high softening resistance of RHEAs [165]. In the same way, recent studies have proposed that short-range ordering (SRO) may have a role in the mechanical behavior of HEAs, affecting (either positively [170,171] and negatively [172,173]) the alloy strength. According to Chen et al. [170], SRO increase the energy barriers for the glide of both screw and edge dislocations in RHEAs, making that the latter ones dominates the deformation. On the other hand, the role and values of SFE in HEAs is still a controversial topic [174–177]. While in pure metals and conventional alloys, the SFE is a single value, in HEAs the SFE possess a localized character associated to the fluctuations of the composition throughout the lattice and therefore a distribution of SFE values can be obtained.

In addition to the microstructural and texture analysis of deformed samples, the derivation of the constitutive relationships for hot forming can be employed to accurately model the flow behavior of metallic materials and determine the involved deformation mechanisms and their corresponding activation energies [178]. For these purposes, various expressions have been proposed: Eqs. (13)–(15) represent the exponential law, the power law, and the hyperbolic sinus law, respectively, that correlate the Zenner-Hollomon parameter (Z, also known as the temperature-corrected strain rate) with the flow stress, at certain conditions of strain and microstructure [179,180].

$$Z = \dot{\varepsilon}\exp\left(\frac{Q_{app}}{RT}\right) = A'\sigma^{n'} \tag{13}$$

$$Z = \dot{\varepsilon}\exp\left(\frac{Q_{app}}{RT}\right) = A''\exp\left(\beta\sigma\right) \tag{14}$$

$$Z = \dot{\varepsilon}\exp\left(\frac{Q_{app}}{RT}\right) = A\ senh(\alpha\sigma)^{n} \tag{15}$$

where $Q_{app}$ corresponds to the apparent activation energy, R to the gas constant, T is the temperature, meanwhile n, β, and n' are parameters of the power, exponential, and hyperbolic sin laws, respectively, $\alpha \approx \beta/n'$, and A, A′, and A″ to dimensionless parameters depending on the initial microstructure. Meanwhile the power law fits the experimental data at low stresses ($\alpha\sigma < 0.8$), the exponential law does it at high stresses ($\alpha\sigma > 1.2$); instead, the hyperbolic sin law can be utilized to cover both stress ranges [180].

The steady-state creep equation (Eq. (16) describes the relationship between the strain rate and the flow stress, considering additional aspects such as the shear modulus (G), the Burger's vector (*b*), the initial grain size (*d*), and the diffusion coefficient *D* (where $D = D_0\ \exp(-Q/$

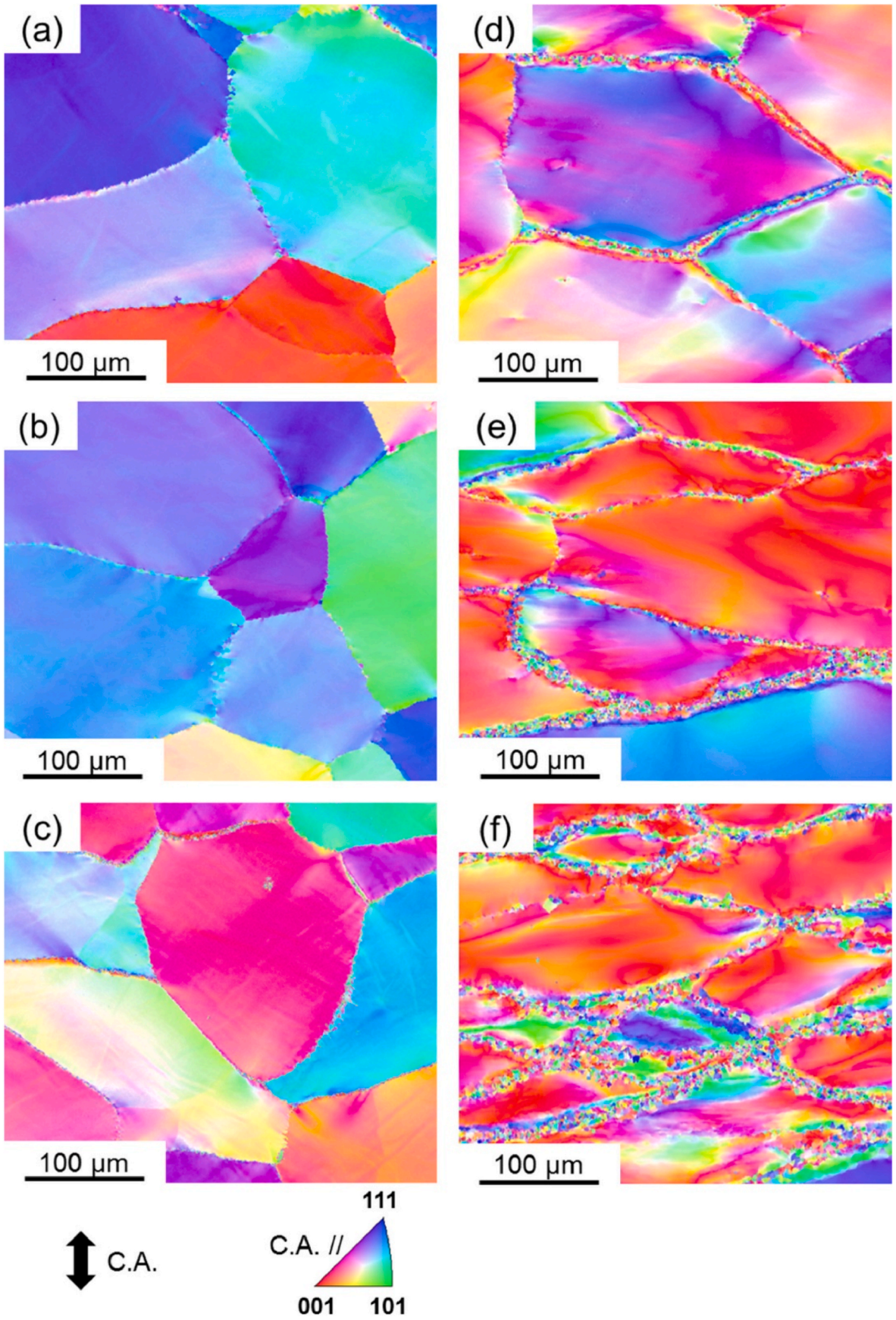


**Fig. 18.** EBSD IPF maps of casting-fabricated HfNbTaTiZr RHEA deformed at a) 0.31, b) 0.32, c) 0.33, d) 0.34, e) 0.35, and f) 0.36 of strain, at 1000 °C with a strain rate of 0.001 $s^{-1}$ under compression testing [162]. The crystallographic orientations are parallel to the compression axis (C. A.) indicated in the image. Reproduced with permission of Elsevier.

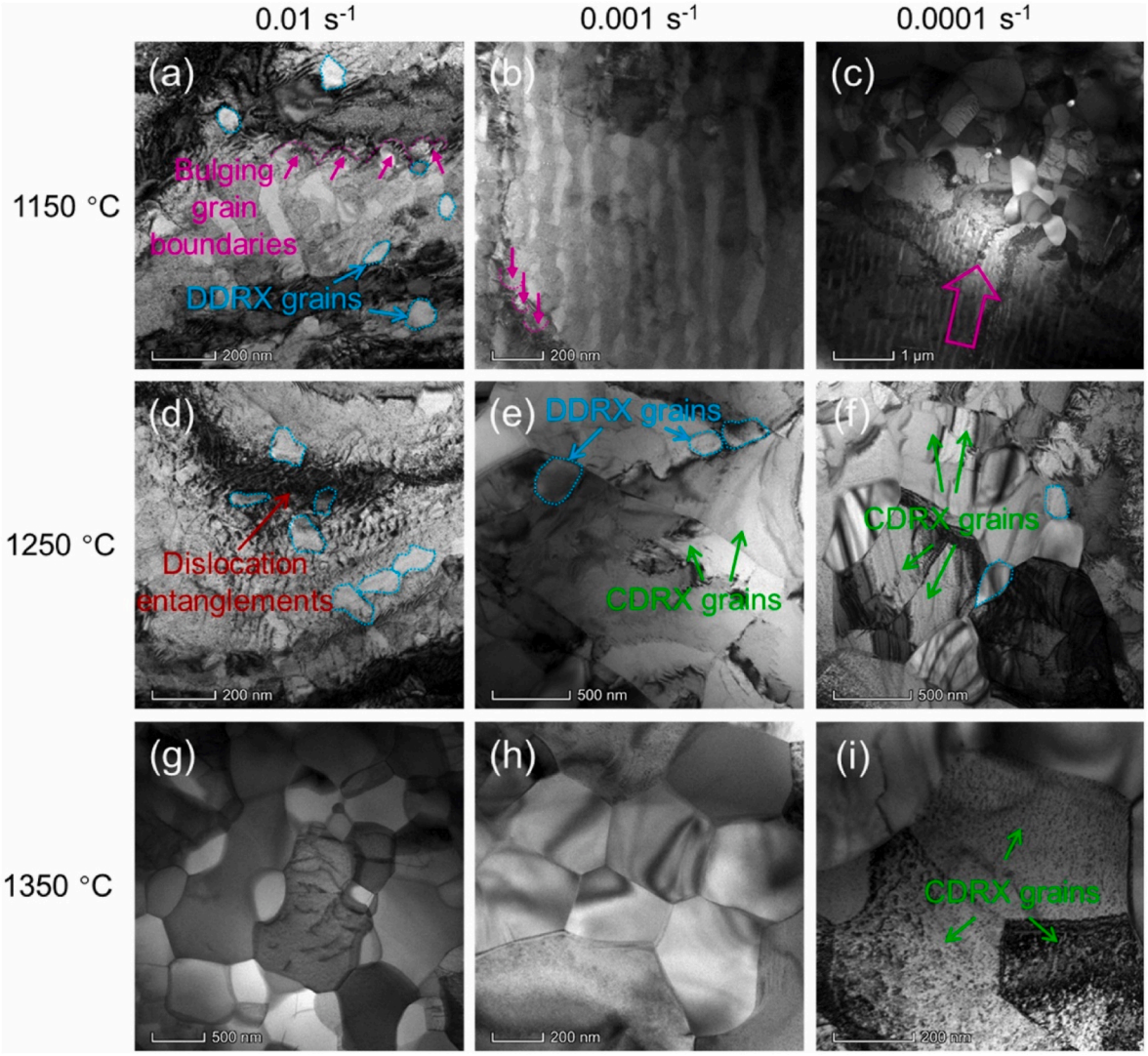


**Fig. 19.** BF-TEM images of a MA + HP $AlMo_{0.8}NbTiW_{0.2}Zr$ RHEA subjected to deformation at various temperatures and strain rates [164]. Reproduced with permission of Elsevier.

*RT)*):

$$\dot{\varepsilon} = \frac{GbD}{kT}\left(\frac{b}{d}\right)^{p}\left(\frac{\sigma}{G}\right)^{m} \tag{16}$$

Additionally, it incorporates the $p$ and $m$ coefficients, which have specific values for each deformation mechanism, as summarized in Table 2. In the same way, depending on the governing deformation mechanism, the activation energy may correspond to that of lattice self-diffusion ($Q_L$), grain boundary diffusion ($Q_{GB}$), pipe or dislocation diffusion ($Q_P$), or solute interdiffusion ($Q_S$). It is evident that the power law (Eq. (13) is obtained by rearranging the terms of Eq. (16). Hence, $n$' becomes equivalent to $m$, and its value relies on the controlling deformation mechanism just as $m$ does, meanwhile $p$ and the grain size dependence are included in the value of $A$'.

Table 3 summarizes the results obtained deriving the constitutive equations of the flow behavior of RHEAs. As can be observed, scarce studies have been done regarding this topic, which are even less frequent for PM RHEAs. Most of these report $n$' values between 3 and 5, indicating that viscous glide and dislocation climb may be the governing deformation mechanism in casting-fabricated RHEAs. In the case of PM RHEAs, $n$' values inferior to 3 were obtained: 2.2 and 2.51 in the case of MoNbTaTiV [84] (fabricated by MA + SPS) and of $AlMo_{0.8}NbTiW_{0.2}Zr$ [164] (fabricated by MA + HP), respectively. Hence, the contribution of GBS to the hot deformation is much more considerable in these alloys than in casting alloys, which is facilitated by the finer grains obtained during PM processing.

On the other hand, the $Q_{app}$ values range between 119 and 403 kJ $mol^{-1}$: Eleti et al. [163] found values of $Q_{app}$ between 232 and 258 kJ $mol^{-1}$ during the high-temperature deformation of a HfNbTaTiZr RHEAs, similar to those found by Senkov et al. [29]. According to them, since $Q_{app}$ was close to the $Q_L$ of Ti, Hf, and Zr, these may control the deformation. However, both groups of authors agreed on the fact that the $Q_L$ of these pure metals will not necessarily be the $Q$ values for the lattice diffusion of these non-traditional alloys, and it may not be as straightforward as in traditional alloys. In traditional alloys, in those cases where lattice diffusion is associated to the controlling deformation mechanism, is the base element that plays the main role in terms of diffusivity, despite the presence or not of solutes. However, in equiatomic SPSS HEAs, it is not possible to make the solute-solvent distinction, and various species (if not all) are involved in the mass transport. Of course, the analysis is even more complex in multi-phase HEAs. On the other hand, there has been some controversy regarding the sluggishness of the diffusion in HEAs [187–191]; even more, some authors have reported an anti-sluggish diffusion in HEAs [190]. In any case, more research is required in this topic to clarify the mass transport behavior of species in HEAs.

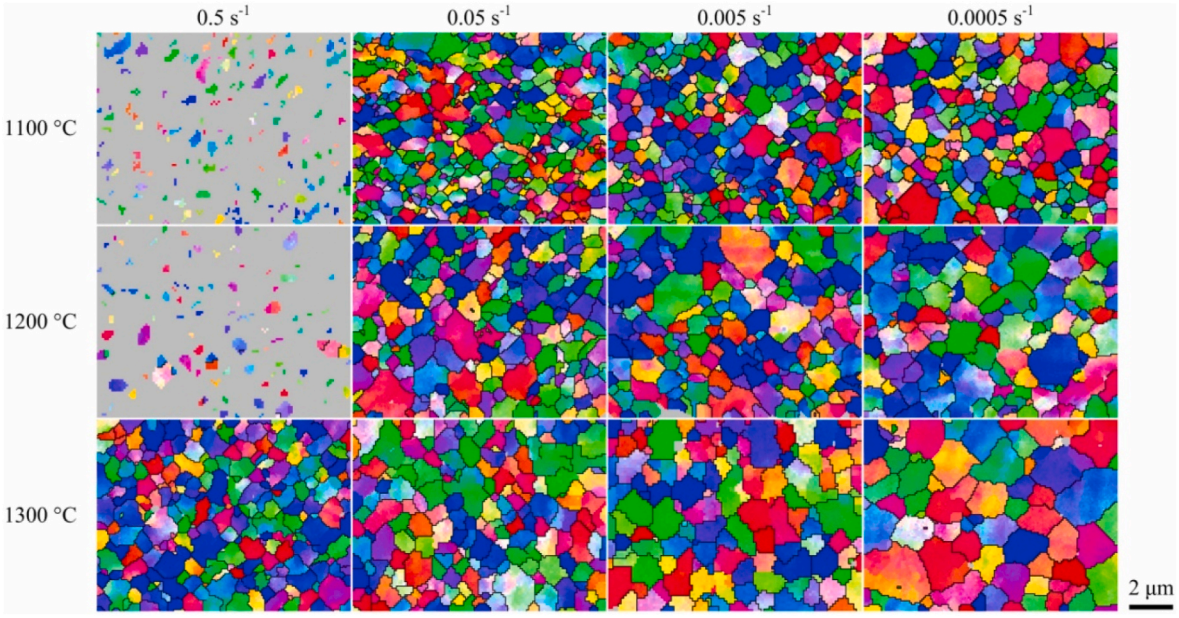


**Fig. 20.** EBSD IPF maps of a MA + SPS MoNbTaTiV RHEA subjected to deformation at different temperatures and strain rates [84]. Reproduced with permission of Elsevier.

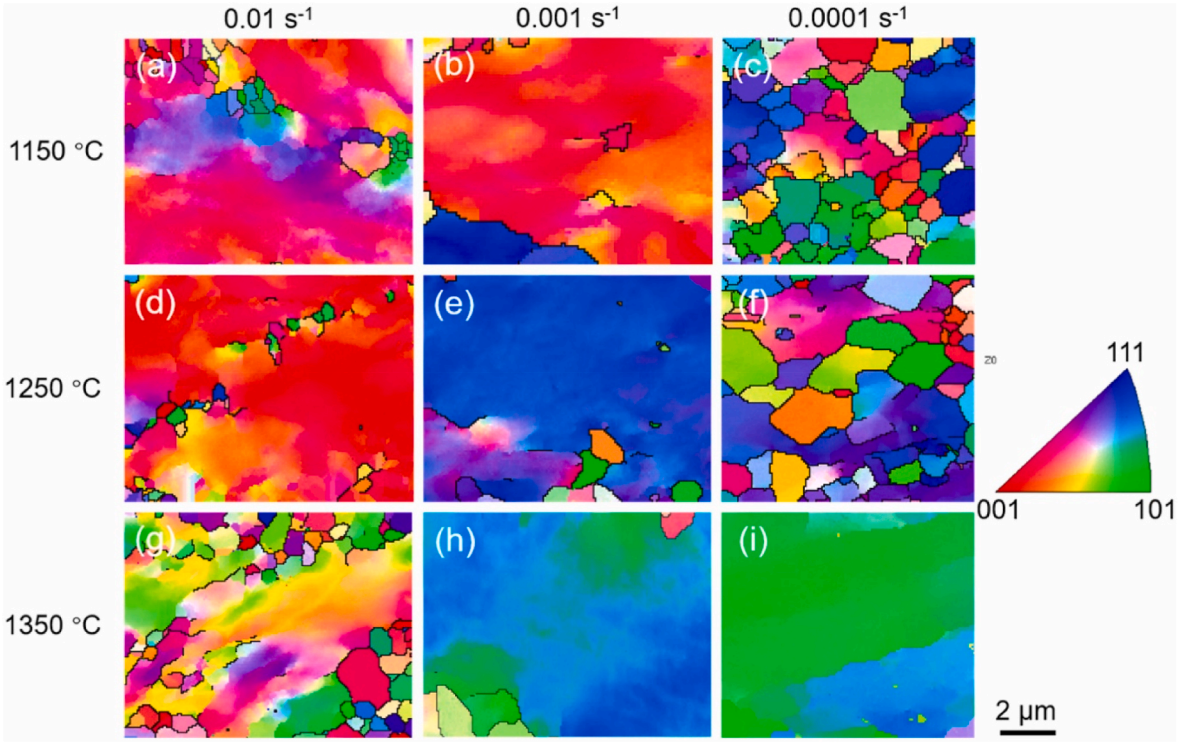


**Fig. 21.** EBSD IPF maps of a MA + HP $AlMo_{0.8}NbTiW_{0.2}Zr$ RHEA subjected to deformation at various temperatures and strain rates [164]. Reproduced with permission of Elsevier.

Returning to deformation mechanisms, ultrafine-grained metals and alloys are commonly deformed through GBS. According to Langdon [192], this is defined as "*the relative displacement of adjacent grains where the grains retain essentially their shape but they become visible displaced with respect to each other*." This mechanism requires accommodation by intragranular dislocation glide at the interior of the displaced grains. Hence, GBS predominance can be determined by means of the derivation of the constitutive equations and a resultant n' ≈ 2, but also through some microstructural hints: retention of equiaxial grain shape (despite the large applied strains) and random textures. The phenomenon is facilitated at elevated temperatures and low strain rates, while all those features that obstacle grain boundary mobility (coarse grain size, presence of secondary particles, grain boundary segregation, etc.) make GBS less favorable.

Thus, hot deformation by means of GBS has been reported in some PM RHEAs; in the case of a PM MoNbTaTiV, the occurrence of this

**Table 2**
High-temperature deformation mechanisms and their corresponding $p$, $m$, and $Q$ values [181].

| Deformation mechanism | $p$ | $m$ | $Q$ |
|---|---|---|---|
| Nabarro-Herring creep | 2 | 1 | $Q_L$ |
| Coble creep | 3 | 1 | $Q_{GB}$ |
| Lattice-diffusion controlled GBS | 2 | 2 | $Q_L$ |
| Pipe-diffusion controlled GBS | 2 | 4 | $Q_P$ |
| GB-diffusion controlled GBS | 3 | 2 | $Q_{GB}$ |
| Solute drag creep | 0 | 3 | $Q_S$ |
| Dislocation climb creep | 0 | 5 | $Q_L$ |

**Table 3**
Summary of constitutive equations parameters for the hot deformation of RHEAs. RHEAs fabricated my PM techniques are clearly indicated in brackets.

| Alloy | T (°C) and $\dot{\varepsilon}$ ($s^{-1}$) range | $Q_{app}$ ($kJ{\cdot}mol^{-1}$) | $n'$ | $n$ | Ref. |
|---|---|---|---|---|---|
| MoNbHfZrTi | 1100–1250 $10^{-3}$ – 0.5 | 326.1 | 3.96 | 2.88 | [182] |
| $AlNbTi_3VZr_{1.5}$ | 1100–1250 $10^{-3}$ – 1 | 228.1 | – | 1.63 | [183] |
| TaNbHfZrTi | 1000–1200 $10^{-2}$ – $10^{-4}$ | 232–258 | 3.03 | – | [163] |
| TaNbHfZrTi | 800–1200 $10^{-5}$ – $10^{-3}$ | 226 | 3.3 | – | [29] |
| $Ti_2ZrHfV_{0.5}Ta_{0.2}$ | 900–1100 $10^{-3}$ – $10^{-1}$ | 119–144 | 3.25 | 2.38 | [184] |
| $AlMo_{0.8}NbTiW_{0.2}Zr$ (MA + HP) | 1150–1350 $10^{-4}$ – $10^{-2}$ | 293–323 | 2.51–2.84 | – | [164] |
| $TiAlVNb_2$ | 1000–1200 $10^{-3}$ – $10^{-1}$ | 375–401 | 4.95 | – | [185] |
| NbZrTiTa | 900–1200 $10^{-3}$ - 1 | 336–403 | 4.31–4.71 | – | [161] |
| MoNbTaTiV (MA + SPS) | 1100–1300 $10^{-4}$ – $10^{-1}$ | 291 | 2.2 | – | [84, 186] |

phenomenon is in agreement with $n'$ close to 2 found through the constitutive relationships derivation. Nevertheless, GBS has not only been reported in ultrafine-grained RHEAs: Eleti et al. [162] reported the GBS had a fundamental role during the high-temperature deformation of HfNbZrTaTi, despite the alloy was fabricated by arc melting and the initial grain size was between 150 and 400 μm. The authors experimentally proved the occurrence of the GBS mechanism (employing marker grids on the sample's surface lately subjected to hot compression) in DRX-ed grains located at the boundaries of coarse unrecrystallized grains. Additionally, they found that the texture of DRX-ed grains evolved into a randomized one with further strain, in agreement with the findings reported by Bai et al. [185], in opposition to unrecrystallized grains that presented the typical textures of bcc metals and alloys (<001> preferred orientations parallel to the compression axis) as well as an elongated shape (as observed in Fig. 18f). Secondly, a strain rate sensitivity index ($m$) of 0.33 was obtained. Although GBS is commonly associated with $m$ values over 0.5, a lower value was expected since the fraction of DRX-ed grains was only a 20 vol % Other studies regarding hot deformation of RHEAs have reported the occurrence of GBS under similar testing conditions [29,193].

On the other hand, the effect of secondary particles over the hot deformation of RHEAs has been studied by Li et al. [129], reporting the high-temperature deformation of (Hf,Zr)C-reinforced HfNbTaTiZr RHEA fabricated by PM. After compression testing, the samples presented $\sigma_{YS}$ values of 2620, 1351, 508, and 105 MPa at 25, 800, 1000, and 1200 °C, respectively. Figs. 22 and 23 show the microstructure of samples after deformation at 800 and 1200 °C. The first sample exhibited inhomogeneous deformation, so three regions were observed according to the microstructural changes: region A, in which no changes were observed (Fig. 22b); region B, in which some cracks were produced in the carbides (Fig. 22c and Fig. 22 d); and region C (that corresponds to a shear band), in which several cracks were produced inside the carbides (Fig. 22e and f). Besides that, the grains of the matrix phase did not suffer any visual modification. The sample deformed at 1200 °C presented homogeneous deformation and hence, exhibited two regions: region A, in which no variation was detected (Fig. 23b), and region B, in which no cracks were observed (neither in the carbide nor in the matrix) although some pores appeared in the matrix-carbide interfaces (Fig. 23c and Fig. 23 d). According to the authors, the elevated $\sigma_{YS}$ obtained at 800 °C was attributed to the load-bearing effect, which was confirmed due to the formation of microcracks in the carbide grains aligned with the compression direction. At 1200 °C, the load-bearing effect is no longer relevant since the elevated temperature gives dislocations

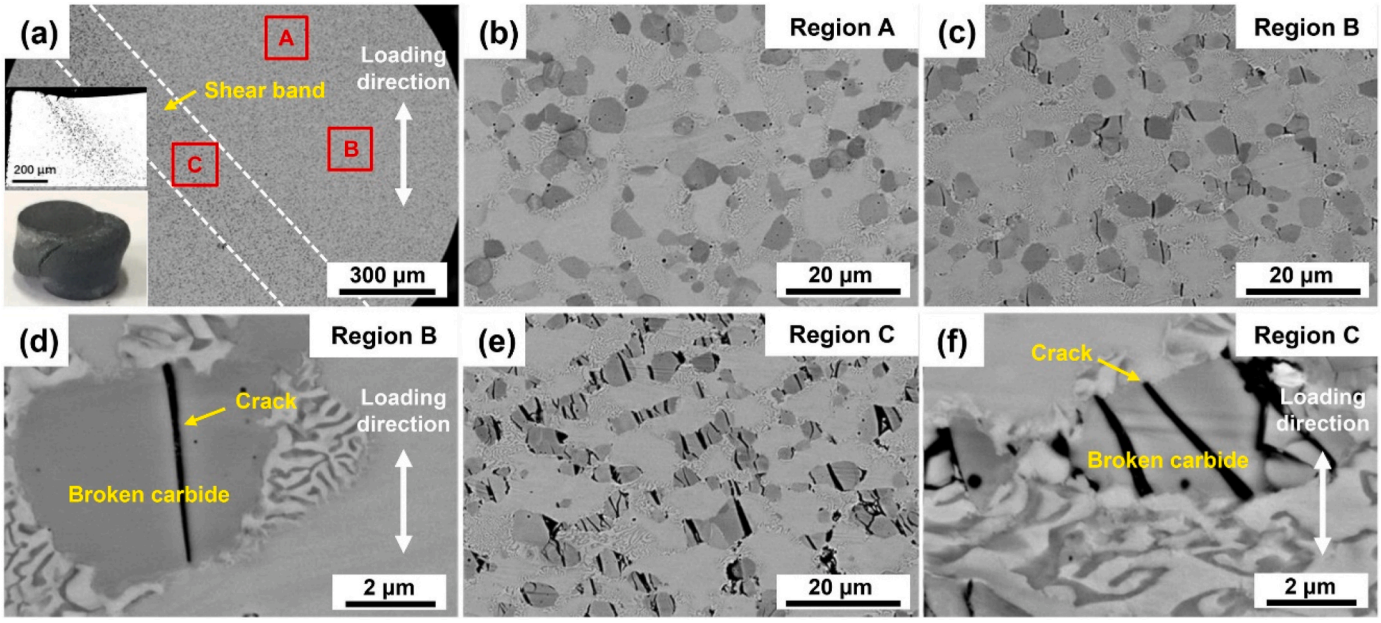


**Fig. 22.** SEM images of a (Hf,Zr)C-reinforced HfNbTaTiZr RHEA after compression test at 800 °C taken at a) low magnification of the sample, b) low magnification of region A, c) low magnification of region B, d) high magnification of region B, e) low magnification of region C, and f) high magnification of region C [129]. Reproduced with permission of Elsevier.

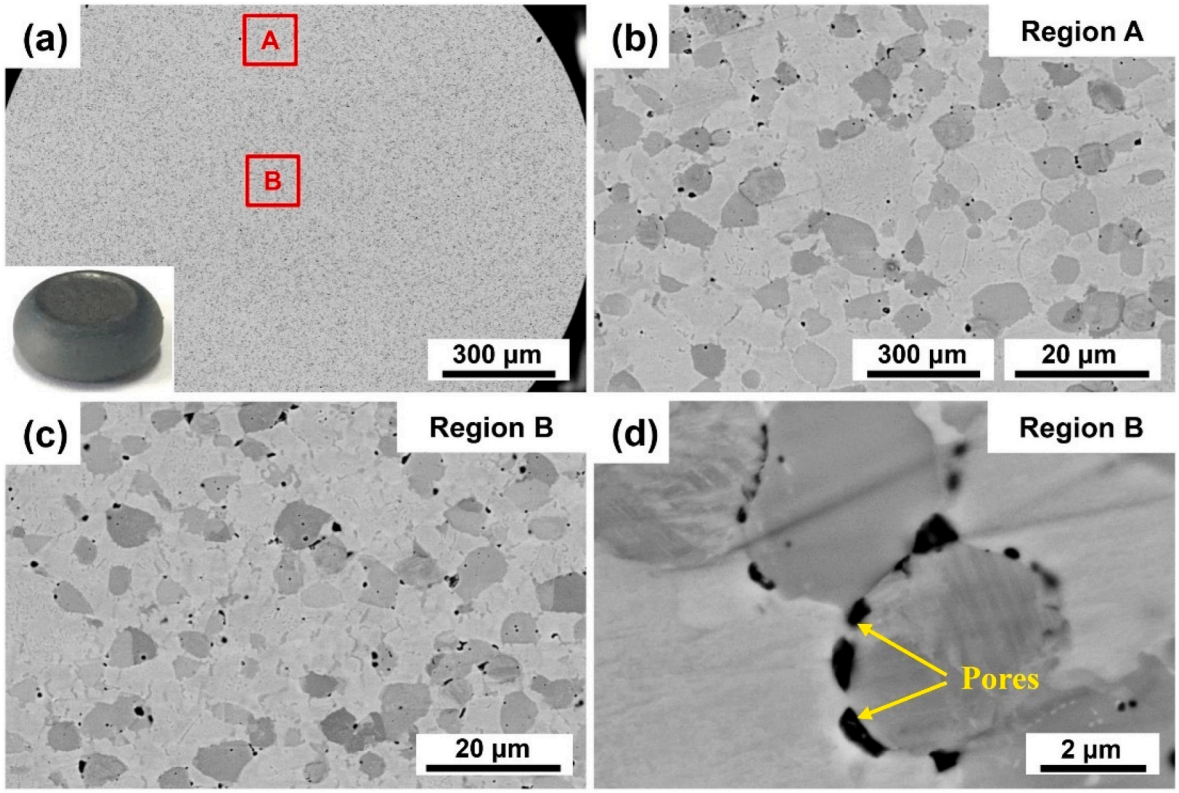


**Fig. 23.** SEM images of a (Hf,Zr)C-reinforced HfNbTaTiZr RHEA after compression test at 1200 °C taken at a) low magnification of the sample, b) low magnification of region A, c) low magnification of region B, and d) high magnification of region B [129]. Reproduced with permission of Elsevier.

enough mobility to overcome them through other mechanisms. Hence, no cracks in the carbide grains were observed. In opposition, the presence of pores at the matrix-carbide interfaces suggests that GBS becomes the dominant deformation mechanism, which would also explain the considerable softening suffered at those temperatures.

It is important to highlight that the presence of secondary particles may affect the derivation of the constitutive equations, resulting in considerably higher $n'$ and $Q_{app}$ values [194,195]. This approach has not been employed yet in PM RHEAs, but some authors have considered this issue in multi-phase HEAs [196–198]. In order to determine the effective stress acting over the deformable matrix, an internal stress ($\sigma_0$, or threshold stress) is considered, as Eq. (17) describes [195,199,200]:

$$Z = \dot{\varepsilon}\exp\left(\frac{Q_{app}}{RT}\right) = A\ senh(\alpha(\sigma - \sigma_0)^n \quad (17)$$

According to Cabrera et al. [200], $\sigma_0$ may arise from the interaction between dislocations and secondary particles, either from remaining Orowan loops or attractive forces between them. Nevertheless, in the case of the previously mentioned PM RHEAs, the resultant $n'$ and $Q_{app}$ are not considerably superior to the values obtained with the rest of RHEAs. Even though this may be associated with the ultrafine-grain character of PM RHEAs (and the similar size scale of bcc grains and secondary particles), more studies are needed to conclude it.

## 6. High-temperature oxidation behavior

Waseem et al. [42] reported the mass gain in isothermal treatment at 1000 °C in air of the WTaVCr and $Ti_7(WTaVCr)_{93}$ RHEAs fabricated by SPS of blended elemental powders. The authors reported parabolic oxidation kinetics, with a mass gain of 75 mg $cm^{-2}$ and 30 mg $cm^{-2}$, respectively, after 3 h of exposure. In both cases, a complex oxide layer was formed, constituted by several oxidized species; in terms of thickness, the addition of Ti caused a thinning of the oxide later from 1.16 mm to 0.22 mm.

In a similar way, Kanyane et al. [201,202] reported the oxidation behavior of equiatomic TiAlMoSiW and non-equiatomic $Ti_{0.25}Al_{0.2}Mo_{0.2}Si_{0.25}W_{0.1}$ RHEAs, prepared by SPS of blended elemental powders employing different sintering temperatures (800, 900, and 1000 °C). An heterogeneous microstructure was obtained in all the cases, indistinctly of the sintering temperature or the nominal composition, presenting W- and Si-rich bcc phases, as well as Ti-rich and Mo-rich silicides. The oxidation behavior was studied through thermogravimetry subjecting the samples to temperatures between 45 and 900 °C, using a heating rate of 10 °C/min in air. In all the cases, the mass gain started around 500 °C; nevertheless, different mass gains were obtained according to the sintering temperature. In both alloys, it was observed that increasing the sintering temperature conducted to a reduction of the total mass gain (from ~2 wt % in samples sintered at 800 °C to ~0.9 wt % in samples sintered at 1000 °C).

On the other hand, Yan et al. [203] studied the high-temperature oxidation behavior of an equiatomic WTaNbTiAl RHEA prepared by MA + SPS. The initial microstructure presented a main bcc phase with an average grain size of ~29 μm, accompanied by W- and Ti-rich phases, as well as alumina particles. Thermogravimetric studies in air were performed to study the oxidation mechanisms, subjecting the samples to an isothermal treatment at 1000 °C for different times (0.5, 12, 24, 36, and 48 h), characterizing the oxidation layers of each of the oxidized samples. The authors reported a two-step oxidation process, with logarithmic and linear rates between 0 and 0.5 h and beyond 0.5 h, respectively. Hence, after 48 h of exposure, a total mass gain of 31.83 mg $cm^{-2}$ was obtained, located in the intermediate range of mass gain among RHEAs, as can be appreciated in Fig. 24.

In terms of the oxide layer structure, three regions were distinguished in all the samples: an outer layer, an internal oxidation front, and a transition zone, as schematized in Fig. 25. It was observed that the total thickness of the oxide layer increased from 120 μm after 12 h of

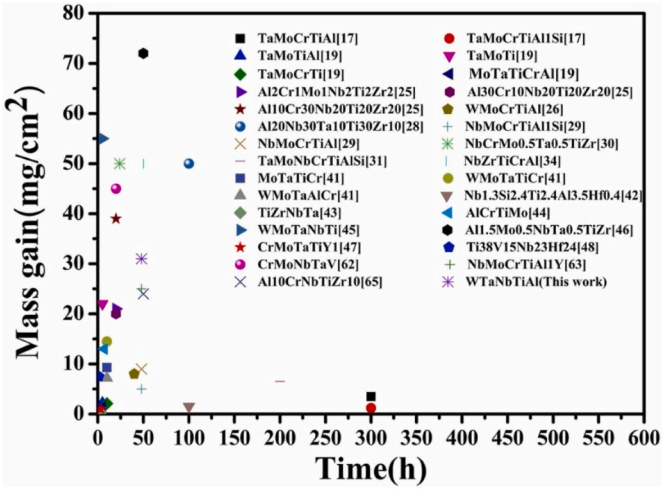


**Fig. 24.** Mass gain of different RHEAs reported in literature subjected to exposure in air at 1000 °C [203]. Reproduced with permission of Elsevier.

exposure to 400 μm after 48 h. TEM analyses were conducted on samples extracted from each of the oxide layers of the samples oxidized for 36 h. Hence, for the outer layer, it was observed the major presence of $AlNbO_4$, followed by Ti-rich oxides, and $Ta_{1.5}Nb_{1.5}O_3$; in the case of the internal oxidation front, only the $Ta_8W_9O_{47}$ and Ti-rich oxides were observed, with Al homogeneously distributed in this layer. Lastly, the inner side of the internal oxidation front presented multiple complex oxides, including W,Ta- and Al,Ti-rich oxides. Based on all their analyses, the authors concluded that the oxidation process can be modeled as diffusion-controlled growth of multilayer oxide scale, with the outer layer acting as the protective layer, meanwhile the internal layer acted as a path for the diffusion of Al, Ti, and Nb cations towards the surface.

## 7. Concluding remarks, challenges, and future directions

The goal of producing RHEAs employing MA + SPS with null contamination seems unachievable since many contamination sources can be found during the entire process, added to the high reactivity of refractory elements with O, C, and N. Certain strategies could be employed to control or minimize the contamination issue. For example, the utilization of hydrogen in the sintering atmosphere (commonly diluted in Ar) may contribute to reducing the oxygen content of the powder and with that, the formation of oxidized particles. This approach has not been applied in the preparation of RHEAs parts yet, and despite of the potential of the strategy, several issues must be considered too (such as safety and risks issues, as well as the formation of hydrides and its effect on the alloy's performance).

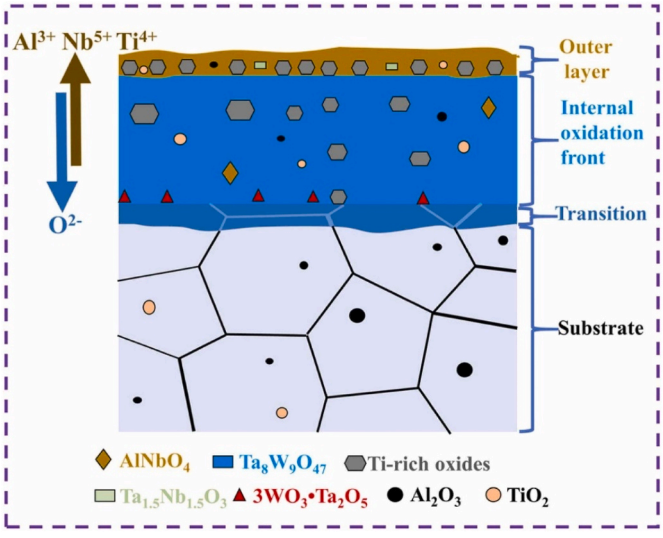


**Fig. 25.** Scheme of the 1000 °C oxidation process of the WTaNbTiAl RHEA prepared by MA + SPS [203]. Reproduced with permission of Elsevier.

It has been observed that prolonged milling times cause higher contents of contaminant elements; the first strategy could be optimize the milling time then, in order to mill for the shortest time that results in a sintered sample with the appropriate microstructure or performance. This, despite that the system has not entered yet in the steady-state stage or that the alloying was not fully accomplished in such short milling period. Of course, this strategy may be expensive since it requires extensive trial and error analysis, as well as the characterization of both powder and sintered samples for each iteration. However, experiences from previous authors have shown that despite of the heterogeneous composition of powders milled for short times, an homogeneous microstructure is obtained after SPS processing. Hence, the efforts may be focused on optimizing SPS conditions (mainly sintering temperature) for shortly milled powders at typical laboratory conditions, rather than explore the multiple variables of MA besides of those of the sintering stage.

Alternatively, powders can be alloyed in a sequenced manner: that is, certain elemental powders can be produced in a first stage (either by MA or atomization processes), and the resulting alloyed (or semi-alloyed) powder can then be milled with a more time-sensitive elemental powder to obtain the final alloy. This could be especially helpful when ductile powders (such as Ni, Fe, or Al) are considered in the composition of a RHEA (commonly constituted by brittle elemental powders, that are less prone to cold weld to the milling media and container) in order to reduce the dosage of the PCA, and with that, the contamination levels of C and O. In a similar line, the combination of dry and wet milling processes have resulted in successful cases in which the PCA dosage is controlled, at the same time that the powder yield is adequately elevated.

The PM route is an extremely versatile process, since MA gives the possibility to produce powders with different characteristics (particle size, dislocation density, homogeneity, contamination degree, etc) that can be blended and used for the consolidation stage. Hence, for example, mixing powders milled for different times (and therefore, with different dislocation density, crystallite size, and interstitial elements content) and subject them to sintering, may produce heterostructured RHEAs. These will exhibit at least two series of regions with different features, such as different grain size, different content, size, or distribution of precipitates, etc. Thus, these heterostructured RHEAs can present a superior combination of strength and ductility, which may be especially interesting to provide some ductility to those brittle alloys with extremely high yield strength. Up to the date of this work, a few heterostructured RHEAs have been reported with promising results, but there is no study producing heterostructured RHEAs employing powder metallurgy approaches yet.

In terms of mechanical properties, there is a considerable lack of studies reporting tensile test results of RHEAs prepared by MA + SPS, either at room as at high temperature, that may be considered as one of the most urgent aspects in the research of these alloys. There is an effervescent number of articles reporting tensile test mechanical properties in the field of RHEAs, but all of these were made on samples produced by either casting or additive manufacturing techniques. In this way, the difficulties in producing large parts (large enough to cut tensile specimens from them, for example) have limited the exploration of tensile properties of MA + SPS RHEAs, but certain alternatives, such as micro-tensile tests, can contribute to solve this issue.

As described, ultrafine grain sizes and finely dispersed precipitates are commonly observed in the microstructure of RHEAs produced by MA + SPS, which seems to be the characteristic features that provide them with the superior mechanical performance. While the first

considerably contributes to the room temperature strength, the contribution of fine precipitates may not be as relevant as expected. Additionally, their contribution to the strength through other mechanisms beyond Orowan strengthening have been scarcely considered. Still, their role in suppressing grain growth and providing elevated thermal stability may be fundamental for the superior performance of MA + SPS RHEAs. On the other hand, when interstitial elements remain dissolved in the lattice of the matrix phase they considerably enhance the mechanical performance. Instead of that, researchers may consider additional strategies to take advantage of oxide and carbide formation, controlling their fraction, size, and distribution, in order to enhance and optimize mechanical properties of PM RHEAs.

It has been showed that RHEAs exhibits uncommon behaviors under hot deformation, presenting DRX in conditions that bcc metals and their alloys commonly exhibit DRV. In traditional alloys the competition of DRX and DRV is determined by the SFE, but as briefly described in this work, HEAs do not exhibit a single SFE value, but a distribution of values based in the surrounding atoms in each position of the lattice. Hence, the role that SFE in the deformation and softening mechanisms of HEAs must be revisited yet. Additionally, the character of the controlling dislocations and their propagation mechanisms of bcc RHEAs is different than that of bcc metals too, recently attributed to the effect of SRO increasing the energy barrier for dislocation glide. Hence, the superior mechanical performance may be explained by other factors beyond the typically considered strengthening mechanisms. The exciting results obtained in these subjects are expected to promote further studies, in both computational and experimental fields, to fully understand the foundations behind the performance of not only RHEAs, but of HEAs in general.

Despite the outstanding performance in terms of high-temperature mechanical properties of PM RHEAs, very few studies have addressed their constitutive modelling, their microstructural evolution, and the texture evolution to have a better comprehension of their deformation and softening mechanisms. In order to enhance the high-temperature mechanical performance of these alloy, is fundamental to understand the principles behind them, and only after that, it will be possible to efficiently tailor the alloy composition and its microstructure in the adequate directions.

Unfortunately, the derivation of the constitutive equations demands a lot of compression samples since a large set of tests at different deformation conditions may be required to adequately explore the hot deformation of RHEAs. At the same time, to adequately approach the microstructural evolution of these alloys, an exhaustive characterization of the quenched samples deformed at different temperatures, strain rates, and strains is necessary, too.

On the other hand, a considerable lack of literature addressing the high-temperature oxidation resistance of PM RHEAs can be noticed. Most of the studies in this subject but done in as-cast RHEAs already establishes relationships between composition and performance, but the role of microstructure (especially those particular features of MA + SPS RHEAs, such as ultrafine-grained microstructure and the presence of oxide and carbides) has not been properly addressed yet. Hence, it would be interesting to study the oxidation behavior of those MA + SPS RHEAs that presented the best high-temperature mechanical properties, in order to advance into determining the guidelines for the alloy design and microstructural tunning of these subfamily of alloys.

One of the pending tasks of the HEAs field, in general, is the diffusional behavior of the constituent elements: contradictory results have been presented in the subject, reporting both sluggish and anti-sluggish tendencies. This issue is particularly relevant for high-temperature applications, since the activation energies of the diffusion of the species involved will determine the hot softening resistance of the alloy. Besides, in traditional alloys, it is pretty clear that the activation energies associated with the diffusion of the base element (either on its own bulk lattice or in the grain boundaries, depending on the mechanism) are those that will determine the softening resistance. In the case of single-phase HEAs though, with five species sharing the same lattice, there is no clarity yet of what species control the deformation (whether those with higher or lower diffusivity) or if the complex composition of the lattice plays an unexpected role too. In order to reveal that, more experimental and modelling studies are necessary to address the actual diffusional behavior of HEAs and their influence on the high-temperature mechanical performance.

## CRediT authorship contribution statement

**P. Martin:** Conceptualization, Investigation, Formal analysis, Visualization, Writing – original draft. **C. Aguilar:** Writing – review & editing. **J.M. Cabrera:** Writing – review & editing.

## Declaration of competing interest

The authors declare the following financial interests/personal relationships which may be considered as potential competing interests: Pablo Martin Saint-Laurence reports financial support was provided by National Agency for Research and Development. Claudio Aguilar reports financial support was provided by National Agency for Research and Development. Jose Maria Cabrera reports financial support was provided by State Agency of Research. If there are other authors, they declare that they have no known competing financial interests or personal relationships that could have appeared to influence the work reported in this paper.

## Acknowledgement

P. Martin gratefully acknowledges to ANID/Doctorado Becas Chile/2019–72200338. C. Aguilar acknowledges the Millennium Institute on Green Ammonia as Energy Vector—MIGA (ICN2021_023) supported by the Millennium Scientific Initiative, FONDECYT n° 1230620, FONDEQUIP n° EQM140095 and postdoctorate project n°74220021. J. M. Cabrera is also grateful to the funding of project RTI2018-097885-B-C31 by the Agencia Estatal de Investigación (AEI) of Spain.

## Appendix A. Supplementary data

Supplementary data to this article can be found online at https://doi.org/10.1016/j.jmrt.2024.03.205.

## References

[1] Yeh JW, Chen SK, Lin SJ, Gan JY, Chin TS, Shun TT, et al. Nanostructured high-entropy alloys with multiple principal elements: novel alloy design concepts and outcomes. Adv Eng Mater 2004;6:299–303+274. https://doi.org/10.1002/adem.200300567.

[2] Cantor B, Chang ITH, Knight P, Vincent AJB. Microstructural development in equiatomic multicomponent alloys. Mater Sci Eng 2004;375–377:213–8. https://doi.org/10.1016/j.msea.2003.10.257.

[3] Yeh JW, Chen YL, Lin SJ, Chen SK. High-entropy alloys - a new era of exploitation. Mater Sci Forum 2007;560:1–9. https://doi.org/10.4028/www.scientific.net/MSF.560.1.

[4] Miracle DB, Senkov ON. A critical review of high entropy alloys and related concepts. Acta Mater 2017;122:448–511. https://doi.org/10.1016/j.actamat.2016.08.081.

[5] Gorsse S, Couzinié JP, Miracle DB. From high-entropy alloys to complex concentrated alloys. C R Phys 2018;19:721–36. https://doi.org/10.1016/j.crhy.2018.09.004.

[6] Cantor B. Multicomponent high-entropy Cantor alloys. Prog Mater Sci 2020:100754. https://doi.org/10.1016/j.pmatsci.2020.100754.

[7] Li Z, Zhao S, Ritchie RO, Meyers MA. Mechanical properties of high-entropy alloys with emphasis on face-centered cubic alloys. Prog Mater Sci 2019;102:296–345. https://doi.org/10.1016/j.pmatsci.2018.12.003.

[8] Senkov ON, Wilks GB, Miracle DB, Chuang CP, Liaw PK. Refractory high-entropy alloys. Intermetallics (Barking) 2010;18:1758–65. https://doi.org/10.1016/j.intermet.2010.05.014.

[9] Senkov ON, Wilks GB, Scott JM, Miracle DB. Mechanical properties of Nb25Mo25Ta25W 25 and V20Nb20Mo20Ta20W20 refractory high entropy alloys. Intermetallics (Barking) 2011;19:698–706. https://doi.org/10.1016/j.intermet.2011.01.004.

[10] Senkov ON, Miracle DB, Rao SI. Correlations to improve room temperature ductility of refractory complex concentrated alloys. Mater Sci Eng, A 2021;820:141512. https://doi.org/10.1016/j.msea.2021.141512.
[11] Laube S, Chen H, Kauffmann A, Schellert S, Müller F, Gorr B, et al. Controlling crystallographic ordering in Mo–Cr–Ti–Al high entropy alloys to enhance ductility. J Alloys Compd 2020;823:153805. https://doi.org/10.1016/j.jallcom.2020.153805.
[12] Wang T, Jiang W, Wang X, Jiang B, Rong C, Wang Y, et al. Microstructure and properties of Al0.5NbTi3VxZr2 refractory high entropy alloys combined with high strength and ductility. J Mater Res Technol 2023;24:1733–43. https://doi.org/10.1016/j.jmrt.2023.03.103.
[13] Qiao DX, Jiang H, Jiao WN, Lu YP, Cao ZQ, Li TJ. A novel series of refractory high-entropy alloys Ti2ZrHf0.5VNbx with high specific yield strength and good ductility. Acta Metall Sin 2019;32:925–31. https://doi.org/10.1007/s40195-019-00921-3.
[14] Wang M, Ma ZL, Xu ZQ, Cheng XW. Effects of vanadium concentration on mechanical properties of VxNbMoTa refractory high-entropy alloys. Mater Sci Eng 2021;808. https://doi.org/10.1016/j.msea.2021.140848.
[15] Senkov ON, Woodward C, Miracle DB. Microstructure and properties of aluminum-containing refractory high-entropy alloys. Jom 2014;66:2030–42. https://doi.org/10.1007/s11837-014-1066-0.
[16] Juan CC, Tseng KK, Hsu WL, Tsai MH, Tsai CW, Lin CM, et al. Solution strengthening of ductile refractory HfMoxNbTaTiZr high-entropy alloys. Mater Lett 2016;175:284–7. https://doi.org/10.1016/j.matlet.2016.03.133.
[17] Wei W, Wang T, Wang C, Wu M, Nie Y, Peng J. Ductile W0.4MoNbxTaTi refractory high-entropy alloys with excellent elevated temperature strength. Mater Lett 2021;295. https://doi.org/10.1016/j.matlet.2021.129753.
[18] Iroc LK, Tukac OU, Tanrisevdi BB, El-Atwani O, Tunes MA, Kalay YE, et al. Design of oxygen-doped TiZrHfNbTa refractory high entropy alloys with enhanced strength and ductility. Mater Des 2022;223:111239. https://doi.org/10.1016/j.matdes.2022.111239.
[19] Zhao B, Chen G, Lv S, Fu X, Zhou W. Doping N/O impurities into a MoNbTiWZr refractory multi-principal element alloy and the strengthening mechanism. J Mater Eng Perform 2021;30:9359–69. https://doi.org/10.1007/s11665-021-06093-5.
[20] Xin SW, Shen X, Du CC, Zhao J, Sun BR, Xue HX, et al. Bulk nanocrystalline boron-doped VNbMoTaW high entropy alloys with ultrahigh strength, hardness, and resistivity. J Alloys Compd 2021;853. https://doi.org/10.1016/j.jallcom.2020.155995.
[21] Kang B, Kong T, Dan NH, Phuong DD, Ryu HJ, Hong SH. Effect of boron addition on the microstructure and mechanical properties of refractory Al0.1CrNbVMo high-entropy alloy. Int J Refract Metals Hard Mater 2021;100. https://doi.org/10.1016/j.ijrmhm.2021.105636.
[22] Wang R, Tang Y, Lei Z, Ai Y, Tong Z, Li S, et al. Achieving high strength and ductility in nitrogen-doped refractory high-entropy alloys. Mater Des 2022;213:110356. https://doi.org/10.1016/j.matdes.2021.110356.
[23] Sheikh S, Shafeie S, Hu Q, Ahlström J, Persson C, Veselý J, et al. Alloy design for intrinsically ductile refractory high-entropy alloys. J Appl Phys 2016;120. https://doi.org/10.1063/1.4966659.
[24] Senkov ON, Rao SI, Butler TM, Chaput KJ. Ductile Nb alloys with reduced density and cost. J Alloys Compd 2019;808:151685. https://doi.org/10.1016/j.jallcom.2019.151685.
[25] Gorr B, Schellert S, Müller F, Christ H-J, Kauffmann A, Heilmaier M. Current status of research on the oxidation behavior of refractory high entropy alloys. Adv Eng Mater 2021;23. https://doi.org/10.1002/adem.202001047.
[26] Xiang T, Zhao M, Du P, Xie G. Heat treatment effects on microstructure and mechanical properties of TiZrNbTa high-entropy alloy. J Alloys Compd 2023;930:167408. https://doi.org/10.1016/j.jallcom.2022.167408.
[27] Wang H, Chen W, Fu Z, Chu C, Tian Z, Jiang Z, et al. Lightweight Ti-Zr-Nb-Al-V refractory high-entropy alloys with superior strength-ductility synergy and corrosion resistance. Int J Refract Metals Hard Mater 2023;116:106331. https://doi.org/10.1016/j.ijrmhm.2023.106331.
[28] Senkov ON, Miracle DB, Chaput KJ, Couzinie JP. Development and exploration of refractory high entropy alloys - a review. J Mater Res 2018;33:3092–128. https://doi.org/10.1557/jmr.2018.153.
[29] Senkov ON, Scott JM, Senkova SV, Meisenkothen F, Miracle DB, Woodward CF. Microstructure and elevated temperature properties of a refractory TaNbHfZrTi alloy. J Mater Sci 2012;47:4062–74. https://doi.org/10.1007/s10853-012-6260-2.
[30] Senkov ON, Senkova SV, Miracle DB, Woodward C. Mechanical properties of low-density, refractory multi-principal element alloys of the Cr-Nb-Ti-V-Zr system. Mater Sci Eng 2013;565:51–62. https://doi.org/10.1016/j.msea.2012.12.018.
[31] Stepanov ND, Yurchenko NY, Zherebtsov SV, Tikhonovsky MA, Salishchev GA. Aging behavior of the HfNbTaTiZr high entropy alloy. Mater Lett 2018;211:87–90. https://doi.org/10.1016/j.matlet.2017.09.094.
[32] Yurchenko NY, Stepanov ND, Gridneva AO, Mishunin MV, Salishchev GA, Zherebtsov SV. Effect of Cr and Zr on phase stability of refractory Al-Cr-Nb-Ti-V-Zr high-entropy alloys. J Alloys Compd 2018;757:403–14. https://doi.org/10.1016/j.jallcom.2018.05.099.
[33] Senkov ON, Senkova SV, Dimiduk DM, Woodward C, Miracle DB. Oxidation behavior of a refractory NbCrMo 0.5Ta 0.5TiZr alloy. J Mater Sci 2012;47:6522–34. https://doi.org/10.1007/s10853-012-6582-0.
[34] Soni V, Gwalani B, Alam T, Dasari S, Zheng Y, Senkov ON, et al. Phase inversion in a two-phase, BCC+B2, refractory high entropy alloy. Acta Mater 2020;185:89–97. https://doi.org/10.1016/j.actamat.2019.12.004.
[35] Senkov ON, Isheim D, Seidman DN, Pilchak AL. Development of a refractory high entropy superalloy. Entropy 2016;18:1–13. https://doi.org/10.3390/e18030102.
[36] Wang Q, Han J, Liu Y, Zhang Z, Dong C, Liaw PK. Coherent precipitation and stability of cuboidal nanoparticles in body-centered-cubic Al0.4Nb0.5Ta0.5TiZr0.8 refractory high entropy alloy. Scripta Mater 2021;190:40–5. https://doi.org/10.1016/j.scriptamat.2020.08.029.
[37] Whitfield TE, Pickering EJ, Owen LR, Jones CN, Stone HJ, Jones NG. The effect of Al on the formation and stability of a BCC – B2 microstructure in a refractory metal high entropy superalloy system. Materialia (Oxf) 2020;13:100858. https://doi.org/10.1016/j.mtla.2020.100858.
[38] Peng H, Kang Z, Long Y, Zhou L. A two-phase ultrafine-grained NbMoTaWV refractory high entropy alloy with prominent compressive properties. Vacuum 2022;199:110930. https://doi.org/10.1016/j.vacuum.2022.110930.
[39] Kang B, Kong T, Ryu HJ, Hong SH. Superior mechanical properties and strengthening mechanisms of lightweight AlxCrNbVMo refractory high-entropy alloys (x = 0, 0.5, 1.0) fabricated by the powder metallurgy process. J Mater Sci Technol 2021;69:32–41. https://doi.org/10.1016/j.jmst.2020.07.012.
[40] Kang B, Lee J, Ryu HJ, Hong SH. Microstructure, mechanical property and Hall-Petch relationship of a light-weight refractory Al0.1CrNbVMo high entropy alloy fabricated by powder metallurgical process. J Alloys Compd 2018;767:1012–21. https://doi.org/10.1016/j.jallcom.2018.07.145.
[41] Kang B, Lee J, Ryu HJ, Hong SH. Ultra-high strength WNbMoTaV high-entropy alloys with fine grain structure fabricated by powder metallurgical process. Mater Sci Eng 2018;712:616–24. https://doi.org/10.1016/j.msea.2017.12.021.
[42] Waseem OA, Lee J, Lee HM, Ryu HJ. The effect of Ti on the sintering and mechanical properties of refractory high-entropy alloy TixWTaVCr fabricated via spark plasma sintering for fusion plasma-facing materials. Mater Chem Phys 2018;210:87–94. https://doi.org/10.1016/j.matchemphys.2017.06.054.
[43] Han J, Su B, Lu J, Meng J, Zhang A, Wu Y. Preparation of MoNbTaW refractory high entropy alloy powders by pressureless spark plasma sintering: crystal structure and phase evolution. Intermetallics (Barking) 2020;123. https://doi.org/10.1016/j.intermet.2020.106832.
[44] Zong L, Xu L, Luo C, Li Z, Zhao Y, Xu Z, et al. Fabrication of nano-ZrO2 strengthened WMoNbTaV refractory high-entropy alloy by spark plasma sintering. Mater Sci Eng, A 2022;843. https://doi.org/10.1016/j.msea.2022.143113.
[45] Liu J, Zhao X, Zhang S, Sheng Y, Hu Q. Microstructure and mechanical properties of MoNbTaW refractory high-entropy alloy prepared by spark plasma sintering. J Mater Res 2023;38:484–96. https://doi.org/10.1557/s43578-022-00833-6.
[46] Zhu C, Li Z, Hong C, Dai P, Chen J. Microstructure and mechanical properties of the TiZrNbMoTa refractory high-entropy alloy produced by mechanical alloying and spark plasma sintering. Int J Refract Metals Hard Mater 2020;93:105357. https://doi.org/10.1016/j.ijrmhm.2020.105357.
[47] Gao F, Sun Y, Hu L, Shen J, Liu W, Ba M, et al. Microstructure and strengthening mechanisms of novel lightweight TiAlV0.5CrMo refractory high-entropy alloy fabricated by mechanical alloying and spark plasma sintering. J Alloys Compd 2023;932:167659. https://doi.org/10.1016/j.jallcom.2022.167659.
[48] Suryanarayana C. Mechanical alloying and milling. New York: Marcel Dekker; 2004.
[49] Pan J, Dai T, Lu T, Ni X, Dai J, Li M. Microstructure and mechanical properties of Nb25Mo25Ta25W25 and Ti8Nb23Mo23Ta23W23 high entropy alloys prepared by mechanical alloying and spark plasma sintering. Mater Sci Eng 2018;738:362–6. https://doi.org/10.1016/j.msea.2018.09.089.
[50] Liu Q, Wang G, Sui X, Liu Y, Li X, Yang J. Microstructure and mechanical properties of ultra-fine grained MoNbTaTiV refractory high-entropy alloy fabricated by spark plasma sintering. J Mater Sci Technol 2019;35:2600–7. https://doi.org/10.1016/j.jmst.2019.07.013.
[51] Torralba JM, Alvaredo P, García-Junceda A. High-entropy alloys fabricated via powder metallurgy. A critical review. Powder Metall 2019;62:84–114. https://doi.org/10.1080/00325899.2019.1584454.
[52] Vaidya M, Muralikrishna GM, Murty BS. High-entropy alloys by mechanical alloying: a review. J Mater Res 2019;34:664–86. https://doi.org/10.1557/jmr.2019.37.
[53] Ke B, Sun Y, Zhang Y, Wang W, Wang W, Ma P, et al. Powder metallurgy of high-entropy alloys and related composites: a short review. Int J Miner Metall Mater 2021;28:931–43. https://doi.org/10.1007/s12613-020-2221-y.
[54] Tian Y, Zhou W, Tan Q, Wu M, Qiao S, Zhu G, et al. A review of refractory high-entropy alloys. Trans Nonferrous Metals Soc China 2022;32:3487–515. https://doi.org/10.1016/S1003-6326(22)66035-7.
[55] Moravcikova-Gouvea L, Moravcik I, Pouchly V, Kovacova Z, Kitzmantel M, Neubauer E, et al. Tailoring a refractory high entropy alloy by powder metallurgy process optimization. Materials 2021;14. https://doi.org/10.3390/ma14195796.
[56] Suryanarayana C. Mechanical alloying and milling. Prog Mater Sci 2001;46:1–184. https://doi.org/10.1016/S0079-6425(99)00010-9.
[57] German RM. Powder metallurgy and particulate materials processing. First. Princeton, New Jersey: Metal Powder Industries Federation; 2005.
[58] Burgio N, Iasonna A, Magini M, Martelli S, Padella F. Mechanical alloying of the Fe-Zr system. Correlation between input energy and end products. Il Nuovo Cimento D 1991;13:459–76. https://doi.org/10.1007/BF02452130.
[59] Hodaei A, Ataie A, Mostafavi E. Intermediate milling energy optimization to enhance the characteristics of barium hexaferrite magnetic nanoparticles. J Alloys Compd 2015;640:162–8. https://doi.org/10.1016/j.jallcom.2015.03.230.
[60] Ghayour H, Abdellahi M, Bahmanpour M. Optimization of the high energy ball-milling: modeling and parametric study. Powder Technol 2016;291:7–13. https://doi.org/10.1016/j.powtec.2015.12.004.

[61] Shkodich N, Sedegov A, Kuskov K, Busurin S, Scheck Y, Vadchenko S, et al. Refractory high-entropy HfTaTiNbZr-based alloys by combined use of ball milling and spark plasma sintering: effect of milling intensity. Metals (Basel) 2020;10:1–15. https://doi.org/10.3390/met10091268.

[62] Roh A, Kim D, Nam S, Kim DI, Kim HY, Lee KA, et al. NbMoTaW refractory high entropy alloy composites strengthened by in-situ metal-non-metal compounds. J Alloys Compd 2020;822:153423. https://doi.org/10.1016/j.jallcom.2019.153423.

[63] Zhan L, Hou J, Wang G, Chen Y, Luo S, Kang Q, et al. Study on mechanical alloying behavior and thermal stability of HfMoNbTaTi refractory high-entropy alloy. Mater Char 2023;203. https://doi.org/10.1016/j.matchar.2023.113122.

[64] Wang G, Liu Q, Yang J, Li X, Sui X, Gu Y, et al. Synthesis and thermal stability of a nanocrystalline MoNbTaTiV refractory high-entropy alloy via mechanical alloying. Int J Refract Metals Hard Mater 2019;84:104988. https://doi.org/10.1016/j.ijrmhm.2019.104988.

[65] Cambridge U of. Ellingham diagram n.d..

[66] Málek J, Zýka J, Lukáč F, Vilémová M, Vlasák T, Čížek J, et al. The effect of processing route on properties of HfNbTaTiZr high entropy alloy. Materials 2019;12:1–15. https://doi.org/10.3390/ma12234022.

[67] Fu A, Guo W, Liu B, Cao Y, Xu L, Fang Q, et al. A particle reinforced NbTaTiV refractory high entropy alloy based composite with attractive mechanical properties. J Alloys Compd 2020;815. https://doi.org/10.1016/j.jallcom.2019.152466.

[68] Long Y, Su K, Zhang J, Liang X, Peng H, Li X. Enhanced strength of a mechanical alloyed NbMoTaWVTi refractory high entropy alloy. Materials 2018;11:1–8. https://doi.org/10.3390/ma11050669.

[69] Long Y, Liang X, Su K, Peng H, Li X. A fine-grained NbMoTaWVCr refractory high-entropy alloy with ultra-high strength: microstructural evolution and mechanical properties. J Alloys Compd 2019;780:607–17. https://doi.org/10.1016/j.jallcom.2018.11.318.

[70] Yan J, Li K, Wang Y, Qiu J. Microstructure and mechanical properties of WMoNbCrTi HEAs sintered from the powders milled for different durations. Jom 2019;71:2489–97. https://doi.org/10.1007/s11837-019-03432-9.

[71] Xin SW, Zhang M, Yang TT, Zhao YY, Sun BR, Shen TD. Ultrahard bulk nanocrystalline VNbMoTaW high-entropy alloy. J Alloys Compd 2018;769:597–604. https://doi.org/10.1016/j.jallcom.2018.07.331.

[72] Guo W, Liu B, Liu Y, Li T, Fu A, Fang Q, et al. Microstructures and mechanical properties of ductile NbTaTiV refractory high entropy alloy prepared by powder metallurgy. J Alloys Compd 2019;776:428–36. https://doi.org/10.1016/j.jallcom.2018.10.230.

[73] Lukáč F, Vilémová M, Klementová M, Minárik P, Chráska T. The origin and the effect of the fcc phase in sintered HfNbTaTiZr. Mater Lett 2021;286. https://doi.org/10.1016/j.matlet.2020.129224.

[74] Menapace C, Shaik KNR, Emanuelli L, Ischia G. Production of a reinforced refractory multielement alloy via high-energy ball milling and spark plasma sintering. Metals (Basel) 2023;13:1189. https://doi.org/10.3390/met13071189.

[75] Raman L, Karthick G, Guruvidyathri K, Fabijanic D, Narayana Murty SVS, Murty BS, et al. Influence of processing route on the alloying behavior, microstructural evolution and thermal stability of CrMoNbTiW refractory high-entropy alloy. J Mater Res 2020;35:1556–71. https://doi.org/10.1557/jmr.2020.128.

[76] Boztemur B, Bayrak KG, Gökçe H, Ayas E, Balcı-Çağıran Ö, Derin B, et al. Mechanically alloyed and spark plasma sintered WNbMoVTa refractory high entropy alloys: effects of Cr and Al on the microstructural and mechanical properties. J Alloys Compd 2023;965. https://doi.org/10.1016/j.jallcom.2023.171415.

[77] Kalali DG, Antharam S, Hasan M, Karthik PS, Phani PS, Bhanu Sankara Rao K, et al. On the origins of ultra-high hardness and strain gradient plasticity in multi-phase nanocrystalline MoNbTaTiW based refractory high-entropy alloy. Mater Sci Eng, A 2021;812. https://doi.org/10.1016/j.msea.2021.141098.

[78] Raman L, Guruvidyathri K, Kumari G, Narayana Murty SVS, Kottada RS, Murty BS. Phase evolution of refractory high-entropy alloy CrMoNbTiW during mechanical alloying and spark plasma sintering. J Mater Res 2019;34:756–66. https://doi.org/10.1557/jmr.2018.483.

[79] Prakash O, Chandrakar R, Chandraker S, Rao KR, Kumar R, Kumar A, et al. Phase evolution of novel MoNbSiTiW refractory high-entropy alloy prepared by mechanical alloying. JOM 2022;74:3329–33. https://doi.org/10.1007/s11837-022-05417-7.

[80] Kang B, Kong T, Raza A, Ryu HJ, Hong SH. Fabrication, microstructure and mechanical property of a novel Nb-rich refractory high-entropy alloy strengthened by in-situ formation of dispersoids. Int J Refract Metals Hard Mater 2019;81:15–20. https://doi.org/10.1016/j.ijrmhm.2019.02.009.

[81] Qin M, Shivakumar S, Luo J. Refractory high-entropy nanoalloys with exceptional high-temperature stability and enhanced sinterability. J Mater Sci 2023;58:8548–62. https://doi.org/10.1007/s10853-023-08535-y.

[82] Qiao Y, Tang Y, Li S, Ye Y, Liu X, Zhu L, et al. Preparation of TiZrNbTa refractory high-entropy alloy powder by mechanical alloying with liquid process control agents. Intermetallics (Barking) 2020;126:106900. https://doi.org/10.1016/j.intermet.2020.106900.

[83] Smeltzer JA, Marvel CJ, Hornbuckle BC, Roberts AJ, Marsico JM, Giri AK, et al. Achieving ultra hard refractory multi-principal element alloys via mechanical alloying. Mater Sci Eng, A 2019;763:138140. https://doi.org/10.1016/j.msea.2019.138140.

[84] Liu Q, Wang G, Liu Y, Sui X, Chen Y, Luo S. Hot deformation behaviors of an ultrafine-grained MoNbTaTiV refractory high-entropy alloy fabricated by powder metallurgy. Mater Sci Eng 2021;809:140922. https://doi.org/10.1016/j.msea.2021.140922.

[85] Liu Q, Wang G, Sui X, Xu Y, Liu Y, Yang J. Ultra-fine grain TixVNbMoTa refractory high-entropy alloys with superior mechanical properties fabricated by powder metallurgy. J Alloys Compd 2021;865:158592. https://doi.org/10.1016/j.jallcom.2020.158592.

[86] Xiang T, Cai Z, Du P, Li K, Zhang Z, Xie G. Dual phase equal-atomic NbTaTiZr high-entropy alloy with ultra-fine grain and excellent mechanical properties fabricated by spark plasma sintering. J Mater Sci Technol 2021;90:150–8. https://doi.org/10.1016/j.jmst.2021.03.024.

[87] Das S, Robi PS. A novel refractory WMoVCrTa high-entropy alloy possessing fine combination of compressive stress-strain and high hardness properties. Adv Powder Technol 2020;31:4619–31. https://doi.org/10.1016/j.apt.2020.10.008.

[88] Das S, Robi PS. Processing and characterization of W23Mo23V17Cr8Ta7Fe22 and WMoVCrTa refractory high entropy alloys. Int J Refract Metals Hard Mater 2021;100. https://doi.org/10.1016/j.ijrmhm.2021.105656.

[89] Lv S, Zu Y, Chen G, Zhao B, Fu X, Zhou W. A multiple nonmetallic atoms co-doped CrMoNbWTi refractory high-entropy alloy with ultra-high strength and hardness. Mater Sci Eng, A 2020;795. https://doi.org/10.1016/j.msea.2020.140035.

[90] Ditenberg IA, Smirnov IV, Grinyaev KV, Osipov DA, Gavrilov AI, Korchagin MA. Morphology, structural-phase state and microhardness of a multicomponent non-equiatomic W-Ta-Mo-Nb-Zr-Cr-Ti powders mixture depending on the duration of ball milling. Adv Powder Technol 2020;31:4401–10. https://doi.org/10.1016/j.apt.2020.09.016.

[91] Zhi Q, Tan X, Liu Z, Liu Y, Zhang Q, Chen Y, et al. Effect of Zr content on microstructure and mechanical properties of lightweight Al2NbTi3V2Zrx high entropy alloy. Micron 2021;144:103031. https://doi.org/10.1016/j.micron.2021.103031.

[92] Ditenberg IA, Smirnov IV, Korchagin MA, Grinyaev KV, Melnikov VV, Pinzhin YP, et al. Structure and phase composition of a W-Ta-Mo-Nb-V-Cr-Zr-Ti alloy obtained by ball milling and spark plasma sintering. Entropy 2020;22. https://doi.org/10.3390/e22020143.

[93] Suryanarayana C. Mechanical alloying and milling. Prog Mater Sci 2001;46:1–184. https://doi.org/10.1016/S0079-6425(99)00010-9.

[94] Reverte E, Keller C, Calvo-Dahlborg M, Alcalá G, Campos M, Cornide J. Effect of Y2O3 addition on the microstructure and mechanical properties of an Al1.8CoCrCu0.5FeNi BCC HEA. J Alloys Compd 2023;960:170647. https://doi.org/10.1016/j.jallcom.2023.170647.

[95] Datta T, Manna I, Majumdar JD. Synthesis of equiatomic CoCrFeMnTiNi multicomponent alloy by sequential alloying using mechanical alloying and vacuum arc melting. J Mater Eng Perform 2024. https://doi.org/10.1007/s11665-024-09193-0.

[96] Devi Sushma U, Devikar A, Chandramouli G, Vinod Kumar GS, Singh S. Effect of pre-milling (Ni and Al) on the sintering behavior of NiAlFeCoCr high entropy alloy. Adv Powder Technol 2024;35:104378. https://doi.org/10.1016/j.apt.2024.104378.

[97] Vaidya M, Prasad A, Parakh A, Murty BS. Influence of sequence of elemental addition on phase evolution in nanocrystalline AlCoCrFeNi: novel approach to alloy synthesis using mechanical alloying. Mater Des 2017;126:37–46. https://doi.org/10.1016/j.matdes.2017.04.027.

[98] Şimşek T, Akgül Ş, Güler Ö, Özkul İ, Avar B, Chattopadhyay AK, et al. A comparison of magnetic, structural and thermal properties of NiFeCoMo high entropy alloy produced by sequential mechanical alloying versus the alloy produced by conventional mechanical alloying. Mater Today Commun 2021;29:102986. https://doi.org/10.1016/j.mtcomm.2021.102986.

[99] Shkodich NF, Kuskov KV, Sedegov AS, Kovalev ID, Panteleeva AV, Vergunova YS, et al. Refractory TaTiNb, TaTiNbZr, and TaTiNbZrX (X = Mo, W) high entropy alloys by combined use of high energy ball milling and spark plasma sintering: structural characterization, mechanical properties, electrical resistivity, and thermal conductivity. J Alloys Compd 2022;893:162030. https://doi.org/10.1016/j.jallcom.2021.162030.

[100] Chen CL, Chang CA, Chen HH. Investigation of Cr content, second phase, and sintering temperature on characteristics of WMoVTiCr refractory high entropy alloys. Int J Refract Metals Hard Mater 2023;110. https://doi.org/10.1016/j.ijrmhm.2022.106034.

[101] Gu T, Wang LM, Hu Q, Liang XB, Fu DX, Chen YX, et al. Effect of mechanical alloying and sintering behavior on the microstructure and properties of NbMoTaWRe refractory high entropy alloy. Met Mater Int 2022;28:2571–82. https://doi.org/10.1007/s12540-021-01165-6.

[102] He J, Qiao Y, Wang R, Tang Y, Li S, Liu X, et al. State and effect of oxygen on high entropy alloys prepared by powder metallurgy. J Alloys Compd 2022;891:161963. https://doi.org/10.1016/j.jallcom.2021.161963.

[103] Zong L, Xu L, Luo C, Jiao Z, Li X, Sun W, et al. Mechanical properties and strengthening mechanism of the nano-sized m-ZrO2 ceramic particle reinforced NbMoTaW refractory high-entropy alloy. Int J Refract Metals Hard Mater 2023;113. https://doi.org/10.1016/j.ijrmhm.2023.106201.

[104] Das S, Robi PS. Mechanical alloying of W-Mo-V-Cr-Ta high entropy alloys. IOP Conf Ser Mater Sci Eng 2018;346:012047. https://doi.org/10.1088/1757-899X/346/1/012047.

[105] Smeltzer JA, Burton MT, Hornbuckle BC, Giri AK, Darling KA, Harmer MP, et al. Optimization of cryogenic mechanical alloying parameters to synthesize ultrahard refractory high entropy materials. Mater Des 2021;210. https://doi.org/10.1016/j.matdes.2021.110070.

[106] Cavaliere P. Spark plasma sintering of materials: advances in processing and applications. https://doi.org/10.1007/978-3-030-05327-7; 2019.

[107] Sokkalingam R, Tarraste M, Surreddi KB, Mikli V, Muthupandi V, Sivaprasad K, et al. Powder metallurgy of Al 0.1 CoCrFeNi high-entropy alloy. J Mater Res 2020;35:2835–47. https://doi.org/10.1557/jmr.2020.272.
[108] Cao Y, Liu Y, Li Y, Liu B, Fu A, Nie Y. Precipitation behavior and mechanical properties of a hot-worked TiNbTa0.5ZrAl0.5 refractory high entropy alloy. Int J Refract Metals Hard Mater 2020;86. https://doi.org/10.1016/j.ijrmhm.2019.105132.
[109] Málek J, Zýka J, Lukáč F, Čížek J, Kunčická L, Kocich R. Microstructure and mechanical properties of sintered and heat-treated hfnbtatizr high entropy alloy. Metals (Basel) 2019;9:11–4. https://doi.org/10.3390/met9121324.
[110] Liu B, Wang J, Chen J, Fang Q, Liu Y. Ultra-high strength TiC/refractory high-entropy-alloy composite prepared by powder metallurgy. Jom 2017;69:651–6. https://doi.org/10.1007/s11837-017-2267-0.
[111] Xiang L, Guo W, Liu B, Fu A, Li J, Fang Q, et al. Microstructure and mechanical properties of TaNbVTiAlx refractory high-entropy alloys. Entropy 2020;22:282. https://doi.org/10.3390/e22030282.
[112] Zhang R, Meng J, Han J, Tulugan K, Zhang R. Oxidation resistance properties of refractory high-entropy alloys with varied AlxCrTiMo content. J Mater Sci 2021;56:3551–61. https://doi.org/10.1007/s10853-020-05480-y.
[113] Fu A, Cao Y, Liu Y, Xu S. Microstructure and mechanical properties of novel lightweight TaNbVTi-based refractory high entropy alloys. Materials 2022;15:355. https://doi.org/10.3390/ma15010355.
[114] Lukac F, Dudr M, Musalek R, Klecka J, Cinert J, Cizek J, et al. Spark plasma sintering of gas atomized high-entropy alloy HfNbTaTiZr. J Mater Res 2018;33:3247–57. https://doi.org/10.1557/jmr.2018.320.
[115] Akmal M, Park HK, Ryu HJ. Plasma spheroidized MoNbTaTiZr high entropy alloy showing improved plasticity. Mater Chem Phys 2021;273:125060. https://doi.org/10.1016/j.matchemphys.2021.125060.
[116] Tsai MH, Tsai RC, Chang T, Huang WF. Intermetallic phases in high-entropy alloys: statistical analysis of their prevalence and structural inheritance. Metals (Basel) 2019;9:1–18. https://doi.org/10.3390/met9020247.
[117] Li T, Liu B, Liu Y, Guo W, Fu A, Li L, et al. Microstructure and mechanical properties of particulate reinforced NbMoCrTiAl high entropy based composite. Entropy 2018;20. https://doi.org/10.3390/e20070517.
[118] Waseem OA, Ryu HJ. Powder metallurgy processing of a wx TaTiVCr high-entropy alloy and its derivative alloys for fusion material applications. Sci Rep 2017;7:1–14. https://doi.org/10.1038/s41598-017-02168-3.
[119] Jensen JK, Welk BA, Williams REA, Sosa JM, Huber DE, Senkov ON, et al. Characterization of the microstructure of the compositionally complex alloy Al1Mo0.5Nb1Ta0.5Ti1Zr1. Scripta Mater 2016;121:1–4. https://doi.org/10.1016/j.scriptamat.2016.04.017.
[120] Miracle DB, Tsai MH, Senkov ON, Soni V, Banerjee R. Refractory high entropy superalloys (RSAs). Scripta Mater 2020;187:445–52. https://doi.org/10.1016/j.scriptamat.2020.06.048.
[121] Stepanov ND, Yurchenko NY, Gridneva AO, Zherebtsov SV, Ivanisenko YV, Salishchev GA. Structure and hardness of B2 ordered refractory AlNbTiVZr0.5 high entropy alloy after high-pressure torsion. Mater Sci Eng 2018;716:308–15. https://doi.org/10.1016/j.msea.2018.01.061.
[122] Lu S, Li X, Liang X, Shao W, Yang W, Chen J. Effect of Al content on the oxidation behavior of refractory high-entropy alloy AlMo0.5NbTa0.5TiZr at elevated temperatures. Int J Refract Metals Hard Mater 2022;105:105812. https://doi.org/10.1016/j.ijrmhm.2022.105812.
[123] Mackie AJ, Hatton GD, Hamilton HGC, Dean JS, Goodall R. Carbon uptake and distribution in Spark Plasma Sintering (SPS) processed Sm(Co, Fe, Cu, Zr) z. Mater Lett 2016;171:14–7. https://doi.org/10.1016/j.matlet.2016.02.049.
[124] Moravcik I, Kubicek A, Moravcikova-Gouvea L, Adam O, Kana V, Pouchly V, et al. The origins of high-entropy alloy contamination induced by mechanical alloying and sintering. Metals (Basel) 2020;10:1186. https://doi.org/10.3390/met10091186.
[125] Laurent-Brocq M, Goujon P-A, Monnier J, Villeroy B, Perrière L, Pirès R, et al. Microstructure and mechanical properties of a CoCrFeMnNi high entropy alloy processed by milling and spark plasma sintering. J Alloys Compd 2019;780:856–65. https://doi.org/10.1016/j.jallcom.2018.11.181.
[126] Smetanina KE, Andreev PV, Nokhrin AV, Lantsev EA, Chuvildeev VN. Carbon contamination during spark plasma sintering of powder materials: a brief overview. J Alloys Compd 2024;973:172823. https://doi.org/10.1016/j.jallcom.2023.172823.
[127] Zhang L, Li X, Qu X, Qin M, Que Z, Wei Z, et al. Powder metallurgy route to ultrafine-grained refractory metals. Adv Mater 2023:2205807. https://doi.org/10.1002/adma.202205807. 1–25.
[128] Razumov N, Makhmutov T, Kim A, Shemyakinsky B, Shakhmatov A, Popovich V, et al. Refractory crmonbwv high-entropy alloy manufactured by mechanical alloying and spark plasma sintering: evolution of microstructure and properties. Materials 2021;14:1–14. https://doi.org/10.3390/ma14030621.
[129] Li X, Fu A, Cao Y, Xu S, Gao S. High-temperature mechanical properties and deformation behavior of carbides reinforced TiNbTaZrHf composite. J Alloys Compd 2022;894. https://doi.org/10.1016/j.jallcom.2021.162414.
[130] Zhu M, Yao L, Liu Y, Zhang M, Li K, Jian Z. Microstructure evolution and mechanical properties of a novel CrNbTiZrAlx ($0.25 \leq x \leq 1.25$) eutectic refractory high-entropy alloy. Mater Lett 2020;272:127869. https://doi.org/10.1016/j.matlet.2020.127869.
[131] Senkov ON, Jensen JK, Pilchak AL, Miracle DB, Fraser HL. Compositional variation effects on the microstructure and properties of a refractory high-entropy superalloy AlMo0.5NbTa0.5TiZr. Mater Des 2018;139:498–511. https://doi.org/10.1016/j.matdes.2017.11.033.
[132] Maiti S, Steurer W. Structural-disorder and its effect on mechanical properties in single-phase TaNbHfZr high-entropy alloy. Acta Mater 2016;106:87–97. https://doi.org/10.1016/j.actamat.2016.01.018.
[133] Xiang C, Fu HM, Zhang ZM, Han EH, Zhang HF, Wang JQ, et al. Effect of Cr content on microstructure and properties of Mo0.5VNbTiCrx high-entropy alloys. J Alloys Compd 2020;818. https://doi.org/10.1016/j.jallcom.2019.153352.
[134] Wang B, Wang Q, Lu N, Liang X, Shen B. Enhanced high-temperature strength of HfNbTaTiZrV refractory high-entropy alloy via Al2O3 reinforcement. J Mater Sci Technol 2022;123:191–200. https://doi.org/10.1016/j.jmst.2022.01.025.
[135] Yao HW, Qiao JW, Hawk JA, Zhou HF, Chen MW, Gao MC. Mechanical properties of refractory high-entropy alloys: experiments and modeling. J Alloys Compd 2017;696:1139–50. https://doi.org/10.1016/j.jallcom.2016.11.188.
[136] Yao HW, Qiao JW, Gao MC, Hawk JA, Ma SG, Zhou HF, et al. NbTaV-(Ti,W) refractory high-entropy alloys: experiments and modeling. Mater Sci Eng 2016;674:203–11. https://doi.org/10.1016/j.msea.2016.07.102.
[137] Coury FG, Kaufman M, Clarke AJ. Solid-solution strengthening in refractory high entropy alloys. Acta Mater 2019;175:66–81. https://doi.org/10.1016/j.actamat.2019.06.006.
[138] Chen B, Zhuo L. Latest progress on refractory high entropy alloys: composition, fabrication, post processing, performance, simulation and prospect. Int J Refract Metals Hard Mater 2023;110:105993. https://doi.org/10.1016/j.ijrmhm.2022.105993.
[139] Hall EO. The deformation and ageing of mild steel: III discussion of results. Proc Phys Soc B 1951;64:747–53. https://doi.org/10.1088/0370-1301/64/9/303.
[140] Kamikawa N, Sato K, Miyamoto G, Murayama M, Sekido N, Tsuzaki K, et al. Stress–strain behavior of ferrite and bainite with nano-precipitation in low carbon steels. Acta Mater 2015;83:383–96. https://doi.org/10.1016/j.actamat.2014.10.010.
[141] Williamson GK, Hall WH. X-ray line broadening from filed aluminium and wolfram. Acta Metall 1953;1:22–31. https://doi.org/10.1016/0001-6160(53)90006-6.
[142] Ungár T, Borbély A. The effect of dislocation contrast on x-ray line broadening: a new approach to line profile analysis. Appl Phys Lett 1996;69:3173–5. https://doi.org/10.1063/1.117951.
[143] Yang C, Bian H, Aoyagi K, Hayasaka Y, Yamanaka K, Chiba A. Synergetic strengthening in HfMoNbTaTi refractory high-entropy alloy via disordered nanoscale phase and semicoherent refractory particle. Mater Des 2021;212:110248. https://doi.org/10.1016/j.matdes.2021.110248.
[144] Song G, Sun Z, Li L, Clausen B, Zhang SY, Gao Y, et al. High temperature deformation mechanism in hierarchical and single precipitate strengthened ferritic alloys by in situ neutron diffraction studies. Sci Rep 2017;7:45965. https://doi.org/10.1038/srep45965.
[145] Liao T, Cao YK, Guo WM, Fang QH, Li J, Liu B. Microstructure and mechanical property of NbTaTiV refractory high-entropy alloy with different Y2O3 contents. Rare Met 2022. https://doi.org/10.1007/s12598-022-02038-6.
[146] Lu WJ, Zhang D, Zhang XN, Wu RJ, Sakata T, Mori H. Microstructure and tensile properties of in situ (TiB+TiC)/Ti6242 (TiB:TiC=1:1) composites prepared by common casting technique. Mater Sci Eng, A 2001;311:142–50. https://doi.org/10.1016/S0921-5093(01)00910-8.
[147] Nardone VC, Prewo KM. On the strength of discontinuous silicon carbide reinforced aluminum composites. Scripta Metall 1986;20:43–8. https://doi.org/10.1016/0036-9748(86)90210-3.
[148] Sun S, Zhao E, Hu C, An Y, Chen W. Precipitation behavior of silicide and synergetic strengthening mechanisms in TiB-reinforced high-temperature titanium matrix composites during multi-directional forging. J Alloys Compd 2021;867:159051. https://doi.org/10.1016/j.jallcom.2021.159051.
[149] Huang K, Logé RE. A review of dynamic recrystallization phenomena in metallic materials. Mater Des 2016;111:548–74. https://doi.org/10.1016/j.matdes.2016.09.012.
[150] Humphreys FJ, Rohrer GS, Rollett A. Recrystallization and related annealing phenomena. third ed. 2017.
[151] Kim S-I, Yoo Y-C. Dynamic recrystallization behavior of AISI 304 stainless steel. Mater Sci Eng, A 2001;311:108–13. https://doi.org/10.1016/S0921-5093(01)00917-0.
[152] Stepanov ND, Shaysultanov DG, Nyu Yurchenko, Zherebtsov SV, Ladygin AN, Salishchev GA, et al. High temperature deformation behavior and dynamic recrystallization in CoCrFeNiMn high entropy alloy. Mater Sci Eng, A 2015;636:188–95. https://doi.org/10.1016/j.msea.2015.03.097.
[153] Annasamy M, Haghdadi N, Taylor A, Hodgson P, Fabijanic D. Dynamic recrystallization behaviour of AlxCoCrFeNi high entropy alloys during high-temperature plane strain compression. Mater Sci Eng, A 2019;745:90–106. https://doi.org/10.1016/j.msea.2018.12.102.
[154] Primig S, Leitner H, Knabl W, Lorich A, Clemens H, Stickler R. Textural evolution during dynamic recovery and static recrystallization of molybdenum. Metall Mater Trans 2012;43:4794–805. https://doi.org/10.1007/s11661-012-1291-5.
[155] Li L, Wu H, Guo C, Feng Y. Deformation behavior and softening mechanism in ferrite steel during warm deformation. J Mater Res Technol 2022;18:3977–90. https://doi.org/10.1016/j.jmrt.2022.04.067.
[156] Sun Z-C, Zheng L-S, Yang H. Softening mechanism and microstructure evolution of as-extruded 7075 aluminum alloy during hot deformation. Mater Char 2014;90:71–80. https://doi.org/10.1016/j.matchar.2014.01.019.
[157] Guo NN, Wang L, Luo LS, Li XZ, Chen RR, Su YQ, et al. Hot deformation characteristics and dynamic recrystallization of the MoNbHfZrTi refractory high-entropy alloy. Mater Sci Eng 2016;651:698–707. https://doi.org/10.1016/j.msea.2015.10.113.

[158] Abubaker Khan M, Wang TL, Feng C, Sun H, Wang B, Hamza M, et al. A superb mechanical behavior of newly developed lightweight and ductile Al0.5Ti2Nb1Zr1Wx refractory high entropy alloy via nano-precipitates and dislocations induced-deformation. Mater Des 2022;222:111034. https://doi.org/10.1016/j.matdes.2022.111034.
[159] Cao T, Guo W, Lu W, Xue Y, Lu W, Su J, et al. Strain rate dependent deformation behavior of BCC-structured Ti29Zr24Nb23Hf24 high entropy alloy at elevated temperatures. J Alloys Compd 2022;891:161859. https://doi.org/10.1016/j.jallcom.2021.161859.
[160] Li-Yan L, Shu-nan C, Yi L, Gang J, Hai-Dong C, Yun-Jie J, et al. Microstructure and mechanical properties of lightweight AlxCrNbTiV(x = 0.2, 0.5, 0.8) refractory high entropy alloys. Int J Refract Metals Hard Mater 2022;102:105723.
[161] Wang B, Shan X, Zhao H, Bai S, Wang B, Tian Y. High-temperature deformation behavior and microstructural evolution of NbZrTiTa refractory high entropy alloy. J Alloys Compd 2023;936:168059. https://doi.org/10.2139/ssrn.4198973.
[162] Eleti RR, Chokshi AH, Shibata A, Tsuji N. Unique high-temperature deformation dominated by grain boundary sliding in heterogeneous necklace structure formed by dynamic recrystallization in HfNbTaTiZr BCC refractory high entropy alloy. Acta Mater 2020;183:64–77. https://doi.org/10.1016/j.actamat.2019.11.001.
[163] Eleti RR, Bhattacharjee T, Shibata A, Tsuji N. Unique deformation behavior and microstructure evolution in high temperature processing of HfNbTaTiZr refractory high entropy alloy. Acta Mater 2019;171:132–45. https://doi.org/10.1016/j.actamat.2019.04.018.
[164] Zhao B, Chen G, Lin Q, Wang K, Lv S, Fu X, et al. Thermal deformation characteristics of AlMo0.8NbTiW0.2Zr refractory multi-principal element alloy. Intermetallics (Barking) 2022;144:107524. https://doi.org/10.1016/j.intermet.2022.107524.
[165] Maresca F, Curtin WA. Mechanistic origin of high strength in refractory BCC high entropy alloys up to 1900K. Acta Mater 2020;182:235–49. https://doi.org/10.1016/j.actamat.2019.10.015.
[166] Lee C, Maresca F, Feng R, Chou Y, Ungar T, Widom M, et al. Strength can be controlled by edge dislocations in refractory high-entropy alloys. Nat Commun 2021;12:5474. https://doi.org/10.1038/s41467-021-25807-w.
[167] Baruffi C, Maresca F, Curtin WA. Screw vs. edge dislocation strengthening in body-centered-cubic high entropy alloys and implications for guided alloy design. MRS Commun 2022;12:1111–8. https://doi.org/10.1557/s43579-022-00278-2.
[168] Kubilay RE, Ghafarollahi A, Maresca F, Curtin WA. High energy barriers for edge dislocation motion in body-centered cubic high entropy alloys. npj Comput Mater 2021;7:112. https://doi.org/10.1038/s41524-021-00577-7.
[169] Lee C, Kim G, Chou Y, Musicó BL, Gao MC, An K, et al. Temperature dependence of elastic and plastic deformation behavior of a refractory high-entropy alloy. Sci Adv 2020;6. https://doi.org/10.1126/sciadv.aaz4748.
[170] Chen S, Aitken ZH, Pattamatta S, Wu Z, Yu ZG, Srolovitz DJ, et al. Short-range ordering alters the dislocation nucleation and propagation in refractory high-entropy alloys. Mater Today 2023;65:14–25. https://doi.org/10.1016/j.mattod.2023.03.009.
[171] Santos-Florez PA, Dai S-C, Yao Y, Yanxon H, Li L, Wang Y-J, et al. Short-range order and its impacts on the BCC MoNbTaW multi-principal element alloy by the machine-learning potential. Acta Mater 2023;255:119041. https://doi.org/10.1016/j.actamat.2023.119041.
[172] Guo S, Wang M, Sui S, Li J, Chen H, Hao X, et al. Research on optimizing strength and ductility of HfNbTaZr dual-phase high-entropy alloy by tuning chemical short-range order. Int J Refract Metals Hard Mater 2022;108:105942. https://doi.org/10.1016/j.ijrmhm.2022.105942.
[173] Liu X, Curtin WA. Atomistic simulations reveal strength reductions due to short-range order in alloys. Acta Mater 2024;263:119471. https://doi.org/10.1016/j.actamat.2023.119471.
[174] LaRosa CR, Ghazisaeidi M. A "local" stacking fault energy model for concentrated alloys. Acta Mater 2022;238:118165. https://doi.org/10.1016/j.actamat.2022.118165.
[175] Shih M, Miao J, Mills M, Ghazisaeidi M. Stacking fault energy in concentrated alloys. Nat Commun 2021;12:3590. https://doi.org/10.1038/s41467-021-23860-z.
[176] Liu X, Zhu Y, Wang C, Han K, Zhao L, Liang S, et al. A statistics-based study and machine-learning of stacking fault energies in HEAs. J Alloys Compd 2023;966:171547. https://doi.org/10.1016/j.jallcom.2023.171547.
[177] Sun H, Ding Z, Sun H, Zhou J, Ren J-C, Hu Q, et al. An efficient scheme for accelerating the calculation of stacking fault energy in multi-principal element alloys. J Mater Sci Technol 2024;175:204–11. https://doi.org/10.1016/j.jmst.2023.07.050.
[178] Savaedi Z, Motallebi R, Mirzadeh H. A review of hot deformation behavior and constitutive models to predict flow stress of high-entropy alloys. J Alloys Compd 2022;903:163964. https://doi.org/10.1016/j.jallcom.2022.163964.
[179] Sellars CM, McTegart WJ. On the mechanism of hot deformation. Acta Metall 1966;14:1136–8. https://doi.org/10.1016/0001-6160(66)90207-0.
[180] Jonas JJ, Sellars CM, Tegart WJMcG. Strength and structure under hot-working conditions. Metall Rev 1969;14:1–24. https://doi.org/10.1179/mtlr.1969.14.1.1.
[181] Jeong HT, Kim WJ. Calculation and construction of deformation mechanism maps and processing maps for CoCrFeMnNi and Al0.5CoCrFeMnNi high-entropy alloys. J Alloys Compd 2021;869:159256. https://doi.org/10.1016/j.jallcom.2021.159256.
[182] Dong F, Yuan Y, Li W, Zhang Y, Liaw PK, Yuan X, et al. Hot deformation behavior and processing maps of an equiatomic MoNbHfZrTi refractory high entropy alloy. Intermetallics (Barking) 2020;126:106921. https://doi.org/10.1016/j.intermet.2020.106921.
[183] Yu Z, Xie B, Zhu Z, Xu B, Sun M. High-temperature deformation behavior and processing maps of a novel AlNbTi3VZr1.5 refractory high entropy alloy. J Alloys Compd 2022;912:165220. https://doi.org/10.1016/j.jallcom.2022.165220.
[184] Li T, Lu Y, Li Z, Wang T, Li T. Hot deformation behavior and microstructure evolution of non-equimolar Ti2ZrHfV0.5Ta0.2 refractory high-entropy alloy. Intermetallics (Barking) 2022;146:107586. https://doi.org/10.1016/j.intermet.2022.107586.
[185] Bai ZC, Ding XF, Hu Q, Yang M, Fan ZT, Liu XW. Unique deformation behavior and microstructure evolution in high-temperature processing of a low-density TiAlVNb2 refractory high-entropy alloy. J Alloys Compd 2021;885. https://doi.org/10.1016/j.jallcom.2021.160962.
[186] Jeong H-T, Kim WJ. Deformation mechanisms and processing maps for high entropy alloys (presentation of processing maps in terms of zener–hollomon parameter): review. Materials 2023;16:919. https://doi.org/10.3390/ma16030919.
[187] Tsai K-Y, Tsai M-H, Yeh J-W. Sluggish diffusion in Co–Cr–Fe–Mn–Ni high-entropy alloys. Acta Mater 2013;61:4887–97. https://doi.org/10.1016/j.actamat.2013.04.058.
[188] Yeh JW. Recent progress in high-entropy alloys. Annales de Chimie. Science Des Materiaux 2006;31:633–48. https://doi.org/10.3166/acsm.31.633-648.
[189] Zhang Y, Gao MC, Liaw PK, Yeh JW. High-entropy alloys. Fundamentals and Applications 2016. https://doi.org/10.1007/978-3-319-27013-5_12.
[190] Sen S, Zhang X, Rogal L, Wilde G, Grabowski B, Divinski SV. 'Anti-sluggish' Ti diffusion in HCP high-entropy alloys: chemical complexity vs. lattice distortions. Scripta Mater 2023;224:115117. https://doi.org/10.1016/j.scriptamat.2022.115117.
[191] Kucza W, Dąbrowa J, Cieślak G, Berent K, Kulik T, Danielewski M. Studies of "sluggish diffusion" effect in Co-Cr-Fe-Mn-Ni, Co-Cr-Fe-Ni and Co-Fe-Mn-Ni high entropy alloys; determination of tracer diffusivities by combinatorial approach. J Alloys Compd 2018;731:920–8. https://doi.org/10.1016/j.jallcom.2017.10.108.
[192] Langdon TG. Grain boundary sliding revisited: developments in sliding over four decades. J Mater Sci 2006;41:597–609. https://doi.org/10.1007/s10853-006-6476-0.
[193] Cao Y, Zhang W, Liu B, Liu Y, Du M, Fu A. Phase decomposition behavior and its effects on mechanical properties of TiNbTa0.5ZrAl0.5 refractory high entropy alloy. J Mater Sci Technol 2021;66:10–20. https://doi.org/10.1016/j.jmst.2020.05.038.
[194] Carreño F, Ruano OA. Threshold stresses in high temperature deformation of dispersion strengthened aluminum alloys. Mater Sci Eng, A 1996;214:177–80. https://doi.org/10.1016/0921-5093(96)10406-8.
[195] Park K-T, Lavernia EJ, Mohamed FA. High-temperature deformation of 6061 Al. Acta Metall Mater 1994;42:667–78. https://doi.org/10.1016/0956-7151(94)90264-X.
[196] Tian Q, Zhang G, Yin K, Wang L, Wang W, Cheng W, et al. High temperature deformation mechanism and microstructural evolution of relatively lightweight AlCoCrFeNi high entropy alloy. Intermetallics (Barking) 2020;119:106707. https://doi.org/10.1016/j.intermet.2020.106707.
[197] Tong Y, Qiao JC, Yao Y. The constitutive model and threshold stress for characterizing the deformation mechanism of Al0.3CoCrFeNi high entropy alloy. Mater Sci Eng 2018;730:137–46. https://doi.org/10.1016/j.msea.2018.05.109.
[198] Khodashenas H, Mirzadeh H, Malekan M, Emamy M. Constitutive modeling of flow stress during hot deformation of Sn–Al–Zn–Cu–Mg multi-principal-element alloy. Vacuum 2019;170:108970. https://doi.org/10.1016/j.vacuum.2019.108970.
[199] Cabrera JM, Jonas JJ, Prado JM. Flow behaviour of medium carbon microalloyed steel under hot working conditions. Mater Sci Technol 1996;12:579–85. https://doi.org/10.1179/mst.1996.12.7.579.
[200] Cabrera JM, Al Omar A, Jonas JJ, Prado JM. Modeling the flow behavior of a medium carbon microalloyed steel under hot working conditions. Metall Mater Trans A Phys Metall Mater Sci 1997;28:2233–44. https://doi.org/10.1007/s11661-997-0181-8.
[201] Kanyane LR, Malatji N, Popoola API, Shongwe MB. Evolution of microstructure, mechanical properties, electrochemical behaviour and thermal stability of Ti0.25-Al0.2-Mo0.2-Si0.25W0.1 high entropy alloy fabricated by spark plasma sintering technique. Int J Adv Des Manuf Technol 2019;104:3163–71. https://doi.org/10.1007/s00170-019-04185-0.
[202] Rudolf Kanyane L, Patricia Popoola A, Malatji N. Development of spark plasma sintered TiAlSiMoW multicomponent alloy: microstructural evolution, corrosion and oxidation resistance. Results Phys 2019;12:1754–61. https://doi.org/10.1016/j.rinp.2019.01.098.
[203] Yan Y, McGarrity KA, Delia DJ, Fekety C, Wang K. The oxidation-resistance mechanism of WTaNbTiAl refractory high entropy alloy. Corros Sci 2022;204:110377. https://doi.org/10.1016/j.corsci.2022.110377.

Pablo Martin Saint-Laurence holds a Master of Science degree in Metallurgical Engineering from the Technical University Federico Santa María (Valparaíso, Chile), and is a PhD candidate in Materials Science and Engineering of the Technical University of Catalonia UPC (Barcelona, Spain). Since 2023, he works as a researcher in the Delft University of Technology (Delft, Netherlands). He has been the recipient of a scholarship to follow PhD studies (2020–2024) granted by the Ministry of Sciences and Technology of Chile. He has performed research stays at the Federal University of Santa Catarina (Brazil), University of Concepción (Chile), and the Institute of Glass and Ceramics of Madrid (Spain). His master and doctoral research work were centered in the development of high-entropy alloys employing powder metallurgy techniques, with a focus in the composition-microstructure relationship. Particularly, his doctoral thesis investigated the development of refractory

high-entropy alloys by powder metallurgy and additive manufacturing approaches, studying their high-temperature mechanical behavior. He has authored 7 articles published in peer-reviewed scientific journals in the subjects of powder metallurgy and/or high-entropy alloys, currently presenting a h-index of 5. Besides, he has presented his work in various national and international conferences in various countries, including Chile, Argentina, Mexico, Brazil, Spain and Portugal. His research activity can be publicly followed in its Google Scholar profile: https://scholar.google.com/citations?user=pk2kPoIAAAAJ&hl=en.

Claudio Aguilar Ramirez is a Metallurgical Engineer and holds a PhD in Materials Science and Engineering form the University of Santiago of Chile. Since 2012 he works as an Associated Professor of the Technical University Federico Santa María (UTFSM), teaching different courses such as Materials Science, Metallurgical Thermodynamics, Powder Metallurgy, and Materials for Engineering applications. He has been Director of the Metallurgical and Mining Department in the UTFSM, as well as Director of the Graduate School of the university. Currently, he is the head of the Research in Powder Metallurgy group, focused on giving technological solutions to the mining, metallurgical, and materials industries. Additionally, he has participated in 39 national and international research projects, collaborating with multiple universities and research centres in Chile, as in Mexico, Brazil, and Spain, and he has directed 11 doctoral and master students. Additionally, he had carried out research stays in different universities of Mexico, Spain, and USA. His area of expertise is centered in the development of new advanced metallic and composite materials employing powder metallurgy techniques with a thermodynamics-based approach, studying Cu alloys, Ti-based alloys, high-entropy alloys, among others. He has published 70 articles indexed in the Journal Citation Report and 65 presentations in international conferences, exhibiting a total h-index of 25. His research activity can be publicly followed in its Google Scholar profile: https://scholar.google.es/citations?user=VjmgcGIAAAAJ&hl=es

José María Cabrera Marrero was born on December 8, 1964 in Santa Cruz de Tenerife, Canary Islands, Spain. He holds a PhD in Industrial Engineering from the Polytechnic University of Catalonia (UPC), having received the Extraordinary Doctorate Award (1995) from the Barcelona School of Industrial Engineering for his doctoral thesis. Likewise, his final degree project was awarded the first prize (1992) for the aforementioned projects by the College and Association of Industrial Engineers of Catalonia. He has been the recipient of a research fellowship (1992–1995) and a postdoctoral fellowship (1995–1996) from the Generalitat de Catalunya. He has carried out research stays at McGill University, Montreal (six months spread over two summers), at the National Polytechnic Institute of Mexico City (10 months between 1995 and 1996, and where he obtained a visiting professor appointment), at the Universidade Federal de Sao Carlos (Brazil) for 3 weeks in 2012, at the Institute of Materials Research of the UNAM (Mexico) for two months (January–February 2017). He has done a sabbatical stay at the Institute of Research in Materials and Metallurgy of the Universidad Michoacana de San Nicolás de Hidalgo, Morelia for 12 months (September 2019–August 2020), the latter funded by CONACyT. He is currently a University Full Professor in the Department of Materials Science and Engineering at the UPC. He was secretary of the department for 10 years, and vice director of the department and head of the doctoral program for another 10 years. At the same time, he was responsible for 15 years in the area of forming processes at the Manresa Technology Center (CTM) until March 2016. He is a professor of the subjects of Selection of Materials in Design, Metallurgical Technology, Physical Metallurgy, Metal Manufacturing and Nanostructured Materials at the School of Engineering of Barcelona East. He has participated in more than 70 research projects (leading 50) both of competitive public funding (responsible for four CICYT projects, a PETRI, an ALFA network, member of a CYTED project, leader of two European RCFS projects and participant in two others), and in projects with companies (including two large-scale projects funded by the CENIT program). His area of knowledge is oriented to the characterization of the behavior of metallic materials to plastic deformation, mainly at high temperature. It is basically in this area where Professor Cabrera has made his greatest contributions, especially by offering a universal constitutive equation that explains the hot flow curves of practically all types of metallic materials. This equation, which has a physical basis, can be introduced into process simulation software by means of numerical techniques, while allowing microstructural predictions to be made. It has also recently focused on obtaining ultra-fine and nanometric grain structures in metallic materials by processes of severe plastic deformation (ECAP, Mechanical Milling). He has given lectures, talks and courses at universities, institutes and companies in France, England, Germany, Belgium, Greece, Russia, Mexico, Argentina, Colombia, Chile, Venezuela, India and Brazil. He has been appointed as director of the Fundacion Centre CIM of UPC since September 2021, a technical centre oriented to additive manufacturing. His research activity can be publicly followed in its Google Scholar profile: https://scholar.google.es/citations?hl=es&user=N4HojSgAAAAJ